CHARACTERISTICS AND USES OF DUAL-SPIRAL DUAL-ENERGY CT IN RADIOTHERAPY OF THE HEAD AND NECK

Enric Fernández-Velilla Ceprià

TESI DOCTORAL UPF/2022

Thesis supervisors:

Dr. Manuel Algara López

Dr. Miguel Ángel González Ballester (Department of Information and Communication Technologies. Universitat Pompeu Fabra)

DEPARTAMENT DE MEDICINA I CIÈNCIES DE LA VIDA

Universitat Pompeu Fabra Barcelona

To Miquel and Silvia

Acknowledgments

To my parents, who have been always there, in the best and the worst moments.

To Teresa, Francesc, Lydia and Pilar for their unconditional support.

To Marisa Jiménez, who always believed in me. Always in my heart.

To my thesis supervisors Dr Miguel Angel González, Dr Manuel Algara, and to my tutor Dr Xavier Sanz, for their patience and support. An especial acknowledgement for Dr Algara, who facilitated the economic resources that allowed this research.

To my colleagues Jaume, Òscar, Martí, Núria, Miguel and Laura, the Medical Physics and Radiation protection teams at Hospital del Mar.

To the Radiation Oncologists of the Radiation Oncology at Hospital del Mar, Palmira, Anna, Núria, and Ismael who actively collaborated in the second part of this work. Especial thanks to Dr Ismael Membrive whose intervention was capital to include more patients in this study.

To the RTTs of the Radiation Oncology department, and especially to those who acquired the CT images of the patients Nuria, Susana and Marta.

To Rafa Jiménez, who helped me to create and follow the acquisition protocols.

To my friends Víctor and Esperança, who always gave me their most sincere support.

To my friend Fernando Barral, who always had an answer to my questions about the equipment.

To my friend Dr. Toni Vila, with whom I started my interest on CT imaging.

To Isa, who brought me her support to start this research.

Abstract

Radiotherapy for tumors of the head and neck requires high accuracy to treat tumors at high doses while protecting normal organs. New imaging technologies for delineation hold potential for improved outcomes; among these, dual-energy computed tomography (DECT) is one of the most promising techniques being introduced in hospitals today.

DECT consists of a double CT acquisition, with one scan at low kilovoltage and one at high. Among the different existing types of DECT, this study focuses on dual-spiral, whose main advantages are its low cost and the spectral separation between energies. Disadvantages include a long acquisition time that increases motion artifacts and variations of iodine concentration in the body. There is an abundance of literature about other types of DECT, but evidence on dual-spiral DECT is still limited. The overarching aim of this study is to fill this gap in knowledge with a comprehensive description of dual-spiral characteristics.

The paper is divided into three main parts.

- First, the performance of virtual monoenergetic images (VMIs) is studied in terms of uniformity, high- and low-contrast resolution, noise spectrum, and iodine enhancement. The objective is to determine the quality of VMI and if there is a range of energies that confer a real improvement over single-kilovoltage acquisitions.
- The second part assesses the utility of DECT in tumor delineation. We present a subjective analysis, an evaluation of time for delineation, and a comparison of interobserver variability.
- Finally, the problem of the injected contrast in dose calculations is addressed. We study the use of virtual non-contrast (VNC) images as a means to avoid the acquisition of an additional true non-contrast series for dose calculations.

Our results show that dual-spiral DECT is not inferior to the other types of DECT.

- VMIs are of good quality; the optimal range is 45 keV to 55 keV.
- Interobserver variability is comparable, and doctors feel more comfortable delineating compared to other types of DECT.
- VNC images can substitute the non-contrast acquisition for dose calculations after a waiting time of about 76 s to prevent changes in iodine concentration.

Resumen

La radioterapia de tumores de cabeza y cuello es una disciplina exigente que necesita una alta precisión para tratar tumores a altas dosis protegiendo los tejidos sanos. Entre las nuevas tecnologías de imagen para delineación de órganos, la TC de Doble Energía (DECT) es una de las más prometedoras.

La DECT consiste en una doble adquisición de TC: una a alto y una a bajo kilovoltajes. Entre los diferentes tipos, este trabajo analiza la de Doble Espiral, cuyas ventajas principales son su coste económico y la separación espectral entre energías. Sin embargo, sufre desventajas como un mayor tiempo de adquisición que incrementa los artefactos de movimiento y las variaciones temporales en la concentración de yodo. Hay numerosa literatura sobre los otros tipos de DECT, pero no sobre la de Doble Espiral. Nuestro objetivo es cubrir ese espacio con un completo estudio de la DECT de Doble Espiral.

El trabajo está dividido en tres partes principales:

- En la primera estudiamos las características de las Imágenes Monoenergéticas Virtuales (VMI) en términos de uniformidad, resolución de alto y bajo contraste, espectro del ruido y mejora del yodo. El objetivo es saber si tienen calidad suficiente y si hay un rango de energías de mejor calidad que las adquisiciones de kilovoltaje único.

- La segunda parte analiza la utilidad de la DECT para delineación de tumores. Presentamos un estudio subjetivo de mejora percibida, una evaluación del tiempo de delineación y una comparación de la Variabilidad Interobservador.

- En la tercera parte abordamos el problema del contraste de yodo en los cálculos de dosis. Aquí estudiamos el uso de las Imágenes Virtuales Sin Contraste (VNC) para evitar adquisición adicional de imágenes reales sin contraste para los cálculos de dosis.

Nuestra conclusión es que la Doble Espiral no es inferior a los otros tipos de DECT:

- Las imágenes VMI tienen buena calidad, especialmente entre 45 y 55 keV.

- La Variabilidad Interobservador no es peor, y los médicos perciben las VMI como más cómodas y mejores para delinear.

- Las imágenes VNC pueden sustituir la serie sin contraste, siempre y cuando se aplique un retraso de 76 segundos para evitar cambios en la concentración de yodo.

Table of contents

List of figures

List of Tables

Summary of abbreviations

AAPM	American Association of Physicists in Medicine
CDF	combined dissimilarity factor
CE	contrast enhancement
CNR	contrast-to-noise ratio
CT	computed tomography
CTDI	computed tomography dose index
CTV	clinical target volume
DC	Sorensen-Dice coefficient
DECT	dual-energy computed tomography
DF-DECT	dual-filter dual-energy CT
DFT	discrete Fourier transform
DLD	dual-layer detector
DS-DECT	dual-spiral dual-energy CT
DXRS-DECT	dual X-ray sources dual-energy CT
FkV-DECT	fast kV-switching DECT
GMI	geographical miss index
GTV	gross target volume
HD	Hausdorff distance
HU	Hounsfield units
ICRU	International Commission on Radiation Units
IEC	International Electrotechnical Commission
IMAR	iterative metal artifacts reduction (algorithms)
IOV	interobserver variability
IV	intravenous (contrast)

JI	Jaccard index
keV	kiloelectron volts
kVp	peak kilovoltage
LCR	low-contrast resolution
LSF	line spread function
MIX	name of the alpha-blended images used in this study
MRI	magnetic resonance imaging
MTF	modulation transfer function
NPS	noise power spectrum
OAR	organs at risk
PCD	photon-counting detector
PET	positron emission tomography
PRV	planning organ at risk volume
PSF	point spread function
PTV	planning target volume
ROI	region of interest
RT	radiotherapy
SD	standard deviation
SECT	single-energy computed tomography
VMAT	volumetric modulated arc therapy
VMI	virtual monoenergetic image
VNC	virtual non-contrast image

1. INTRODUCTION

1. Introduction

1.1 Background

Many hospitals are introducing dual-spiral, dual-energy computed tomography (DECT) because of its simplicity and low cost, especially when a computed tomography (CT) scanner is completely dedicated to radiotherapy and the number of patients is not high. Head and neck tumors, which account for about 4% of all malignant tumors, are particularly amenable to DECT imaging, so it is crucial to know if dual-spiral DECT meets the standards for quality and accuracy that radiotherapy requires.

Current trends in clinical practice justify the introduction of DECT, which can help to reduce the quantity of iodine injected into the patient in CT protocols because it has a higher contrast-to-noise ratio (CNR). This reduction is expected to limit adverse effects, especially in patients with compromised kidney function.

Moreover, DECT enables the construction of virtual non-contrast (VNC) images. Many hospitals use iodine-enhanced images for plan calculations, assuming a small increase in calculation uncertainty, typically under 1%. Other centers prefer calculations only in non-contrast images and acquire one series with iodine for tumor delineation plus one without for calculations. However, real non-contrast images can be substituted with VNC images from DECT studies, averting the need for the non-contrast series and thus reducing the imaging radiation doses to the patient. Spanish law makes this dose reduction mandatory when it can be achieved. However, this possibility has not been studied in dual-spiral DECT.

Radiotherapy of the head and neck requires high precision to delineate the tumor and protect organs. CT imaging is used for both delineation and radiotherapy (RT) planning calculations. However, the similar densities of soft tissues pose challenges for radiation oncologists. Although delineation is usually done through a multimodal approach, making use of magnetic resonance imaging (MRI) or positron emission tomography (PET), DECT has demonstrated its capacity to correct some of the uncertainties intrinsic to those imaging systems.

Among the different types of DECT, dual spiral stands out for its simplicity and low cost. There is an abundance of literature about applications of DECT in RT but just a few papers about dual-spiral DECT. The overarching aim of this study is to fill this gap in knowledge with a comprehensive description of dual-spiral characteristics.

Another aspect that must be investigated, constituting one of the main objectives of this study, is the possibility of virtually removing iodine from images to improve the precision of calculations in RT planning.

The Radiation Oncology Department at Hospital del Mar started to work with DECT in 2018. The lack of studies about its quality and features made it necessary to acquire our own data and perform our own thorough research. Since 2018, physicists and radiation oncologists from different hospitals across Europe have been asking us for information about the characteristics and uses of dual-spiral DECT, alerting us to the pertinence and opportunities for this line of research. In consequence, dual-spiral DECT was chosen as the focus of this dissertation, which can now be disseminated to the wider scientific community.

1.2 Theoretical framework

1.2.1 CT imaging in radiotherapy

Wilhelm Conrad Roentgen discovered X-rays in 1895. Their application in medicine started shortly thereafter, and by 1896 they were being adopted as treatments for different pathologies. The use of these techniques represented the dawn of radiotherapy, the medical specialty whose intent is to treat disease, malignant or not, by means of ionizing radiation.

Nowadays, radiotherapy is a high-precision discipline that makes the most of new imaging technologies to localize both the regions to treat and the organs to protect. Radiation technologies have evolved in parallel with imaging techniques to improve precision and allow higher radiation doses with decreased side effects. Today it is not possible to separate radiotherapy at high doses from imaging systems.

Among the different applications of radiotherapy, its use in oncology is crucial. The radiobiological effects of radiation destroy a high proportion of diseased cells and increase tumor control, but such high doses are dangerous for normal tissue, which must be protected, with doses kept under known tolerance limits. High-precision imaging and treatment are thus mandatory.

RT treatment entails different pre-treatment phases, starting with the acquisition of images for organ localization and delineation. These images must have certain characteristics to make them useful for the RT planning procedures: they have to be acquired in the exact same position that the patient will adopt in the treatment unit, and they must allow dose calculations at the range of energies used for irradiation. Among the imaging techniques currently available, CT fulfils those requirements and is used for both delineation and planning. As CT images present some limitations, like a low soft-tissue contrast and a lack of metabolic information, CT series are commonly combined with other MRI or PET images to guide the delineation process.

CT images have some advantages that make them suitable for radiotherapy.

- Geometrical distortions are small.
- The current CT systems are wide enough to allow identical patient positioning as that which will be used in the treatment unit.
- They achieve a good contrast between bony structures and soft tissue.
- As CT scans are X-ray absorption images, they can be used for dose calculations in photon treatments.

Since CT images are obtained by means of X-rays, the same radiation used for treatment, RT plans can be accurately predicted and calculated. However, they show low contrast between different soft tissues. This problem can be addressed with the use of iodinated contrast, but this approach introduces some issues about dose calculations that must be considered in radiotherapy calculations.

CT images are attenuation images. When X-rays are emitted from the X-ray tube into the patient's body, some of them are absorbed, while the rest exit on the opposite side, reaching the CT detector. From the detector readings, the CT scanner can calculate the attenuation of each voxel in the body as a value relative to the attenuation of water. These

relative values are named CT numbers, and they are expressed in especial units called Hounsfield units (HU):

$$\mathrm{HU} = C \cdot \frac{\mu_{\mathrm{Tissue}} - \mu_{\mathrm{Water}}}{\mu_{\mathrm{water}}} \cdot 1000 \qquad \text{(Eq.1)}$$

where μ_{Tissue} and μ_{water} are the linear attenuation coefficients of the voxel and water, respectively, and C is a correction value depending on the acquisition itself. With this definition, CT numbers have a value of −1000 HU for air and 0 HU for water. Those are the only fixed values on the CT scale.

In contrast, the CT number of a particular point on the patient is not a fixed value. Rather, it depends on the voxel composition, the X-ray spectrum, the CT scanner, and the reconstruction algorithm.

Changes in the X-ray spectrum cause the most important variation in CT numbers for a given pixel. This spectrum depends on the anode material of the X-ray tube, tube construction, filtration, power generator, and kilovoltage.

The tube kilovoltage is abbreviated as kVp. The use of this abbreviation is rooted in the fact that the shape of the X-ray spectrum of a given beam is not unique for a particular kilovoltage value. Nevertheless, the maximum energy of the photons composing that beam is fixed and unique for the maximum value of the kilovoltage, which is called *peak kilovoltage*, or *kVp* (**Fig. 1**).

Since CT numbers vary with the tube kilovoltage, all planning images are typically acquired at the same standard value of 120 kVp in RT calculations. This convention allows medical physicists to keep a unique calibration curve for each CT scanner in the treatment planning system.

However, a single kilovoltage of 120 kVp also has two notable disadvantages. First, the contrast between soft tissues is small. If the CT number scale comprises values between −1000 HU and 3096 HU (maximum and minimum for an 11-bit CT), soft tissues fall inside a narrow range of approximately −100 HU to 100 HU. Secondly, a single kilovoltage setting does not adapt the acquisition to varying patient thicknesses. As radiation transmission increases with energy, thicker locations would benefit from higher kilovoltages, i.e., 140 kVp, and thinner from lower, i.e., 80 kVp to 100 kVp.

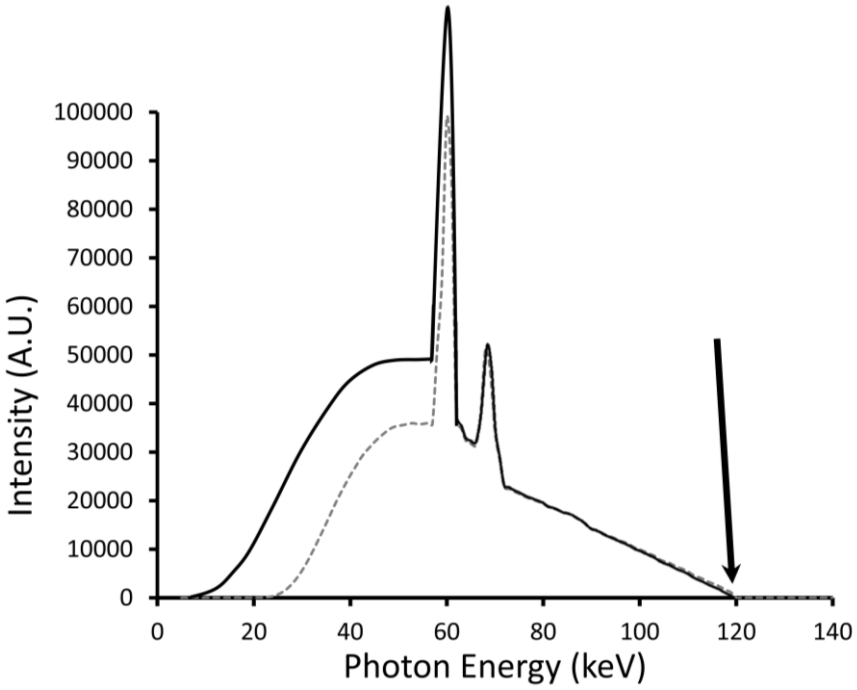

Figure 1. Spectrum of the Siemens Somatom Confidence CT for 120 kVp. The dotted line corresponds to the Sn filtered spectrum, and the solid line to the unfiltered. The arrow points out the maximum photon energy, which is the same for both curves. Data courtesy of Siemens EMEA.

One particularly complex treatment is the irradiation of tumors of the head and neck. This region is problematic because of the high radiation doses required for tumor control and the presence of many organs at risk (OARs) that must be protected. Thus, head and neck tumors require highly accurate imaging for delineation and planning. However, OARs, tumors and lymph nodes are all soft tissues, and their images at 120 kVp show insufficient contrast. This problem can be addressed by using MRI or PET scans and registering them to the CT series (**Figure 2**).

In clinical practice, radiation oncologists usually use those supplementary images for delineation. Although soft-tissue contrast is higher in MRI, and PET gives functional information, several uncertainties intrinsic to MRI and PET images must be considered when matching to CT series.

- MRIs have geometrical distortions that arise when matching to CT images.
- PET images usually have less resolution and require long time acquisitions.
- Patient position, immobilization devices, and couch shape are usually different.

- MRI and PET have long acquisition times that increase uncertainties due to patient motion.
- About 10% of patients cannot undergo MRI scans for different reasons, such as claustrophobia or metal implants.

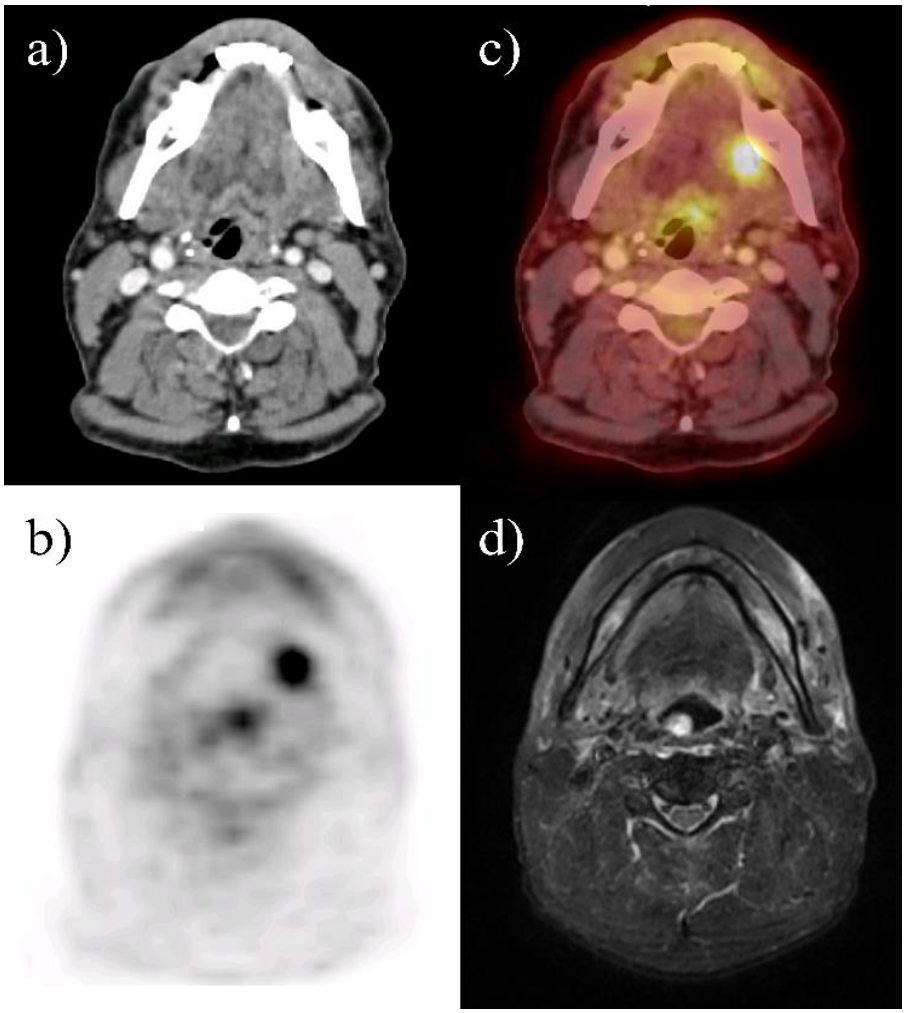

Figure 2. Different modalities in a head and neck patient. a) CT with contrast. b) PET. c) Registration of PET and CT, and d) MRI. As seen here, PET has the lowest resolution. MRI images are not suitable for RT calculations.

These aspects can make image matching impossible, and any procedure that introduces important uncertainties may impair delineation accuracy. In light of these considerations, it is critical to find a way to increase contrast directly in the CT acquisition of the head and neck area.

The most common way to address the lack of contrast at 120 kVp is by injecting an intravenous (IV) iodinated contrast into the patient before the acquisition. Due to its high atomic number (Z = 53), iodine increases the photoelectric effect, enhancing the CT numbers of tissues.

At 120 kVp, the predominant interaction mechanism between X-rays and tissues is Compton scatter[1] (**Figure 3**). This effect is more sensitive to the electronic density of the materials in the path of X-rays than to their atomic number.

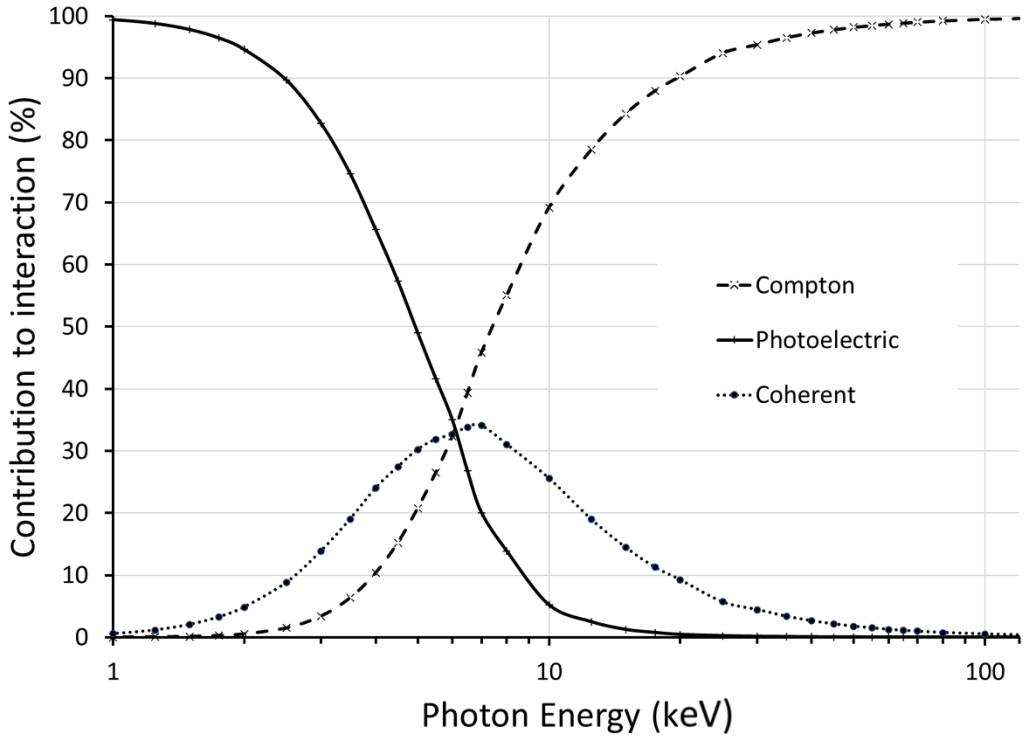

Figure 3. Relative weight of interaction effects for soft tissues in the 1 keV to 120 keV range. The filtered spectrum at 120 kVp has a mean energy of about 80 keV, where Compton scatter is clearly the main interaction. Author's figure based on data from Plechaty et al.[2]

Since the electronic densities of tissues relative to water fall in a narrow interval between 0.9 for fat and 1.8 for cortical bone, the image contrast at 120 kVp is low. When iodine contrast is injected, this element spreads across the patient tissues in different concentrations. Where concentration is higher, the lower energy photons of the 120 kVp spectrum experience an increase in their linear attenuation coefficient due to the predominance of the photoelectric effect at low energies. This causes an iodine-produced enhancement of the contrast between tissues. However, that enhancement is not high

when the whole 120 kVp spectrum is considered because of the predominance of Compton scatter. Contrast can be increased if the lowest kilovoltage achievable is used for the CT acquisition (Figures. 4 and 5), because at low kilovoltages the balance between Compton and photoelectric effects changes in favor of the latter.

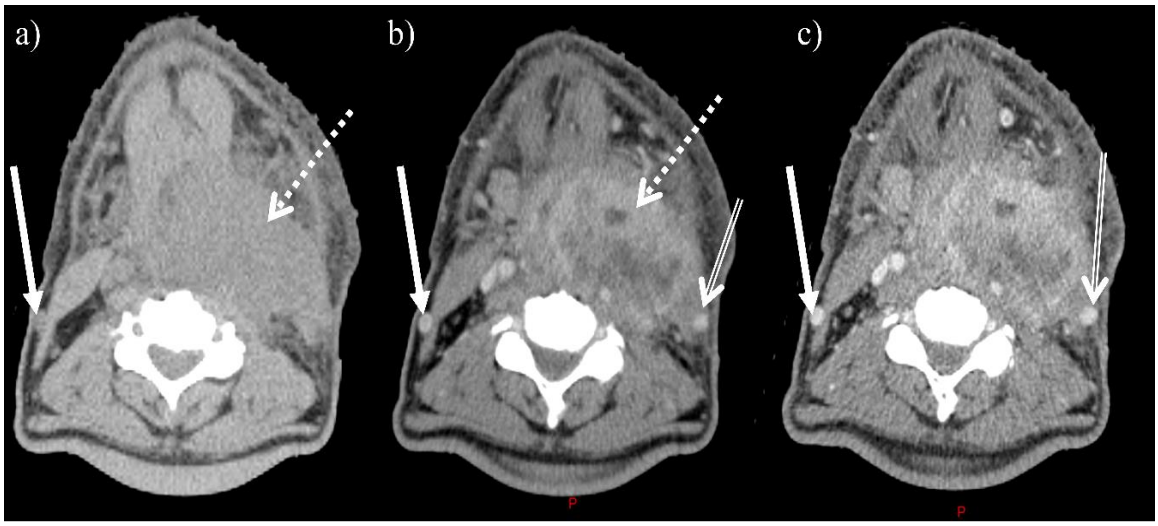

Figure 4. Images of the head and neck with and without iodinated contrast. a) 120 kVp without iodinated contrast. b) 120 kVp with contrast. c) 80 kVp with contrast. The solid arrow points to a vessel that is not well defined in a). The dotted arrow points to the tumor, whose internal structure is invisible in a). The double arrow points to a vessel whose boundaries are clearly visible only at 80 kVp.

It is common practice in RT planning for head and neck tumors to acquire both a CT series with the injection of iodinated contrast for delineation of target volumes and OAR, and a series without iodine for planning and calculations of radiation doses. Thus, hospitals that apply this technique are assuming that iodine may reduce the accuracy of calculations. The main advantage is that the iodine-injected images can be acquired at a low kilovoltage that is only used for delineation, not for low-kilovoltage dose calculations, taking advantage of the increased iodine enhancement.

Even though injected iodine does have a certain impact on dose calculations, some actions can reduce the uncertainties. Many centers acquire only one series with iodinated contrast for both delineation and calculations, an approach supported by several studies[3,4,5,6]. The main advantage is the lower radiation dose related to imaging, but on the other hand, iodine enhancement is also lower.

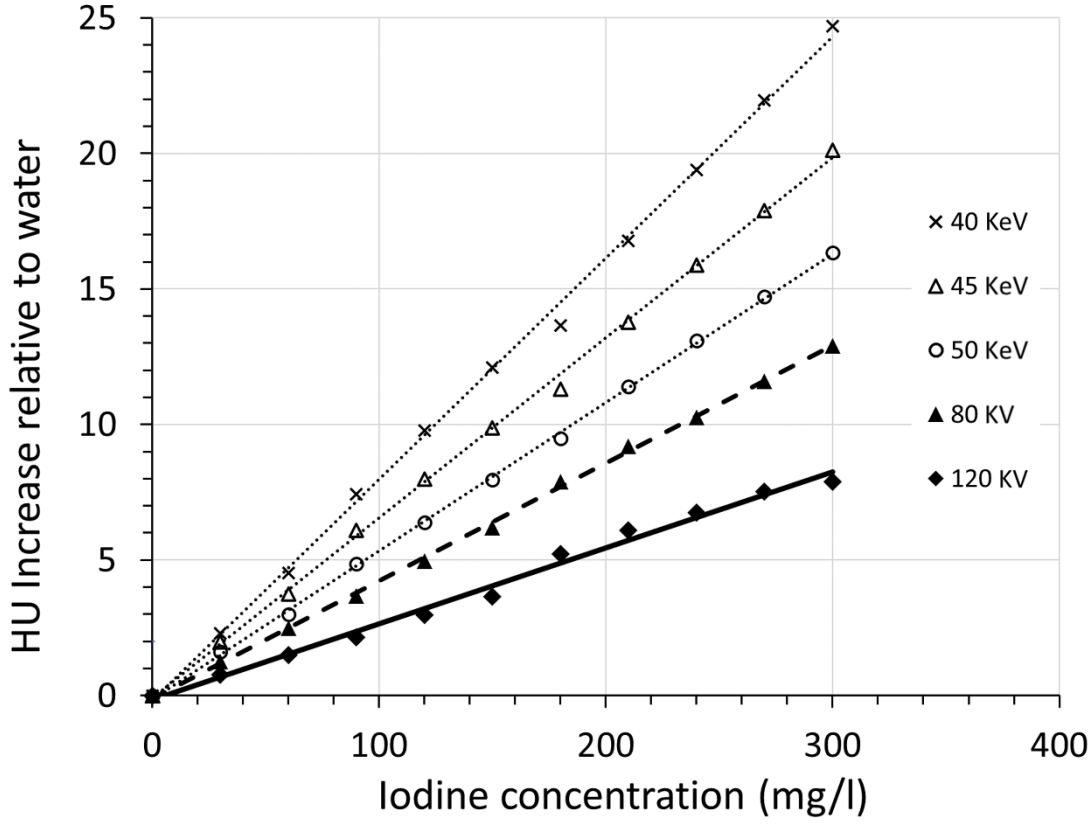

Figure 5. Effect of kVp and concentration of iodine for a water-iodine solution.

1.2.2 Dual-energy CT

DECT is an alternative solution to deal with the iodine question, first proposed by Hounsfield in 1976. It combines two CT acquisitions, one at low kilovoltage (typically 80 kVp) and one at high (typically 140 kVp). DECT takes advantage of the different behavior of materials when X-rays of different energies pass through them:

The low kilovoltage series provides extra iodine enhancement, while the high kilovoltage series has less noise and is more like the 120 kVp series. This allows some degree of material characterization and decomposition that is not possible with SECT.

At low energies, the predominant interaction effect is the photoelectric effect. This type of interaction is especially sensitive to the atomic number Z of the interacting material and to its electronic density ρ_e. The probability of photoelectric interaction for a photon of energy E can be written as:

$$P(\text{PhotoE}) \propto \frac{\rho_e \cdot Z^4}{E^3}$$

And for the Compton scatter:

$$P(\text{Compton scatter}) \propto \frac{\rho_e}{E}$$

From the previous expressions, materials with a high *Z* number present a more intense photoelectric effect that causes strong attenuation at low energies. However, as most biological tissues are composed of low *Z* elements, their differences in terms of photoelectric or Compton effects are limited, and the contrast of soft tissues is still low regardless of energy. Bone is the most important exception to that behavior because of the calcium (Z=20) photoelectric contribution.

Although the probability of both interactions decreases as energy increases, the smaller exponent of *E* in the Compton scatter increases the relative proportion of it at high energies in relation to the photoelectric effect. In this case, differences in absorption are more related to density, which is very similar in all patient's tissues. Thus, differences between materials are small even if they have a high *Z* number.

As a result, combining images at high and low kilovoltage should provide information about both the *Z* composition of tissues and electronic density (**Figure 6**).

To take advantage of those characteristics, DECT acquires two different series of images.

- One low-kilovoltage series, typically 80 kVp to 100 kVp, at an energy level where photoelectric interaction of both iodine and radiation absorption is high. These series are usually characterized by higher noise, more artifacts, and a high contrast.
- One high kilovoltage series, typically 140 kVp to 150 kVp, where the Compton effect is completely dominant, and iodine causes less disturbance. When high voltage is set, images have lower noise and less artifacts, but also a lower contrast.

The success in DECT analysis depends on the spectral separation between the high and low kilovoltage. The wider the separation, the better the decomposition (**Figure 7**).

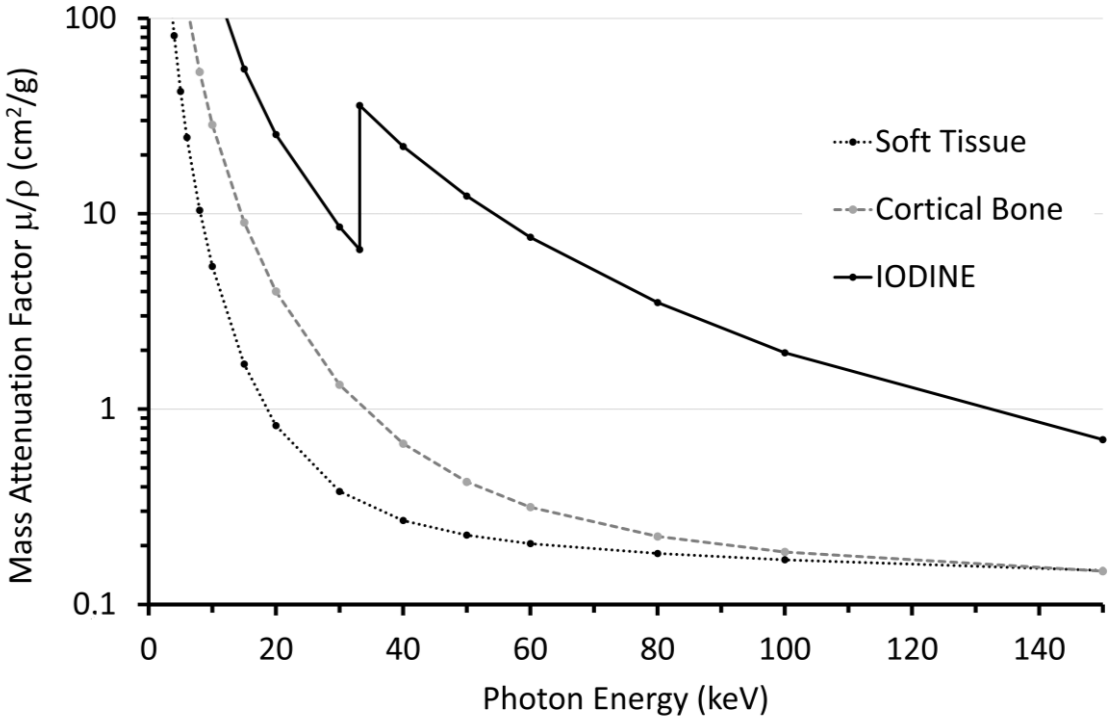

Figure 6. Mass attenuation factors as a function of photon energy. Iodine has a high *Z* number (53) and a K-edge at 35 keV (vertical line). Cortical bone has a high concentration of calcium (*Z* = 27) and a high absorption at low energies due to the photoelectric effect. Above 100 keV, differences between soft tissues and calcium are small and cannot be observed in the figure. Author's figure based on data from https://physics.nist.gov/PhysRefData/XrayMassCoef/tab4.html.

Finally, even though DECT scans are composed of two acquisitions at high and low kilovoltages, it is commonly accepted that the total radiation dose must be kept under the value of the equivalent study at the standard kilovoltage of 120 kVp. This is an important limitation because of differences in the tube efficiency and radiation characteristics at different kilovoltage settings: tube efficiency and radiation penetration decrease with kilovoltage, so as detectors in the CT device receive less radiation, there is a higher level of noise in the images.

When a DECT system allows separate setup of both kilovoltages, the low kilovoltage acquisition is set up with a smaller helicoidal pitch and a higher tube load than that of the high kilovoltage to decrease noise. Even though high kilovoltage images are then set up in the opposite way, they do not show a noticeable degradation in terms of noise. Thus, with the different setup, the overall quality of the DECT study improves without increasing the dose to the patient.

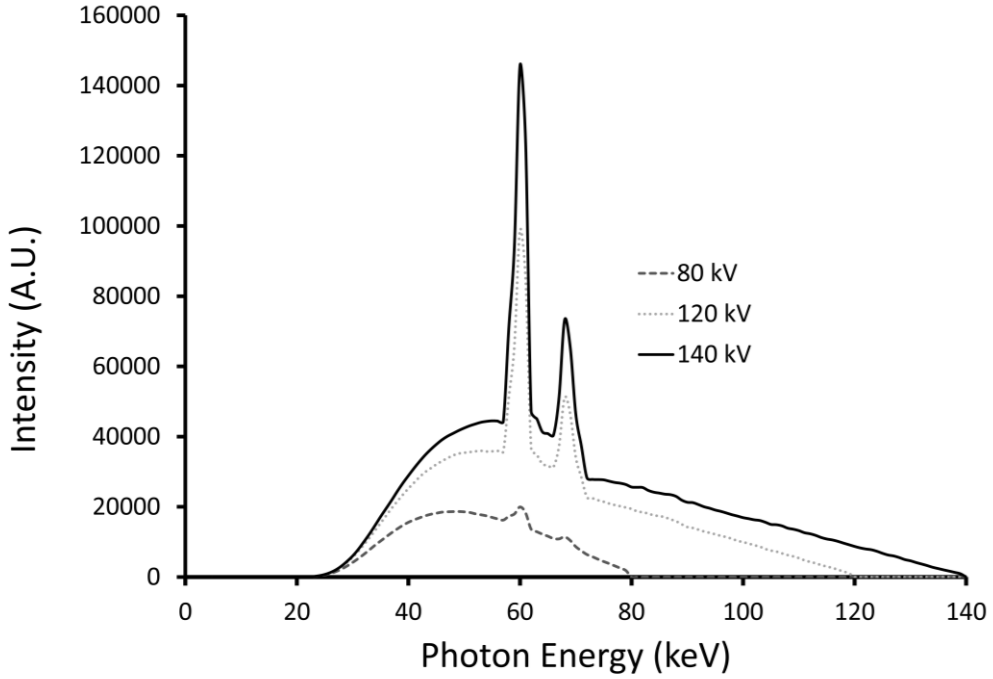

Figure 7. Photon spectra for high and low kVp. Somatom Confidence RT Pro. Siemens Healthineers. Data courtesy of Siemens Healthineers.

DECT studies are commonly used in radiotherapy to enhance iodine contrast and help in tumor and organ delineation. Among the different series that can be obtained, virtual monoenergetic images (VMIs) are specifically designed to that end. Additionally, due to the material decomposition features of DECT, it is possible to virtually remove iodine from tissues, allowing dose calculations on VNC images and eliminating the need for real non-contrast acquisitions.

Different approaches to DECT are available, depending on CT manufacturers and technological solutions.

1.2.3 Types of dual-energy systems

a) Dual-spiral DECT

Dual-spiral DECT (DS-DECT) is the simplest dual-energy system because it does not require critical modifications to the SECT devices. Series are acquired asynchronously,

so the second acquisition starts immediately after the first has finished as if it were a different scan (**Figure 8**).

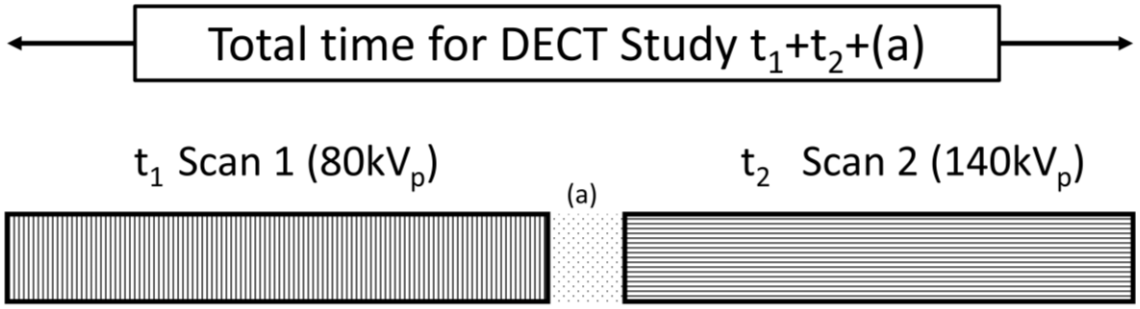

Figure 8. Dual-spiral DECT. There may be a time delay (a) between series due to the fact that in most systems the second series must start in the same location on the body, and the second scan is acquired in the same direction. That means that the patient position must return to the starting position. Some systems (i.e. Siemens Somatom go SIM and Open Pro) can do the second scan in the opposite direction, saving time (a).

DS-DECT stands out for its low cost and simplicity as well as its spectral separation, which is an important factor for material decomposition. On the other hand, the longer acquisition time and the sequential (rather than simultaneous) acquisition can cause motion artifacts and a variation in iodine concentration that can introduce important uncertainties.

Although the first DS-DECT systems did both acquisitions starting from the same point in the patient and scanned in the same direction, recent modifications have eliminated the time to return to the initial couch position, so the second scan starts in the final position of the first and does the acquisition in the opposite direction.

This study focuses on the DS-DECT system, particularly its applications in radiotherapy of the head and neck, where the mandatory patient immobilization can reduce motion artifacts.

b) Fast kV-switching DECT

To improve simultaneity of scans, some DECT systems switch kilovoltage between low and high during tube rotation (**Figure 9**). This is known as fast kV-switching DECT

(FkV-DECT). This approach decreases the number of projections at each tube rotation for each energy if the switching is not quick enough. The faster the switching, the higher the number of projections, but transient effects when changing kilovoltage become an important limitation to decreasing switching time. These effects can increase noise at low kilovoltage and dose at high kilovoltage. To prevent these effects, some manufacturers do asymmetric acquisitions by prolonging the time at low kilovoltage and using a shorter time for high kilovoltage (i.e., General Electric HD750).

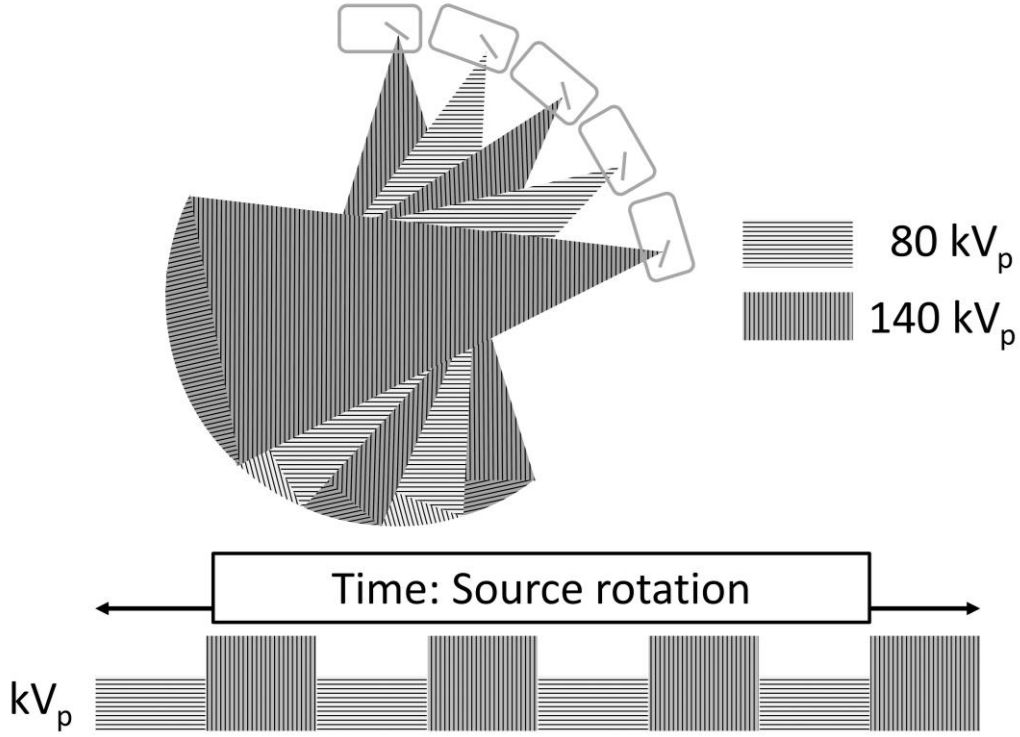

Figure 9. Fast kV switching DECT. Even though the ideal switching should be that represented in the figure, transient effects smooth the slope and cause a lower spectral separation.

The main advantage of FkV-DECT is that the series are acquired almost synchronously, with a separation of about 1 ms, so registration is better and there are no time differences in iodine concentration. Unfortunately, spectral separation may suffer, as filtration cannot be changed between kilovoltages, and the fast switching causes transient effects.

There is a variant for fast-kV switching, where the tube does a complete rotation before switching kilovoltage. This solution has been introduced by Toshiba and is called slow-kV switching. Acquisitions are not simultaneous, and time separation is about one rotation time, but transient variations are no longer a problem, and couch movement is

not needed due to the wide detector used. This type of DECT is halfway between dual-spiral and fast kV-switching DECT.

c) Dual X-ray sources DECT

Dual X-ray sources dual-energy CT (DXRS-DECT) systems have two X-ray tubes mounted with an angular separation of 90º in the same slip-ring structure of the CT device **(Figure 10**). Each tube has its own set of detectors in the opposite part of the ring. This kind of construction allows a totally simultaneous acquisition of the two series because both structures work at the same time. As the tubes are different, these systems have the best spectral separation between high and low kilovoltage. Additionally, tubes can be set up individually, enabling the best performance for both kilovoltages, separate filtration, and individual noise reduction.

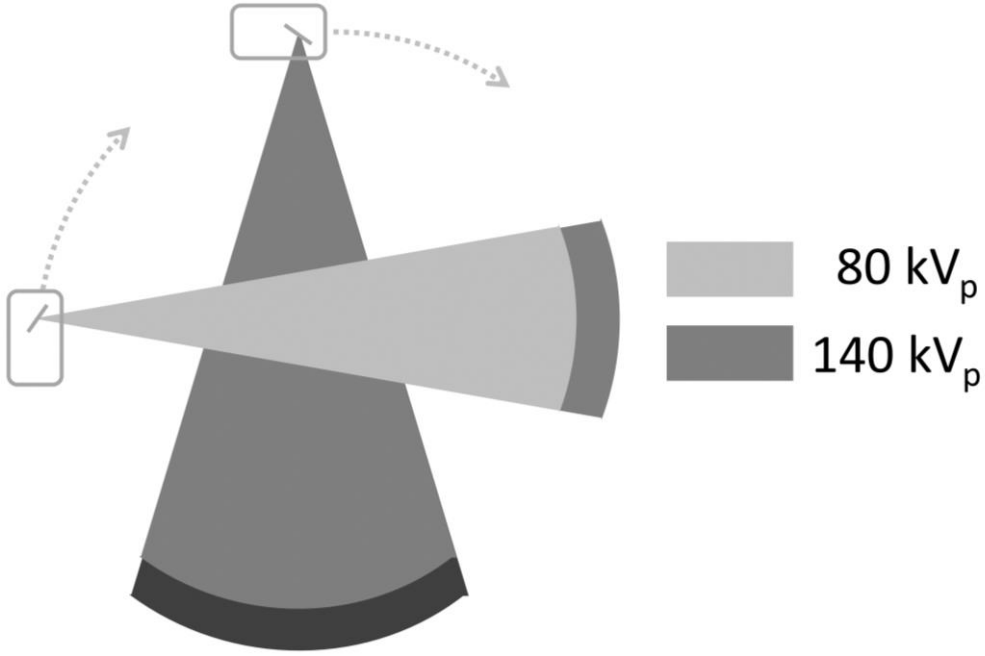

Figure 10. Dual X-ray sources (DXRS) DECT system. In the DXRS system, tubes are mounted at a phase of 90°. The detector array of 80 kVp is smaller than that of 140 kVp. Tubes can be set up separately, but cross scatter can reduce spectral separation.

However, the construction of DXRS-DECT systems entails several limitations. First, there is a phase separation of 90º between series, which can be important in fast moving structures like the heart. Secondly, simultaneous irradiation causes a cross-detection of

scattered radiation because the detector of one tube detects part of the scattering caused by the other. This effect reduces spectral separation unless a scattering reduction algorithm is implemented. The third limitation resides in the limited space inside the CT gantry: the low-kilovoltage source has a smaller detector, and therefore the maximum field of view for DECT is smaller than the maximum achievable by the CT scanner. Typical values for the DECT field of view are 26 cm, 33 cm, or 35 cm, while typical value for SECT is at least 50 cm.

d) Dual-filter DECT (Twin Beam)

Dual-filter dual-energy CT (DF-DECT) is a different approach, with a single tube CT scanner introduced by Siemens Healthineers that presents only a small lack of simultaneity between series. In this case, the tube has two different filters that split the X-rays in half in the craniocaudal direction (**Figure 11**). Each filter is composed of a different material: half is made of gold (Au) and is responsible for the low-energy spectrum, and half is made of tin (Sn) and generates the high-energy spectrum. Notably, this type of DECT uses only a 120 kVp beam, and the high and low separation is obtained by filtration. This means that the spectral separation is lower than in the dual-source, fast kilovoltage-switching and dual-spiral systems.

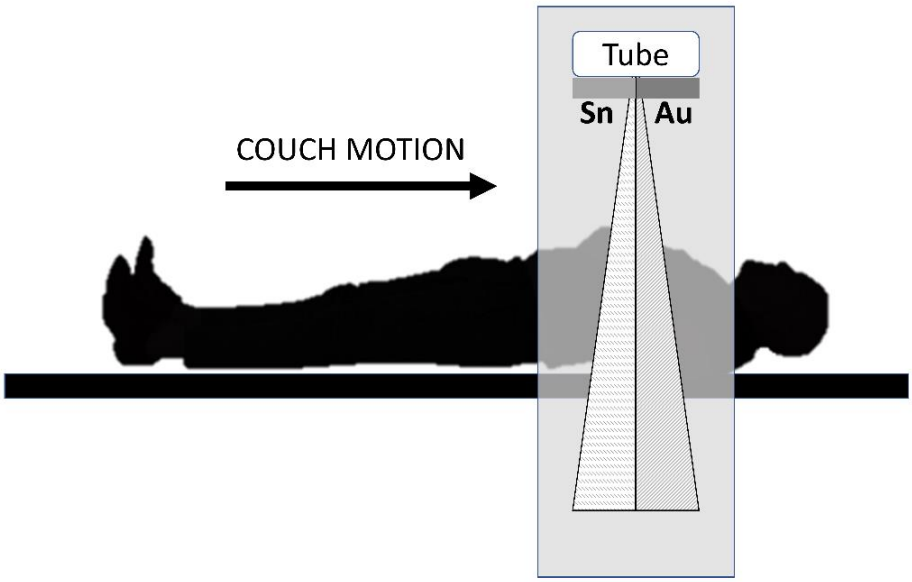

Figure 11. Twin-beam system. The tube is set at 120 kVp, and the spectrum discrimination is done by means of a dual filter.

Nevertheless, DF-DECT has a good temporal registration, even though high- and low-kilovoltage images are not taken simultaneously. Due to its construction, half the detector array acquires the first series, and the other half acquires the second. A slice that has been acquired at one energy must wait until the other half of the detector reaches the same Z-coordinate. The time to reach that position depends on the exploration pitch and is at least one rotation time.

Unfortunately, scattered photons from one filter can reach the detectors of the other half. This is an additional source of a lower energy discrimination in DF-DECT systems.

e) Dual-layer detector DECT

Dual-layer detector dual-energy DECT (DLD-DECT) moves to a different point of view: instead of acting on the X-ray beam, the DECT is obtained by means of a special detector with two layers, one sensitive to low-energy photons and the second sensitive to the higher energies.

In this case, X-rays exiting the patient cross the low-energy layer until they reach the high-energy detector (**Figure 12**). Because of its construction, the main advantage of these systems is that spatial and temporal coincidences of high and low energy series are exact. This feature allows application of material decomposition algorithms in the projection space with no registration errors between series.

The limitations of DLD-DECT include the fact that X-rays experiment additional filtration and attenuation when crossing the low-energy scintillator, thus changing quantity and spectrum of the beam that reaches the high-energy scintillator. Moreover, high-energy photons also interact with the low-energy detector, and part of the low energy is detected by the high-energy detector. Both reasons entail a decrease in energy separation for this type of DECT.

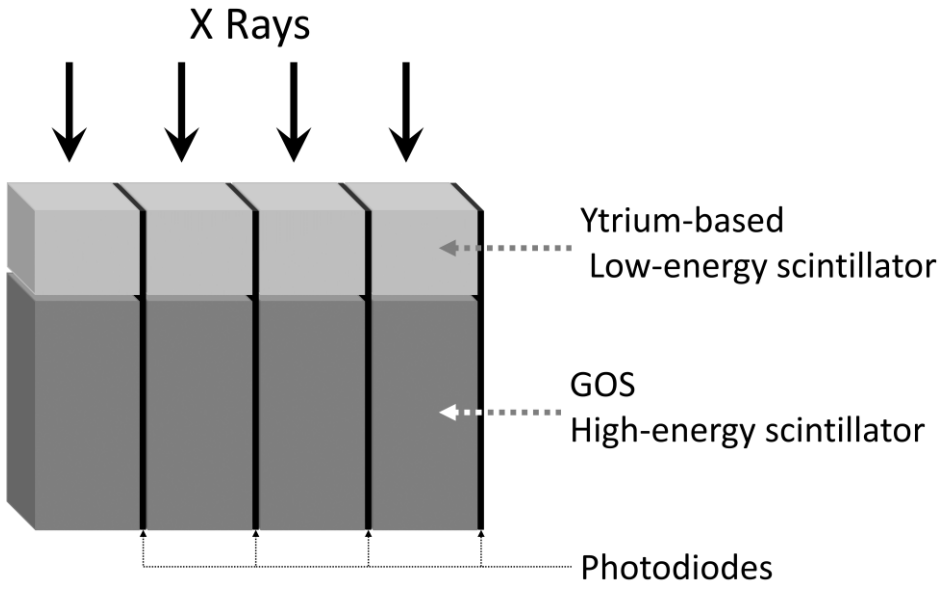

Figure 12. Detail of the dual-layer detector (Nanopanel prism from Philips Iqon Spectral CT). GOS = Gadolinium Oxysulphide Scintillator.

f) Photon-counting detector DECT

The photon-counting detector DECT (PCD-DECT) is the newest solution to acquire spectral information from X-rays. PCDs eliminate the need for a scintillator, as they directly convert radiation interaction to an electronic signal. In these devices (currently only Siemens Naeotom Alpha), each individual photon over 25 keV is counted, as are the electron-hole pairs generated in a CdTe semiconductor layer (**Figure 13**). As the number of pairs released by an individual photon is proportional to its energy, it is possible to know the exact energy of each photon. Thus, a complete spectrum of the X-rays reaching the detector after crossing the patient can be obtained. For design and energy discrimination reasons, the spectrum is divided in energy bins.

Energy discrimination and measurements can be affected by two phenomena that limit their accuracy: first, the photon-generated charge can suffer some degree of distribution between the closest detectors, an effect known as *charge sharing*. Second, some photons are re-emitted when X-rays interact with the semiconductor layer. This effect is known as *K-escape*.

The individual detector size in PCD is smaller than those of scintillator-based systems and does not have inter-detector dead space, two characteristics that increase the potential spatial resolution. However, the final resolution is limited by the anti-scatter grid that is present in all CT systems.

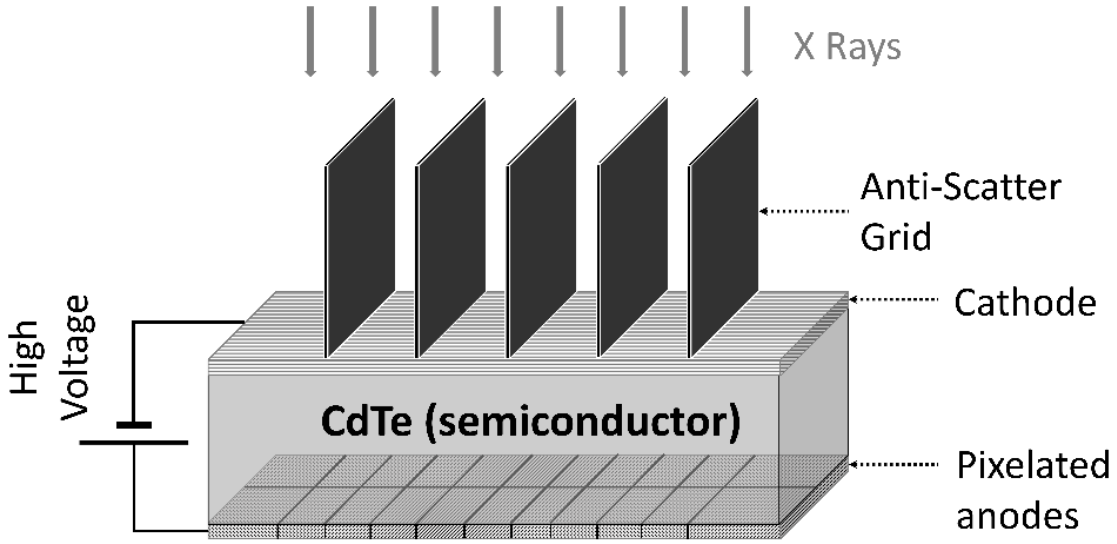

Figure 13. Spectral detector, Siemens Naeotom Alpha.

This type of DECT has several advantages.

- A radiation to light conversion is no longer needed in a scintillator, thus eliminating cross-contamination between photodiodes.
- High- and low-energy series are substituted by the energy bins of the whole spectrum, allowing the creation of any monoenergetic series at any energy in addition to the SECT acquisition.
- There is only one acquisition, any series can be derived from it, and the need for registration disappears.
- Material decomposition of each pixel is based on the whole spectrum, so the system can do a multi-material decomposition instead of the two-material decomposition allowed by other systems.

Finally, a short summary of the different approaches to dual energy can be seen in **Table 1**.

Table 1. Summary of characteristics for all types of dual-energy CT

Dual spiral	**Fast kV-switching**	**Slow kV-switching**	**Dual source**	**Dual filter**	**Dual-layer detector**	**Photon-count detector**	
Beam	Beam	Beam	Beam	Beam	Detector	Detector	**Basis of spectral separation**
Low: sequential acquisitions	Almost exact, only time for switching	High: 1 rotation offset	Very good: 90° between series	High: half collimation offset	Exact	Exact	**Temporal coherence**
High	High	High	High	Moderate	Moderate	High, allows complete spectrum	**Spectral separation**
Only image space	Image and projection spaces	Only image space	Image and projection spaces	Image space	Image and projection spaces	Image and projection spaces	**Spectral analysis**
Full	Full	Full	Limited by detector size of low kV	Full	Full	Full	**Field of view**
Under discussion	Yes	Yes	Yes	Yes	Yes	Yes	**Studies with iodinated**
No	Yes	No	Yes	No	Yes	Yes	**Cardiac DECT imaging**

1.2.4 Radiation dose with DECT

When performing DECT scans, it is important to keep the radiation dose to an acceptable level. The reference level for the DECT dose is usually fixed at that of a similar SECT scan in terms of scan length, slice thickness, patient size, and explored region. The characteristics of DECT scans for fulfilling that requirement strongly depend on the DECT system used.

- **Dual-spiral DECT and slow kV-switching systems** can keep the computed tomography dose index (CTDI) and dose-length product similar to that of a single 120 kVp acquisition by using different performance parameters for each scan. In general, low-kilovoltage scans have more noise but a lower dose, while the reverse is true for high-kilovoltage scans. The way to decrease noise and dose at the same time is by increasing the radiation quantity by increasing the mAs (milliAmpères·second) of the acquisition and decreasing scan pitch in the low-kilovoltage acquisition, and doing the opposite in the high kilovoltage scan.

  Another advantage of dual-spiral DECT resides in the conventional scans: modern CT devices modulate the current of the X-ray tube filament to reduce dose by adapting it to patient thickness in each slice. Dual-spiral DECT allows this kind of modulation even though it is the same in both scans.

- **Fast kV-switching DECT** can be dose-modulated in order to reduce patient dose. However, it is not possible to program different scan characteristics for each energy. Couch speed and acquisition pitch must be the same for both scans, and transient effects of fast kilovoltage switching make it difficult to change mA at the same time, so it is kept at an average value between both kilovoltages.
- **Dual-source DECT** has the advantage that both X-ray tubes can be set up separately. Thus, the mA can be increased in the low-kilovoltage tube and decreased in the high-kilovoltage tube. Scan pitch must be the same for both scans because they are acquired at the same time. Thus, in comparison with dual-spiral DECT, dual-source DECT requires a greater increase of mA in the low kilovoltage scan to reduce noise. Depending on the tube characteristics, this can be a limiting condition of the low-kilovoltage image quality.

- **Dual-filter DECT** has the advantage of a single-kilovoltage setup of the X-ray tube. As only half the detectors are exposed to each beam, the exploration pitch must be decreased. In this case, pitch is the same for both scans, and no separate setup is possible. Decreasing pitch must be followed by a decrease of tube current to keep the dose at the same value, which can cause higher noise in the low-energy acquisition.
- **Detector-based DECT** systems use only one kilovoltage setup of the X-ray tube. Like dual-filter DECT, exploration pitch and tube current are the same for all energies. Thus, an averaged tube setup is necessary. As a result, and due to the X-ray spectrum, low-energy images usually show higher noise.

1.2.5 DECT-derived series

a) Alpha blending

Dual-energy scans can be acquired in different ways. For example, dual-layer detector and twin beam systems use a single-kilovoltage beam, usually set to 120 kVp, because it is the standard kilovoltage in CT imaging. However, dual-spiral, dual-source and fast kV-switching systems use two different beams that are not set to 120 kVp. Even though this setting has many advantages related to their better spectral separation, they lack the acquisition power of a real 120 kVp series. As these series are the standard in radiology and radiotherapy, it is necessary to derive pseudo-120 kV images from the low- and high-kilovoltage acquisitions. A simple solution for this problem is called alpha-blending.

Image blending can be linear or non-linear. Non-linear blending is based on modified sigmoid blending and operates voxel-by-voxel[7]. In this case, blending can increase the contrast-to-noise ratio by potentiating the brightest voxels (containing iodine) from the low-kilovoltage images and by using the lower noise characteristics of voxels in the high-energy kilovoltage image. Usually, non-linear blending is used to highlight a given characteristic of interest.

However, linear blending is more common because of its simplicity and good results. Linear calculation of alpha-blended images assumes that the 120 kVp CT numbers in the images can be expressed as a linear combination of those from the low- and high-kilovoltage scans. So, for a particular pixel:

$$\mathrm{CT(MIX)} = \propto \cdot \mathrm{CT}(\ \mathrm{kV_{low}}) + (1-\alpha) \cdot \mathrm{CT}\big(\ \mathrm{kV_{high}}\big)$$

where CT (MIX) are the CT numbers in HU in the virtual 120 kV images, usually called MIX series. Factor alpha must be adjusted to fit the correct values of CT numbers, and it depends on the CT system and the HU interval to fit. Thus, a low α value results in an enhancement of the high *Z* number components, such as iodine or calcium, and a high α value tends to reduce noise and reduce the influence of the photoelectric effect. The α value ranges from 0.3 to 0.7; the present study uses the 0.3 value, which assigns a higher weight to the high-kilovoltage images (**Figure 14**).

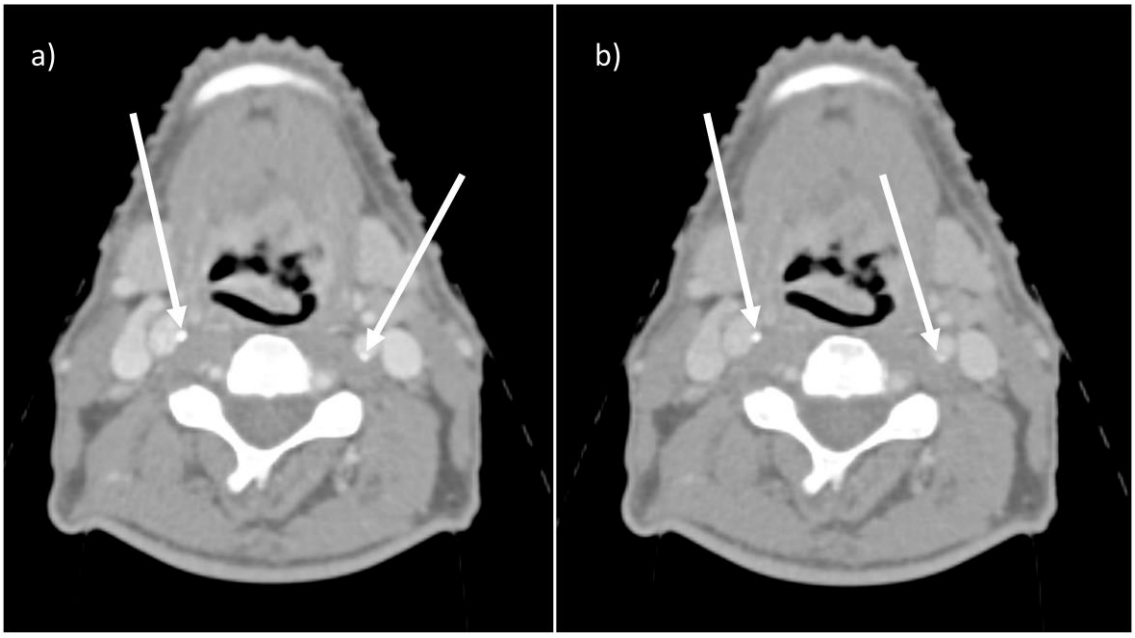

Figure 14. MIX images of different α values. a) With α = 0.7, iodine and calcium show a higher enhancement, resulting in a contrast increase. b) With α = 0.3, the image is more balanced and similar to a real SECT 120 kVp. Arrows point out calcifications in blood vessels that would be equal in both images if they were equivalent. However, they look different (author's data).

As the high-voltage images have a lower noise level, assigning them more weight reduces the overall noise. However, the relative increase in CT numbers from the photoelectric effect in high *Z* number materials introduces a higher uncertainty in the CT numbers calculated for them (**Figure 15**). This can affect images when iodinated contrast is introduced, because its *Z* number is higher than that of biological tissues. As calculations in RT planning can be done on contrast-enhanced images, the possible increase in dose uncertainty will be analyzed in this work.

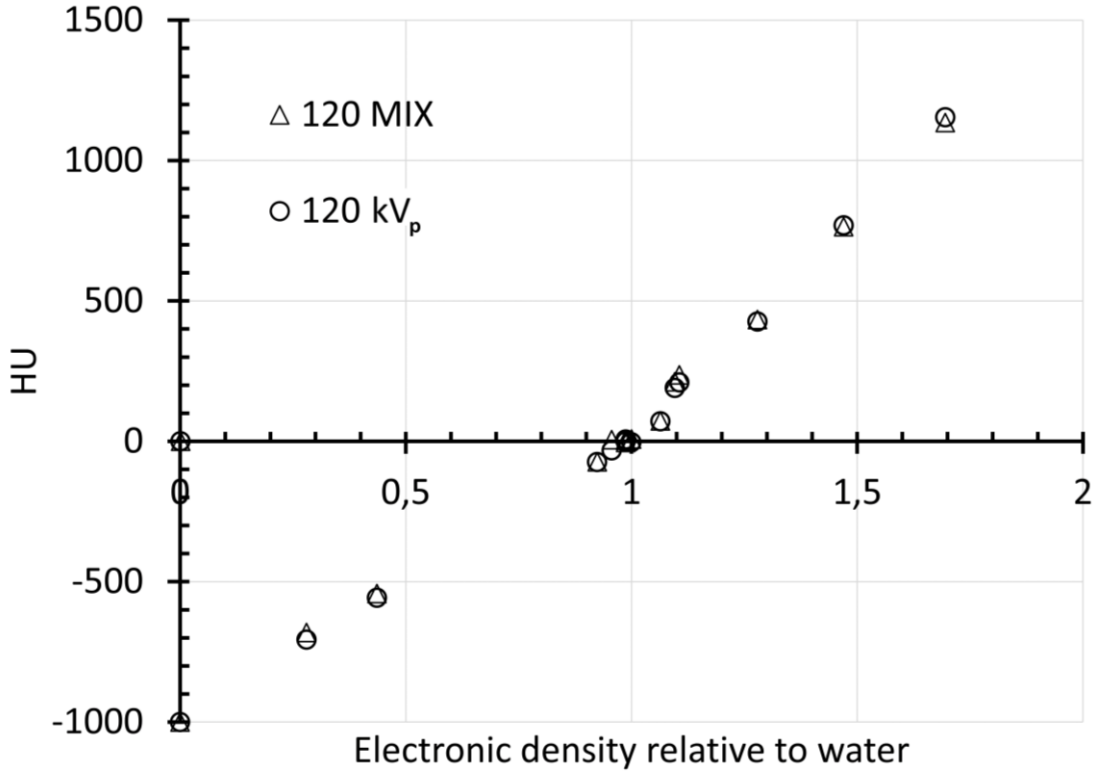

Figure 15. Calibration curves of real 120 kVp and MIX series obtained with a dual-spiral DECT Siemens Somatom Confidence RT Pro. Deviations are insignificant but tend to increase at high HU. Graph based on author's data.

Alpha-blended images can substitute real SECT 120 kVp. Even though their calculation is based on a simple linear assumption, several studies have demonstrated that the accuracy in CT numbers is better than 0.2%[8]. Although the standard α value gives good results in CT numbers, some authors have proposed ways to calculate α for each specific case[7] or for each particular voxel[9].

Due to the averaged basis of alpha-blended images, they show a lower noise level when compared to SECT 120 kVp images with the same patient dose. Additionally, as high-kilovoltage images show fewer artifacts produced by metal implants, MIX images also show fewer artifacts than SECT 120 kVp[10].

b) Material decomposition

Dual-energy CT is capable of separating different materials because of their different behavior when X-rays of different energies interact with them. Structures with high *Z* numbers present a much higher interaction at low energies than those with low *Z*. This effect is due to the special sensitivity of the photoelectric effect to *Z*. However, at high

energies, where only the Compton effect is relevant, those differences are small and related only to electronic density, which has small variations in the patient.

Separation of different materials at each pixel based on the properties of dual energy is called *material decomposition*.

Material information can be extracted from projection data through two different approaches: 1) in the projection space, subtracting equivalent projections and applying filtered backprojection to reconstruct the difference as spectral information; and 2) in the imaging space, after reconstructing standard CT images, by using postprocessing algorithms to extract specific spectral information from the difference between the corresponding voxels. This is the only possible approach when images at high and low kilovoltages are not taken at exactly the same time, as is the case with dual-spiral DECT. Dual-energy analysis is then performed on the dual-kilovoltage series using imaging-based algorithms. The present study analyzes DECT and material decomposition with the information obtained in the imaging space.

There are several methods for obtaining tissue composition in the imaging space. Until the recent introduction of photon-counting detectors, where the behavior of tissues at each energy beam results in a good characterization of materials, the main limitation of the decomposition algorithms has come from the information available, from just two points on the spectrum, high and low energy. When different elements, densities, and proportions are involved, the information provided from these two points does not permit the determination of the exact composition of tissues. So, to date there is no algorithm to precisely decompose patient tissues, a problem which several authors have tackled using different approaches, including basis material decomposition and Rho/*Z* decomposition.

- BASIS MATERIALS DECOMPOSITION

1- Two-materials decomposition

The attenuation of X-rays in the diagnostic energy range is mainly due to photoelectric and Compton effects. When the radiation spectrum is at an energy level that does not involve the K- or L- edges of the crossed materials, the attenuation coefficient of each

voxel can be expressed as a linear combination of photoelectric and Compton interactions, as proposed by Alvarez and Macovski[11].

$$\mu_x(E) = a_1 \frac{1}{E^3} + a_2 f_{KN}(E) \qquad \text{(Eq.2)}$$

μ_xI is the attenuation coefficient of material x for X-rays of energy E; F_{KN}(E) is the Klein-Nishina function, which depends only on photon energy; and a_1 and a_2 are factors that depend on the physical parameters of the material:

$$a_1 \approx K_1 \frac{\rho}{A} Z^n \, , n \approx 4$$

$$a_2 \approx K_2 \frac{\rho}{A} \, Z$$

At those approximate values, K_1 and K_2 are constants, ρ is mass density, and A and Z are atomic weight and number, respectively.

Each part of the sum in equation 2 represents one type of interaction. The first part, $1/E^3$, approximates the energy dependence of the photoelectric effect, while f_{KN}(E) accounts for the Compton scattering. That approach fits experimental data with less than 1% of the difference in the range from 30 keV and 200 keV (Rao and Gregg 1973, Phelps, Hoffman and Ter-Pogossian 1975).

Since the factors $1/E^3$ and f_{KN}I depend only on the energy, not on the material, equation 1 can be re-written as:

$$\mu_x(E) = x_1 \cdot f_P(E) + x_2 \cdot f_c(E) \qquad \text{(Eq.3)}$$

Where x_1 and x_2 are physical properties of material x, and f_p and f_c are functions that represent photoelectric and Compton interactions, independently of the material. In the CT acquisition, x_1 and x_2 are unknown for each voxel because of the mixture of different components and proportions.

A method to approximate each voxel composition is considering it as a mixture of only two components, the so called *two-material decomposition*. With this assumption, a particular voxel composed by a material x can be characterized by a proportion between two materials y and z, whose behavior is known. Equation 3 can be rewritten for all three materials as:

$$\mu_x(E) = x_1 \cdot f_P(E) + x_2 \cdot f_c(E) \qquad \text{(Eq.4)}$$

$$\mu_y(E) = y_1 \cdot f_P(E) + y_2 \cdot f_c(E) \qquad \text{(Eq.5)}$$

$$\mu_z(E) = z_1 \cdot f_P(E) + z_2 \cdot f_c(E) \qquad \text{(Eq.6)}$$

where $f_p(E)$ and $f_c(E)$ are independent of the materials, and y_1, y_2, z_1, and z_2 are known factors for the basis materials. Thus, from equations 3 and 4:

$$f_p(E) = \frac{z_2\mu_y(E) - y_2\mu_z(E)}{z_2y_1 - y_2z_1} \qquad \text{(Eq.7)}$$

$$f_c(E) = \frac{z_1\mu_y(E) - y_1\mu_z(E)}{z_1y_2 - y_1z_2} \qquad \text{(Eq.8)}$$

As $\mu_y(E)$ and $\mu_z(E)$ are known, equations 7 and 8 can be simplified:

$$f_p(E) = a_y\mu_y(E) + a_z\mu_z(E) \qquad \text{(Eq.9)}$$

$$f_c(E) = b_y\mu_y(E) + b_z\mu_z(E) \qquad \text{(Eq.10)}$$

Thus, introducing equations 9 and 10 into equation 4, the linear attenuation coefficient of the voxel can be rewritten as a linear combination of the basis materials as:

$$\mu_x(E) = A \cdot \mu_y(E) + B \cdot \mu_z(E) \qquad \text{(Eq.11)}$$

A and *B* depend only on the materials chosen as reference. In the two-material decomposition model, these values are considered the proportions of the component materials. To calculate them, two CT series at different energies must be acquired, so material decomposition is possible only with DECT.

Since Hounsfield Units are defined in terms of the linear attenuation coefficient (Eq.1), terms in equation 11 can be substituted by their equivalents in HU:

$$HU_x(E) = A \cdot HU_y(E) + B \cdot HU_z(E) + A + B - 1 \qquad \text{(Eq.12)}$$

Where $HU_x(E)$, $HU_y(E)$ and $HU_z(E)$ are the CT numbers of materials x, y, and z in HU, respectively. An additional condition exists due to the nature of the calculation itself: $A + B = 1$. This is the mass conservation constraint, where the quantities of the basis materials must equal the total mass of the voxel. With this assumption, Eq.12 becomes:

$$HU_x(E) = A \cdot HU_y(E) + B \cdot HU_z(E) \qquad \text{(Eq.13)}$$

CT numbers in HU can be extracted for a particular voxel in the image space, so it is possible to use any type of DECT to do such a decomposition. Dual-spiral DECT can therefore be used to decompose any voxel into basis materials.

The two-material decomposition model can be interpreted graphically as a change in a coordinate system. Basis materials can be considered as vectors (**Figure 16**), where the X coordinate shows HU at low kilovoltage (HU_{low}) and the Y coordinate at high kilovoltage (HU_{high}). Any unknown material can also be represented in the same diagram with its own values of CT numbers.

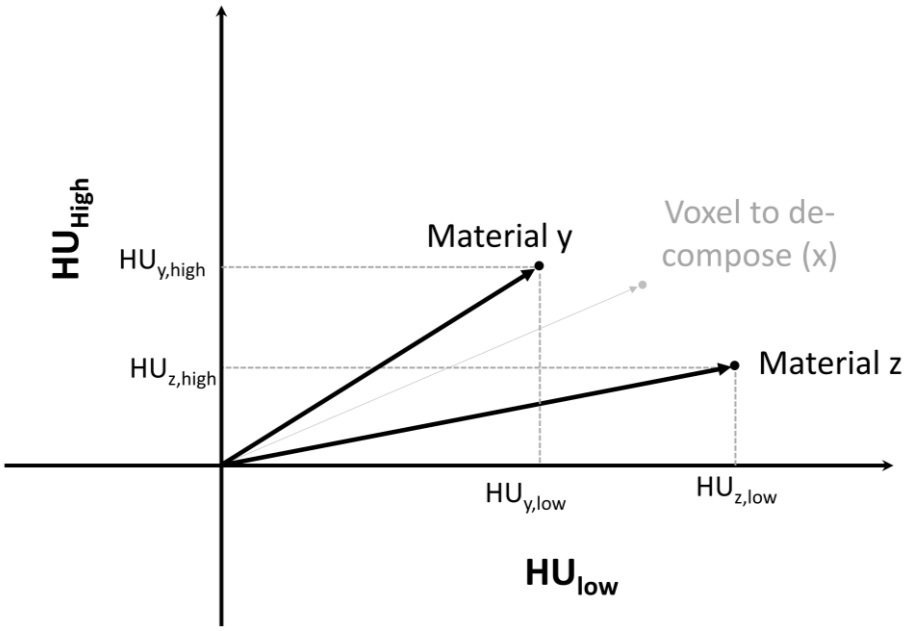

Figure 16. Representation of basis materials and the material to decompose in the image space at two different kVp. In this study, kV_{low} is set at 80 kVp, and kV_{high} at 140 kVp.

The z material vector ($HU_{z,low}$, $HU_{z,high}$) can be expressed as a combination of the two y and z basis material vectors: factors *A* and *B* in equation 13 (**Figure 17**).

In principle, any pair of known materials can be used as basis materials. In this work, all the Virtual Monoenergetic series have been decomposed by using the two-material decomposition based on the mixture of iodine and water.

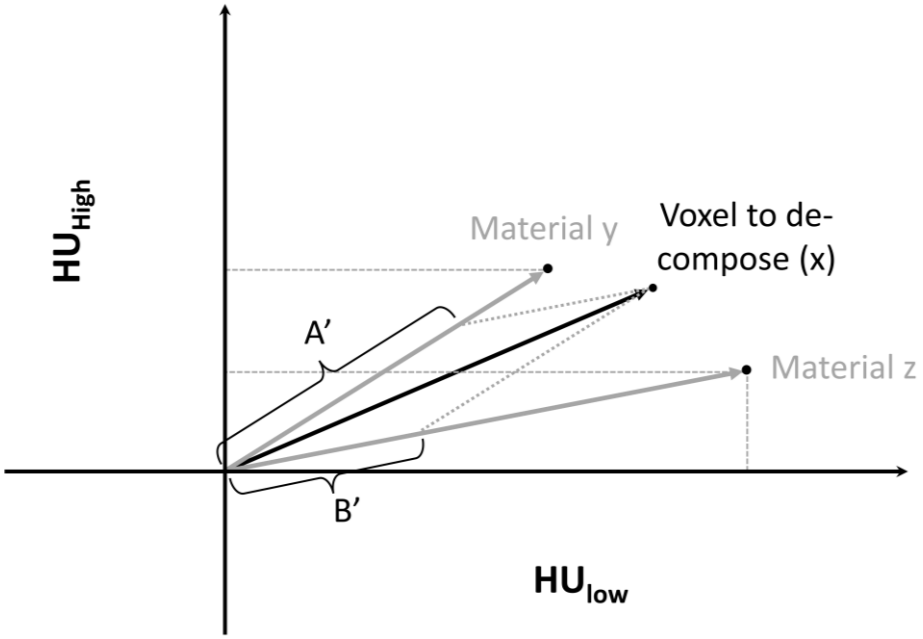

Figure 17. Vectoral projections of two materials. *A*' and *B*' are the projections of vector *x* on vectors *y* and *z*. The relative values of these projections are factors *A* and *B*.

2- Three-materials decomposition

The simplicity of the two-material decomposition cannot account for all the materials in a patient because not all components behave the same with respect to the CT numbers at high and low kilovoltage. A general rule is that tissue CT numbers decrease as kilovoltage increases. That rule is not valid for fat because the HU of fat increases when kilovoltage increases. As fat is an important component of the human body, some additional approaches must be considered.

The problem of adding a third basis material comes from the fact that only two kilovoltages are used in DECT. Equation 13 increases its complexity with a third factor, but only two equations form the equation system. A system with three unknown factors but only two equations has infinite solutions. The easiest way to deal with this problem might be to acquire a third series at a third kilovoltage. However, this is not a valid solution because such a decomposition would be unstable, as only two physical processes dominate the attenuation dependency on energy. Thus, additional assumptions must be

introduced in the model. One approach to this is the so-called **three-materials decomposition**.

That model assumes that three basis materials compose each voxel instead of two. There are two ways to deal with the problem: 1) volume or mass conservation, and 2) semiempirical methods to estimate the effective density when volume conservation is not present. Volume conservation assumes that the sum of the volumes of the three basis materials equals the total volume of the voxel, and mass conservation makes the same assumption with mass.

The most common methods are based on mass restriction, which assumes that the total mass of a given voxel equals the sum of partial masses. The reason why this is preferred over volume constraint is that most structures in the body act as dissolutions, where volume is not conserved. With that assumption, and considering y, z and m as basis components, the equation system from Eq.13 becomes:

$$\mathrm{HU_x}(E_{\mathrm{low}}) = A \cdot \mathrm{HU_y}(E_{\mathrm{low}}) + B \cdot \mathrm{HU_z}(E_{\mathrm{low}}) + C \cdot \mathrm{HU_m}(E_{\mathrm{low}})$$

$$\mathrm{HU_x}\left(E_{\mathrm{high}}\right) = A \cdot \mathrm{HU_y}\left(E_{\mathrm{high}}\right) + \mathrm{B} \cdot \mathrm{HU_z}\left(E_{\mathrm{high}}\right) + C \cdot \mathrm{HU_m}(E_{\mathrm{high}})$$

$$A + B + C = 1$$

Any set of basis materials is allowed for three-material decomposition.

One of the most interesting cases is when an iodinated contrast agent is injected into the patient. Reference materials x and y are usually fat and soft tissue, and the third component is iodine. Any voxel in the patient can be represented as shown in **Figure 16**. This allows the calculation of the relative iodine concentration and also its virtual removal. The procedure illustrated in **Figure 18** is as follows.

After determining the three reference materials, whose position in the dual energy plane is well known, the measured voxel *z* is represented. The iodine uptake is the line connecting the origin (water) with the iodine point *a*. A parallel line is created passing through voxel *z*. The virtual non-contrast position of the voxel is the point where that line crosses the connection between the other two materials. Finally, the position vector of point *d* can be obtained as a vectoral sum of vectors representing points *c* and *b*. The components of that sum are the relative proportions of materials *b* and *c*.

An important condition for such an analysis is that one of the three reference materials must show a relatively important photoelectric effect at low kilovoltage. This condition limits three-material decomposition to contrast agents (i.e., iodine or xenon) or specific biological compounds such as bone (calcium) or uric acid crystals. Additionally, to fulfill the requirements of mass or volume conservation, the reference materials must be selected in such a way that voxel *z* lays inside the triangle determined by points *a*, *b*, and *c* in **Figure 18**.

After three-material decomposition, there are two different ways to evaluate images:

- Virtually removing one of the three basis materials. This allows, for instance, VNC when iodine is removed, or virtual non-calcium when calcium is eliminated.

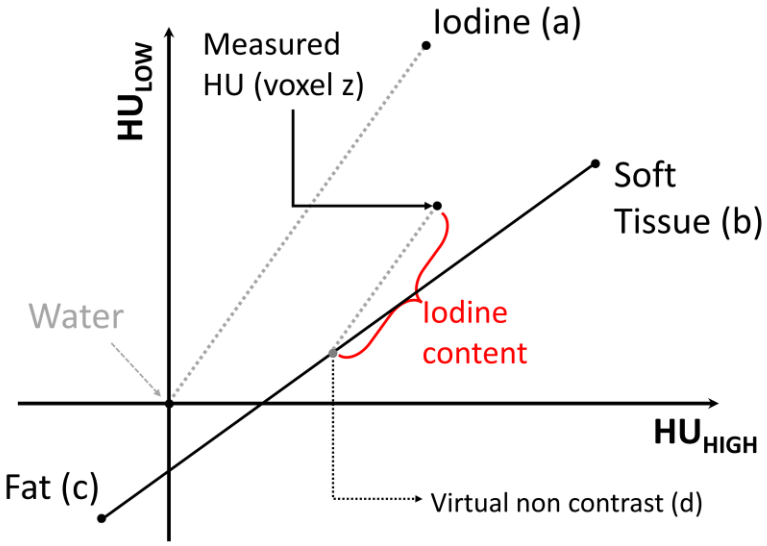

Figure 18. Three-material decomposition. *A*, *b*, and *c* are the known reference materials. *D* represents the virtual non-contrast position of the studied voxel *z*. The position of *d* depends on the reference materials. If bone is used instead of iodine, calcium density can be calculated.

- Elimination of two materials. These images show only the relative concentration of the component of interest. Examples of these are iodine, calcium, or fat maps (**Figure 19**).

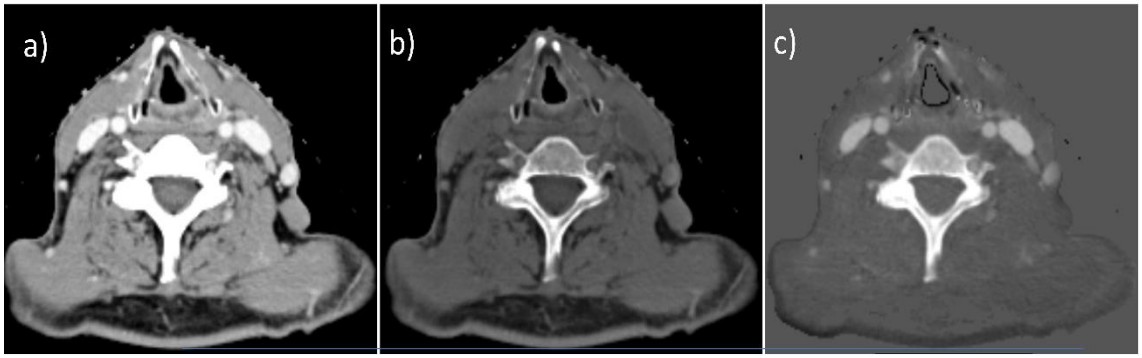

Figure 19. Images of a head and neck patient. a) SECT 120 kVp image of a head and neck patient. b) Virtual non-contrast (VNC) image of the same slice. c) Iodine map. Author's data.

The images obtained from two- or three-material decomposition do not reflect the real densities or compositions of the patient tissues. They show only the relative composition related to the basis materials, with the assumption that no other elements are involved. This assumption must be well understood when interpreting images because many other elements can be present, and their influence can be important in the final image shown.

Importantly, SECT images are shown in terms of relative absorption to water. As explained above, their values are expressed in HU. However, VMI, VNC, MIX, and virtual non-calcium series are derived from CT numbers at two kilovoltages and do not show real relative attenuation coefficients. Nevertheless, the units for CT numbers in those images are HU, even though they do not represent exactly the same measure. Moreover, that assumption does not affect definitions like uniformity, contrast-to-noise ratio, or contrast enhancement because their values are not unit-dependent and have no units.

3- Multi-material decomposition

Decomposing any tissue into all its component parts using only two points, as obtained by means of dual-energy systems, is not straightforward.

Mendonca et al. and Paulo et al.[12,13] proposed one approach to address that limitation, based on an algorithm that contains a database of reference material triplets with known behavior at low and high kilovoltages. That results in a *tessellation* of the CT numbers representation (**Figure 20**). Each voxel is then tested to find which of those triplets best fits the CT data and then decomposed in those three materials. Thus, reference materials can be different at each voxel.

The best solution for multi-material decomposition comes from the new photon-counting devices, which use a single X-ray beam but divide the whole spectrum in energy bins (**Figure 21**). The number and amplitude of bins is limited because of the detector's energy resolution, which depends on several effects, including signal splitting at pixel borders, energy loss due to K-escape for photons near the K-edge, or pulse pile-up due to the finite pulse width of the detected X-ray pulses.

Many multi-material decomposition algorithms have been proposed for photon counting devices. Those algorithms can work in the projection domain, the image space or iteratively in the reconstruction process between projection and image.

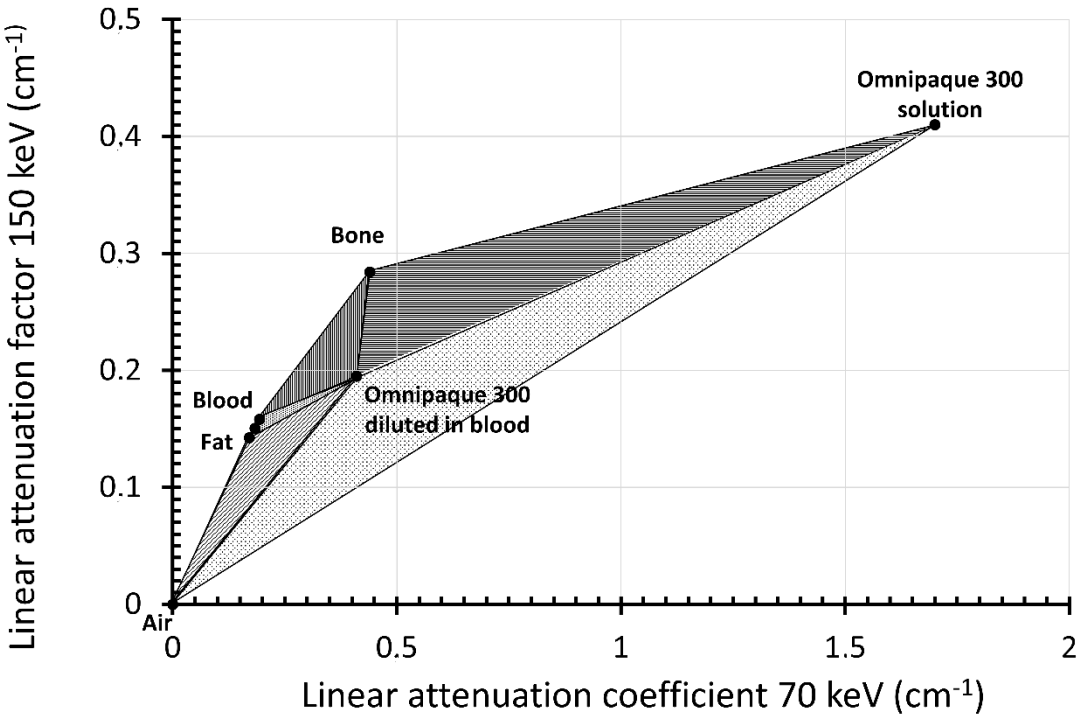

Figure 20. Tessellation of the linear attenuation graphic. Each triangle represents a triplet of basis materials. The selected triplet for each voxel is selected by the vertices of the triangle that encompasses the point of interest. Data from NIST database and Mendonça et al. 2014.

Typically, careful calibration of the basis materials and the imaging system are required when using spectral CT in the projection or reconstruction domains. Alternatively, and following the method proposed by Wang et al.[14] in the reconstructed images, it is possible to use a classification method for each energy bin to separate the voxel into different materials. This is similar to the two- and three-material decomposition models. Thus, traditional multi-material decomposition is based on the assumption that the linear

attenuation coefficient of a voxel *x* in the energy bin *e* (**Fig. 21**), $\mu_{x,e}$ is a linear combination of a set of basis materials:

$$\mu_{x,e} = \sum_{m=1}^{M} \omega_m \cdot \mu_{m,e}$$

Where ω_m is the volume fraction of basis material m, and $\mu_{m,e}$ is the linear attenuation coefficient of material m at the energy bin *e*, and *M* is the total number of basis materials.

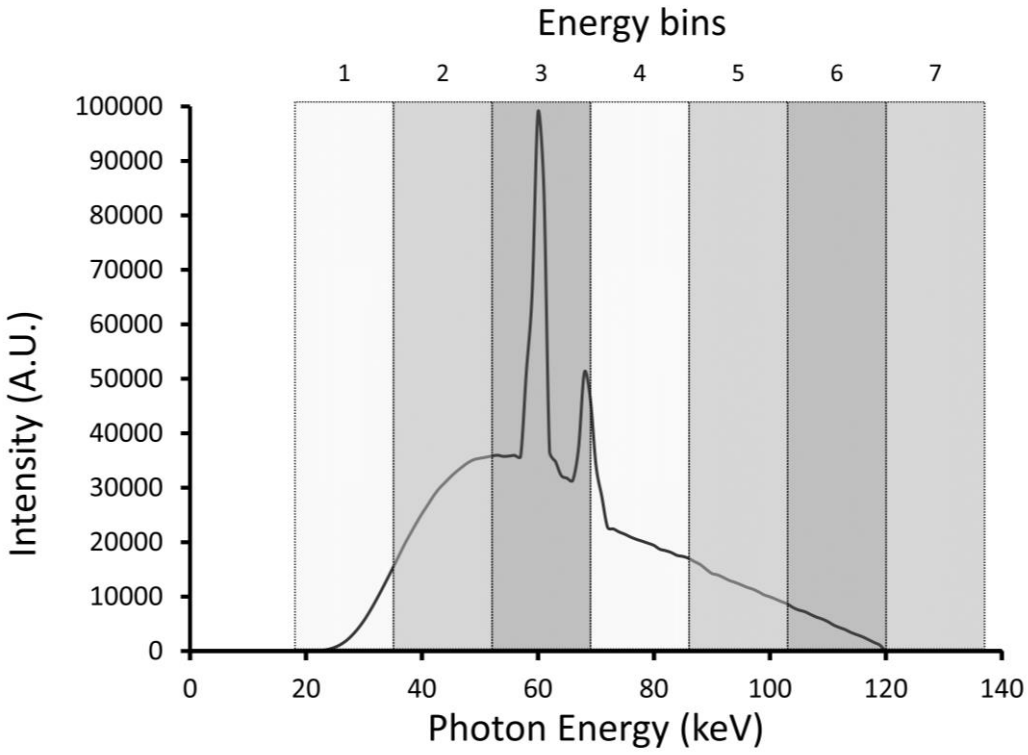

Figure 21. Division of X-ray spectrum in energy bins in a photon counting device.

- Rho/Z decomposition

DECT allows a different type of material characterization. Instead of determining a decomposition in basis materials, each voxel can be assigned a value of an effective atomic number Z_{eff} and electronic density ρ_e. The theoretical principles of those calculations were well established and experimentally verified in the first years of computed tomography[15].

Rho/*Z* decomposition is based on the solution to equation 2. The linear attenuation coefficient of any material can be separated into two parts, one due to the photoelectric effect and the other representing Compton scatter.

The behavior of the real voxel, which is a complex composition of different elements at two different kilovoltages, is compared to a hypothetical material with a single composition and whose atoms are identical. This material is characterized by an effective atomic number Z_{eff} and an electronic density ρ_e (Rho). Both the real and the hypothetical materials are supposed to have the same linear attenuation coefficients at both low and high kilovoltage.

Z_{eff} can be expressed as a combination of the elemental components of the voxel as

$$Z_{eff} = \sum_i \omega_i \cdot Z_i^n$$

Where ω_i is the fraction of the total number of electrons due to material i with atomic number Z_i. Exponent n is an experimental constant whose values are 3 to 4 (n = 3.5 in American Association of Physicists in Medicine [AAPM] Task Group report TG 291[16]).

With the previous assumptions, equation 2 can be rewritten. The real voxel x is composed by i elemental components, each one with an atomic number Z_i and a number of atoms per unit volume N_i. Its linear attenuation coefficient at energy E can be expressed as

$$\mu_x(E) = \sum_i f(Z_i, E) \cdot N_i \qquad \text{(Eq.14)}$$

Considering two scans at energies E_1 and E_2, the equivalent material fulfills two conditions:

$$\mu_x(E_1) = \mu_{eq}(E_1) \text{ and } \mu_x(E_2) = \mu_{eq}(E_2) \qquad \text{(Eq.15)}$$

Thus, with the assumption that the equivalent material has only one component whose atomic number and number of atoms are Z_{eff} and N_{eq}, respectively:

$$\mu_x(E_1) = \sum_i f(Z_i, E_1) \cdot N_i = f(Z_{eff}, E_1) \cdot N_{eq} \qquad \text{(Eq.16)}$$

$$\mu_x(E_2) = \sum_i f(Z_i, E_2) \cdot N_i = f(Z_{eff}, E_2) \cdot N_{eq} \qquad \text{(Eq.17)}$$

Dividing equations 16 and 17,

$$\frac{\mu_x(E_1)}{\mu_x(E_2)} = \frac{f(Z_{eff},E_1)}{f(Z_{eff},E_2)} \qquad \text{(Eq.18)}$$

Since equation 18 depends only on Z_{eff}, the most common practice is to determine a calibration or simulation curve of the ratio $\mu_x(E_1)/\mu_x(E_2)$ for the specific CT device and spectrum (**Figure 22**).

When Z_{eff} has been calculated, it is straightforward to calculate the electronic density of the voxel because electronic density and Z are related by the expression:

$$\rho_e = \frac{\rho}{A_m} \cdot Z \cdot N_A$$

Where ρ_e and ρ are the electronic and mass densities, A_m is the atom mass, and N_A is Avogadro's number.

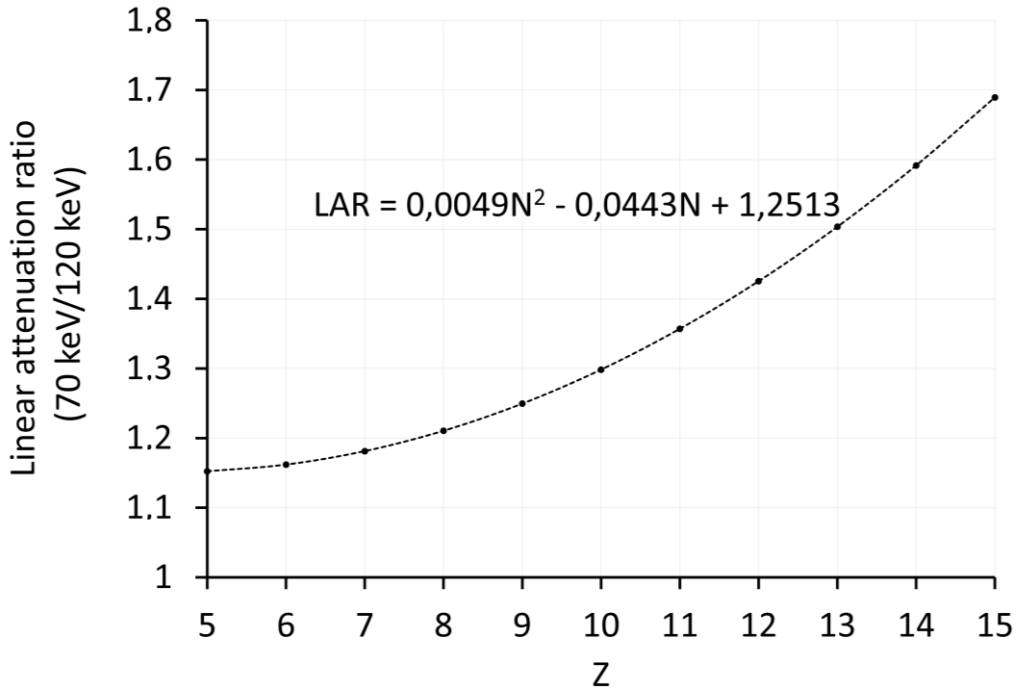

Figure 22. Experimental linear attenuation ratio between 70 keV and 120 keV. The equation represents the quadratic fit. Source: AAPM TG 291.

1.2.6 Applications of dual-energy CT

Each of the aforementioned features of DECT has been used to create different imaging series that provide different information. Thus, alpha-blended images substitute real

SECT 120 kVp series; material differentiation can be used to create virtual non-calcium, virtual non-contrast and virtual monoenergetic series; and Rho/*Z* series give information about material properties. Each type of series has multiple applications that are increasing as DECT is being adopted by more hospitals. Nevertheless, several have been established in clinical practice and are described below.

a) Applications of alpha-blended (MIX) images

The main characteristic of MIX images is their similarity to real SECT 120 kVp images. However, they show a higher CNR when iodine contrast is injected into the patient. This is because even though the high-kilovoltage images are given more weight, iodine increases its attenuation factor in a nonlinear function in the low-kilovoltage images.

MIX images are usually created in addition to other DECT series. In the DECT systems that do not split the 120 kVp spectrum, like dual-spiral, dual-source, and fast kV-switching systems, the acquisition does not have a standard 120 kVp series. In many cases these images are necessary, and the way to deal with this problem is to acquire an additional SECT scan. The MIX series fill this gap. They can be used with or without contrast enhancement. Thus, their main application is to avoid the need for an additional scan at 120 kVp. This helps maintain the radiation dose with DECT at the same values referenced for SECT studies.

b) Applications of material decomposition

The most important application of two-material decomposition is creating VMIs. As detailed above, any voxel in the patient can be described as a combination of two known materials. Once the relative weights of these materials have been adjusted to fit HU values at the high and low kilovoltage, the behavior of the pixel at different energies can be derived from the attenuation curves of both materials. The only restrictions are that the energy must be higher than the k-edge of both materials and that equation 2 must be applicable. As VMIs are commonly created with iodine and water as basis materials, the interval where both conditions are fulfilled ranges from 40 keV to 150 keV.

Although monoenergetic images are derived from datasets acquired by means of two beams with complex spectra, VMIs have physical characteristics very similar to images acquired with real monoenergetic beams. As a result, beam-hardening artifacts are not an

issue, especially at high energy levels. This is one application of VMIs in medicine when iodine contrast is not injected: reduction of CT image artifacts. Several studies have shown this application in metal implants, foreign metal bodies, vascular calcifications, and artifacts produced by a high iodine contrast uptake[17,18,19]. Moreover, the combination of high-energy VMIs of at least 100 keV and iterative metal artifacts reduction algorithms (IMAR) can be one of the best combinations to reduce such artifacts in CT imaging[20].

The application of VMIs to reduce artifacts was not studied here because in a clinical situation, iterative algorithms perform better in this regard. For RT planning IMAR algorithms reduce the artifacts and are also dose neutral to the patient. Therefore, it is not a common practice to use DECT with this purpose.

VMIs are typically used with iodine contrast injected into the patient. At low energies, iodine's attenuation factor increases dramatically, as shown in **Figure 6**, but so does noise. Those characteristics produce a high-contrast enhancement of iodine at low energies. Even though calculation of VMI generates an increasing noise level when energy decreases, the CNR at low energies is high enough to distinguish areas in the patient with low contrast uptake. This has applications in vascular and oncological imaging[21,22,23].

As contrast enhancement is high, low keV VMIs can be used in low iodine-dose environments. One application is the reduction of the iodine dose injected into the patient. Thus, many reduction protocols use VMI. This is an important feature in patients with impaired renal function.

Three-materials decomposition is used in a different way. Since any pixel is split in three basis materials, there are different possibilities of use:

- Virtual removal of one of the three basis materials. In this case the resulting image consists in a combination of the contributions of the other two. This is the case of Virtual Non-Contrast (VNC) images, that are obtained from iodine-enhanced acquisitions and where the removed material is iodine, and Virtual Non-Calcium (VNCa), where the removed material is Calcium in non-enhanced images.
- Virtual removal of two components. The resulting images have CT numbers proportional to the specific weight of the remaining material. These are the cases of Iodine, calcium and uric acid maps.

Material decomposition has many clinical uses, summarized below.

- **Abdomen**

Liver. Multiple studies have shown the potential advantages of VMI[24,25,26] in hypervascular liver lesions. They can also be useful in hypoenhanced lesions like hepatic metastases[27]. However, image quality can be compromised, especially at very low energies in large patients[28].

Pancreas. VMIs overcome the limitations of the low-contrast conditions in classical SECT. Some authors have shown that they can help to distinguish small pancreatic adenocarcinoma from normal parenchyma[29,30].

Kidney. VMIs have been used to improve the imaging of solid and non-solid renal tumors. Renal cyst pseudo-enhancement remains a common issue in CT of the kidney, but VMI reconstructions have been shown to minimize or even overcome this problem while maintaining kidney contrast enhancement similar to standard CT acquisition[31,32].

Bowel. VMIs perform better than SECT in the detection of early bowel ischemia in an acute setting[33]. They have been also introduced to complement the SECT series in the assessment of Crohn's disease and in the diagnosis of gastrointestinal tumors[34].

- **Lung**

DECT has multiple uses in lung imaging, including for acute and chronic pulmonary embolism, chronic thromboembolic pulmonary hypertension, vascular abnormalities, and parenchymal diseases[35,36] (**Figure 23**). The addition of xenon to the inspired air allows visualization of gas diffusion through the lung. The *Z* number of xenon is 54, only one unit higher than that of iodine. Low-energy VMIs are especially sensitive to this gas[36,37,38]. The combination of imaging with injected iodine, which also produces perfusion images with high sensitivity at low VMI energies, allows a complete diffusion/perfusion study of lung function.

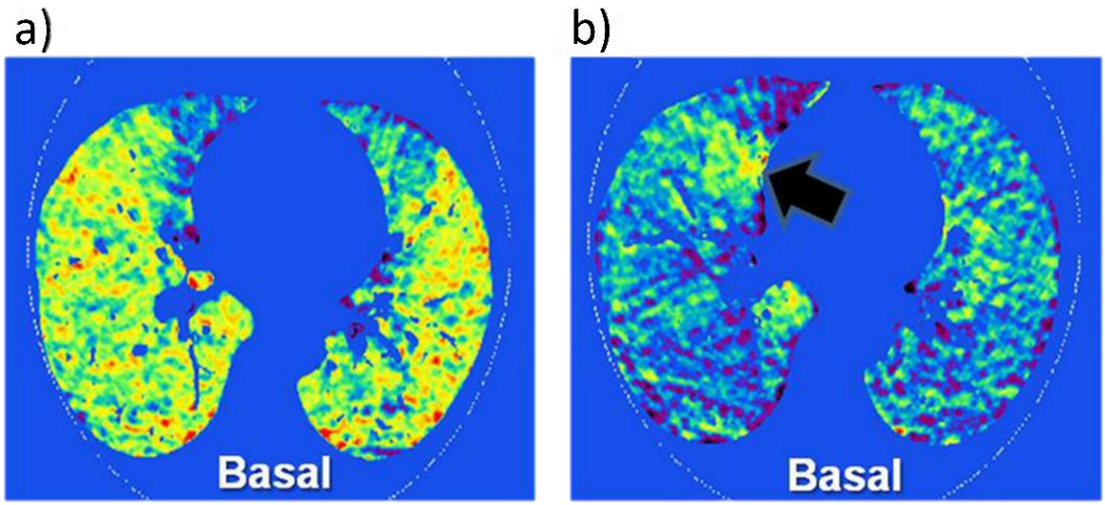

Figure 23. Wash-in and wash-out xenon-enhanced DECT for evaluation of dynamic ventilation in a patient with asthma. Arrow in b) shows focal gas trapping. From Hwang et al 2017[38].

- **Cardiovascular system**

Coronary vasculature and functional evaluation of the myocardium with DECT show comparable results to that of MRI and single-photon emission computerized tomography (SPECT). However, the presence of metallic components as stents or pacemaker wires, a high concentration of iodine in the right heart, or extensive calcifications, may negatively affect CT images. VMIs can improve these impairments through mechanisms like a lower iodinated contrast dose at low energies[39] or the reduction of artifacts at high energies[40].

Three-material decomposition can be used to acquire iodine and calcium maps, enabling the subtraction of vessel calcifications and improving vessel lumen identification. Additionally, fat maps can be used to detect lipid-rich plaque, and iodine/water maps to assess organ perfusion, especially in the lung and heart.

- **Head and neck**

Iodine quantification, virtual non-contrast image reconstruction, and bone removal in DECT angiography have been applied in head and neck imaging. Authors like Beland et al.[41] have used VNC images to improve the diagnosis of salivary gland stones, while virtual non-calcium studies have been used to evaluate bone marrow edema or tumor infiltration[42,43]. VMIs have also been investigated by many authors for head and neck

imaging because of their increased vascular and brain tissue contrasts when iodine contrast is present (**Figure 24**).

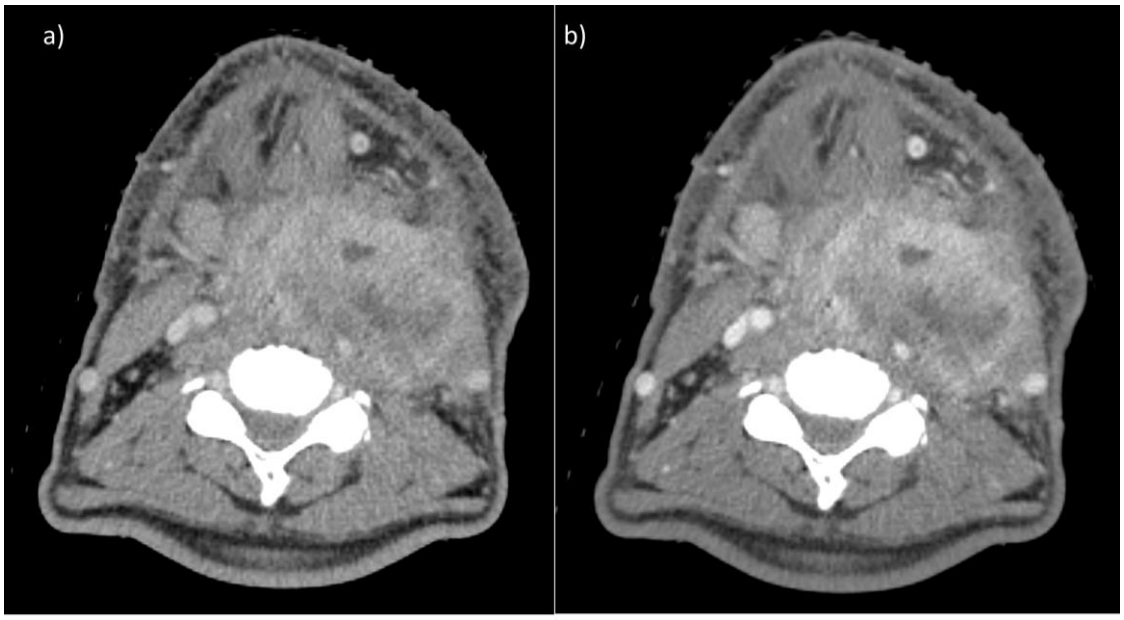

Figure 24. Iodine enhancement of 40 keV VMI. a) SECT 120 kVp image. b) Same slice at VMI 40 keV. The contrast of blood vessels shows such an important enhancement in the VMI that the perfect delineation of vessels is possible. Author's data.

Stolzmann et al. showed the usefulness of DECT VMIs to reduce artifacts due to metal implants[44], while Tanaka et al. found out that 100 keV VMI improved bone diagnosis around the implants[45] (**Figure 25**). These results can be even better with the addition of IMAR algorithms, as shown by Bongers et al.[46]

DECT has many applications in head and neck oncology. Multiple studies have shown that VMI series improve tumor visibility, identification of soft-tissue tumor boundaries, and determination of the extent of the local tumor[43,47,48]. Additionally, a comparison of VMI at low versus high keV can be useful in evaluating thyroid cartilage invasion for proper staging of laryngeal and hypopharyngeal cancers[49]. Using DECT iodine maps can be even more specific than MRI to evaluate that invasion[50]. Low energy VMI may also be used to improve visibility of pathological lymph nodes[51], and in radiotherapy of the head and neck, VMI series can be used for better delineation of gross target volumes (GTVs) and lymph nodes, while MIX and VNC images can be used for dosimetry calculations. These applications will be described and analyzed in depth in chapter 4.

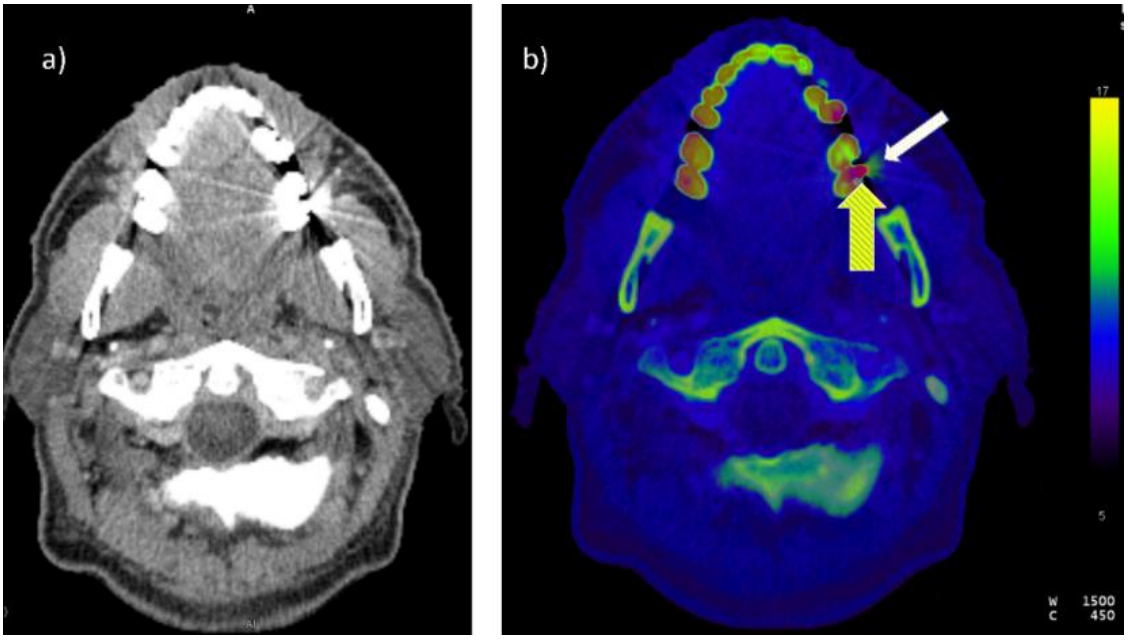

Figure 25. Rho/Z images of a metal implant in the 120 kVp series. a) Rho/Z image b) allows the separation of metal implants from bone (yellow arrow) and the delimitation of artifact (white arrow). Author's data.

- **Musculoskeletal system**

DECT decomposition is currently being used to diagnose gout and bone marrow edema, assess bone mineral density, and reduce metal artifacts. Conventional CT and MRI have failed in the diagnosis of early-stage gout, but DECT has proven efficacy at such stages[52] and is commonly used in clinical practice. Nevertheless, some recent studies show that ultrasounds can be better than DECT for those diagnoses[53,54]. In contrast, material labeling has shown good outcomes for identifying acute gout and following up urate deposits[55,56].

Bone marrow edema secondary to trauma is normally diagnosed by MRI. However, long acquisition times may require potentially painful patient positioning. Conventional CT has less sensitivity in that diagnosis because it is not able to remove fine bone trabeculations. On the other hand, DECT can overcome that limitation due to its capacity for material characterization. As DECT can remove the calcium signal, it provides a superior characterization of bone marrow edema[57,58].

Finally, the World Health Organization guidelines established dual X-ray absorptiometry as a reference standard for osteoporosis assessment and diagnosis. However, this

technique is particularly susceptible to image distortions due to overlying structures and distortions secondary to osteodegenerative changes of the spine. DECT has been proposed as an alternative for 3D volumetric assessment of bone mineral density, but there are still some concerns about radiation dosing that must be studied[59].

c) Applications of Rho/Z images

One challenge in proton radiotherapy is the determination of the stopping power ratios of each medium to water, because calculation algorithms need that factor to determine the proton range at different energies. DECT has the capacity to calculate electronic density (ρ_e) and effective atomic number Z_{eff}, a feature that has limited accuracy with SECT[60,61].

Calculating the stopping power ratio from DECT is currently based on work by Yang et al.[62], which fits Z_{eff} with the logarithm of the mean excitation potential and achieves an accuracy in human tissues within 2% of the stopping power ratio, according to recent studies[63,64], while accuracy is about 7% when using SECT.

Rho/*Z* images can be also used for separation of various materials inside organs or tumors. Some authors, such as Mileto et al.[65], have shown that non-enhancing renal cysts can be discriminated from enhancing tumors on Z_{eff} maps. Additionally, separation of materials by their Z_{eff} can be useful to evaluate regions closer to metal implants like the one shown in **Figure 25**.

1.2.7 Dual energy in radiotherapy of head and neck tumors

According to the medical dictionary of the National Cancer Institute, head and neck tumors are those that arise in the anatomical region of the head or neck (nasal cavity, sinuses, lips, mouth, salivary glands, throat, or larynx) (**Figure 26**). These tumors account for nearly 4% of all cancers and are more than twice as common in men compared to women. Treatment includes surgery, radiotherapy, chemotherapy, immunotherapy, or a combination of these. This work focuses on patients treated with external beam photon radiotherapy.

There are different RT treatments for the head and neck region: local treatment of the tumor bed (in case it has been operated) or the tumor itself, treatment of the tumor (or bed) plus regional lymph nodes, or treatment of the lymph nodes only. Whatever the

treated volumes are, radiotherapy of the head and neck is complex because of the proximity of many crucial organs that need to be protected, such as the spinal medulla, and side effects of the treatment could seriously compromise the patient's quality of life.

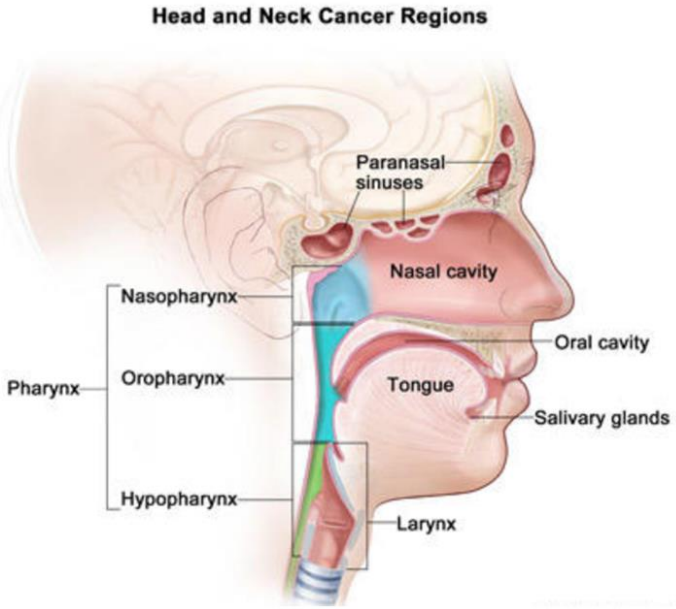

Figure 26. Head and neck region. Picture from National Cancer Institute.

Thus, accurate delineation is absolutely essential in radiotherapy[66], especially in the head and neck region. In head and neck patients, radiation doses prescribed to treat the tumors are as high as 70 Gy, well above the tolerance threshold for OARs. **Table 2** details some examples in that regard.

Table 2. Organs at risk and tolerance doses in the protocol for head and neck radiotherapy at Hospital del Mar (Barcelona, Spain)

Organ at risk	**Tolerance dose**
Spinal cord	Max 45 Gy
Parotid gland	Mean dose < 20 Gy
Pharynx constrictors	Max 50 Gy
Oral cavity	Max 27 Gy at 50% of volume
Mandible	Max 55 Gy at 20% of volume
Thyroid	Max 45 Gy at 50% of volume
Esophagus	Mean dose < 34 Gy

Moreover, the geometry of tissues in the head and neck area is complex, and sometimes regions to treat surround the OARs or are close to them (**Figure 27**).

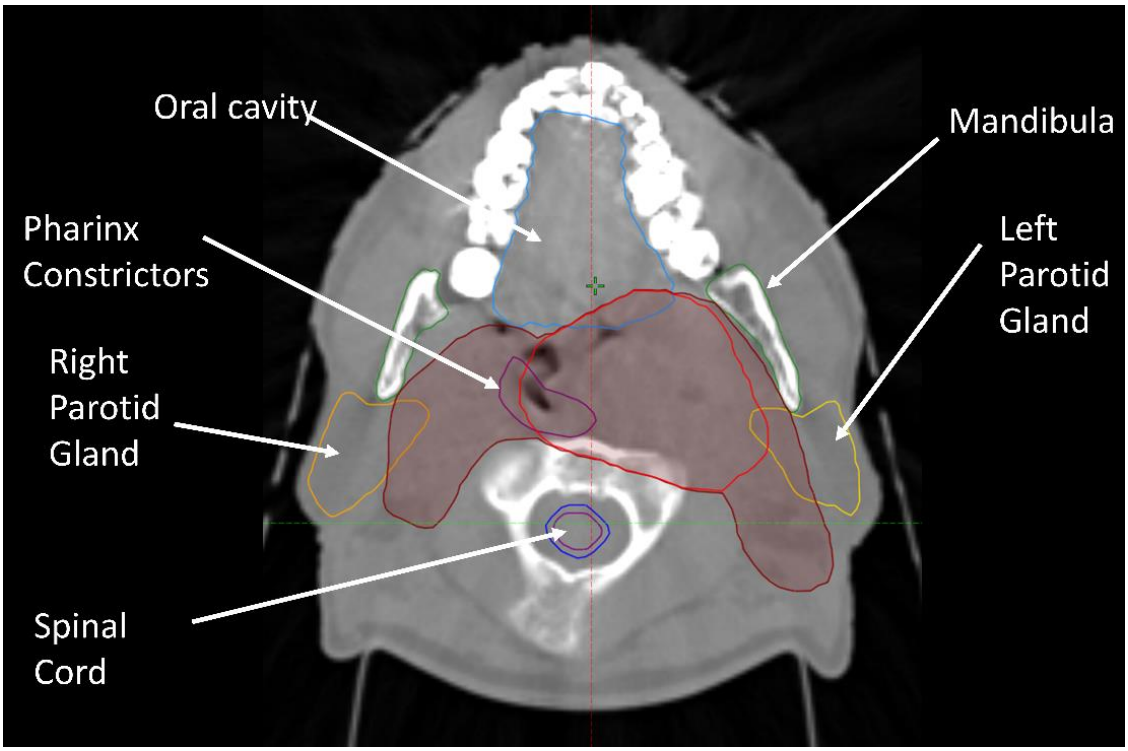

Figure 27. Structure set of an RT treatment in the head and neck area. The red line represents the planning target volume (PTV) of the tumor, whose planned dose is 70 Gy. The brown line corresponds to the lymph nodes PTV, with a dose of 50 Gy.

The proximity and shape of OARs to the tumor increases the complexity of RT treatments and necessitates high precision in both treatment and organ delineation. Precision in organ delineation strongly depends on the differences in the HU of tissues. Unfortunately, CT images do not have a high contrast between soft tissues because of the predominance of the Compton effect. Nevertheless, it is common practice in RT organ segmentation to increase tissue differences by means of an IV injection of iodinated contrast. As iodine has a high atomic number (Z = 53), its administration produces image contrast due to differential photoelectric absorption (**Figure 28**). Moreover, as the k-edge of iodine is 33.2 keV, photons with energies near that value show a high increase in absorption, which is reflected in a high increase of CT numbers in the low-kilovoltage CT images. Contrast agents used in this work were ioversol (Optiray) and iohexol (Omnipaque), two water-soluble, low-osmolality (less than three times the osmolality of human serum) iodinated compounds.

CT images are used in radiotherapy in two steps of the treatment workflow: 1) delineation of tumors and OARs, and 2) dose calculations. DECT is a promising technology in both steps because it can overcome some limitations of the classical SECT images.

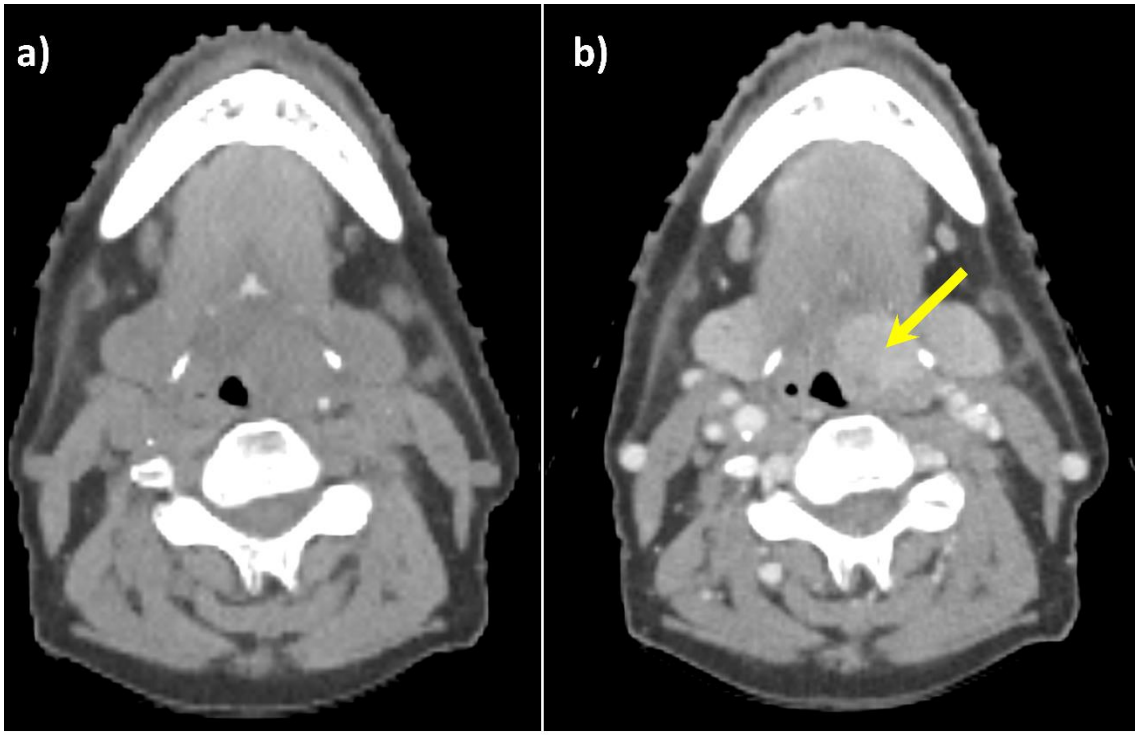

Figure 28. Images of the same tumor a) with and b) without injected iodine. Both were acquired at the standard 120 kVp. Window settings are the same (center = 0, window = 400). In b), tumor (yellow arrow) is clearly visible.

a) DECT in tumor delineation

According to International Commission on Radiation Units (ICRU) reports 50 and 62[67,68], delineation of structures for RT treatments must include different types of volumes.

- **Volumes to treat**

- **GTV**, corresponding to the macroscopic tumor boundaries as determined by means of imaging techniques.
- **Clinical target volume (CTV)**, usually derived by applying an additional margin to the GTV and intended to include subclinical disease that cannot be determined by imaging techniques. In case GTV is not present, the CTV can be delineated with the help of pre-treatment images or by anatomical boundaries. As CTV can suffer position displacements and variations of shape and volume, an internal margin can be defined.

- **Internal target volume (ITV)**, defined as the volume that includes both internal margin and CTV.
- **Planning target volume (PTV)**, defined by an additional margin to the internal target volume. It encompasses all the geometrical uncertainties due to patient or organ motion, equipment, and positioning uncertainties. It must also consider intra- and inter-fraction deviations of the treatment. PTV is a geometrical concept used in treatment planning to assure that the CTV receives the prescribed dose.

- **Volumes to protect**

In correspondence with target definitions, which are volumes to be treated, OARs must also be defined. An OAR is a normal tissue whose sensitivity to radiation can limit or affect treatment planning or prescribed dose. As OARs should be protected as much as possible in an RT treatment, planning organ at risk volume (PRV) is created in parallel with PTV to include any movement of the OARs during the treatment as well as positioning uncertainties.

A schematic view of volumes can be seen in **Figure 29**.

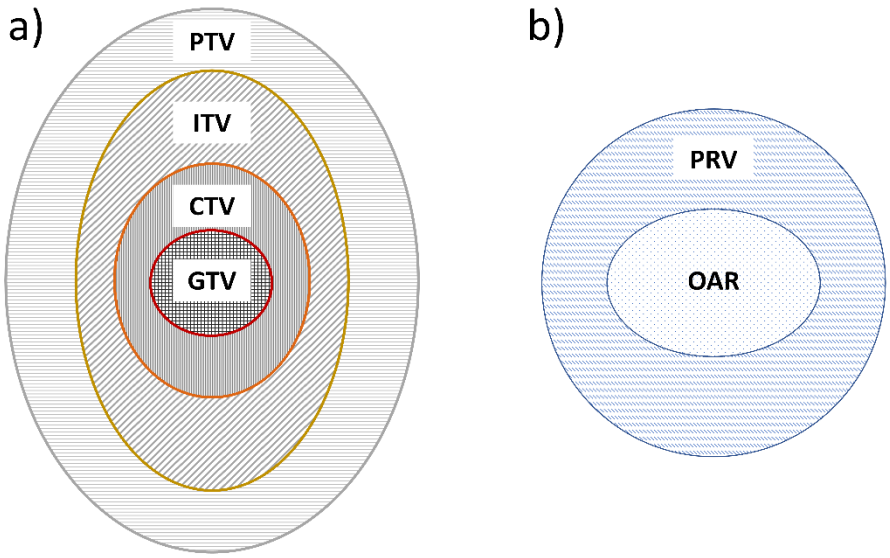

Figure 29. Relative positions of a) target volumes b) and organs at risk (OARs). For anatomical reasons, the planning organ at risk volume (PRV) usually intersects with one or several target volumes, a situation where clinicians must decide the balance between the dose at planning target volume (PTV) and the dose at OAR.

Treatments in the head and neck regions are complex because several OARs of critical importance, like the spinal cord, tend to be located in close proximity to the high-dose PTVs. It is therefore crucial to correctly delineate structures with the fewest possible uncertainties. Target volume delineation is strongly dependent on the accuracy of GTV identification because CTV and PTV are usually defined as GTV plus a geometrical margin[69].

RT planning is done on CT images. Standard acquisitions are at SECT 120 kVp. As 120 kVp images have a low contrast between soft tissues, it is a common practice to acquire images with iodinated IV contrast. When iodine is injected, imaging contrast increases (see **Figure 28**). However, iodine may affect dose calculations.

Despite the use of iodine, 120 kVp images still do not take full advantage of the possibilities of contrast addition. It is well known that low-kilovoltage acquisitions with iodine (i.e., 80 kVp) have a higher contrast than 120 kVp (**Figure 30**) and allow a better delineation of tumors.

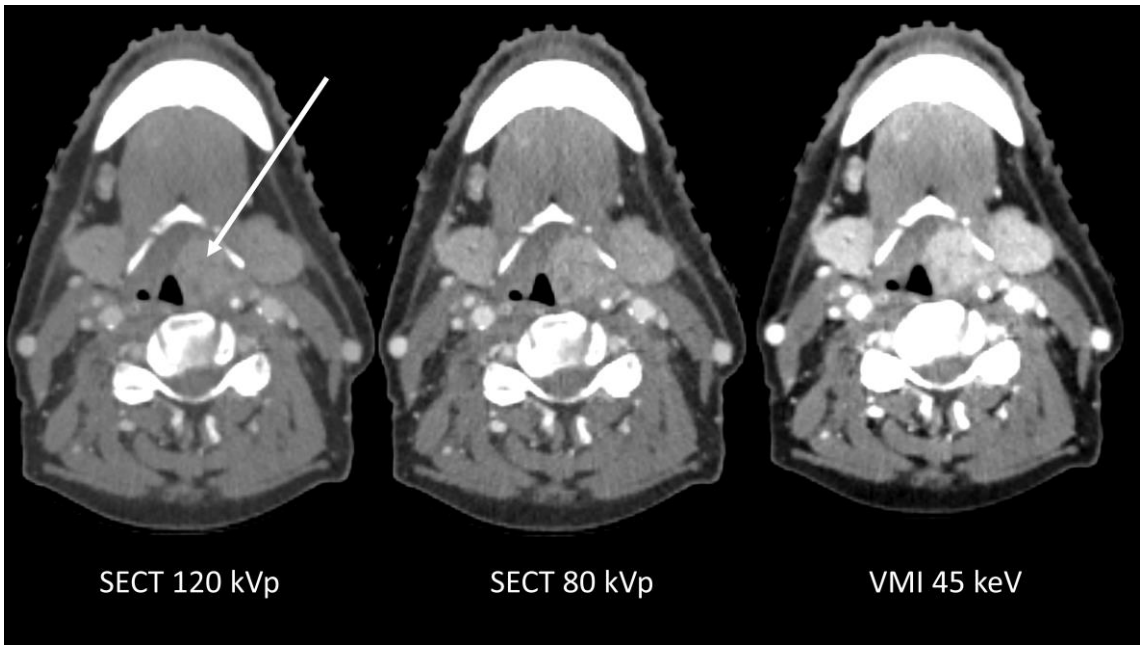

Figure 30. Acquisitions with iodinated contrast at SECT 120 kVp, 80 kVp, and 45 keV VMI. With the same windowing characteristics (c = 75, w = 350), differences in contrast are clearly visible, especially in the central area where the tumor is present. VMIs shows far higher contrast than SECT images.

However, images at low kilovoltage are not commonly used for RT planning because of their relatively high sensitivity to the photoelectric effect, which is not present at the usual

RT treatment energies (above 1 MV). For that reason, when the acquisition protocol includes a low-kilovoltage series for delineation, an additional 120 kVp is acquired for planning.

Radiation oncologists have a different way of dealing with that problem. DECT provides more information to the delineation process and takes better advantage of iodinated contrast.

- On the one hand, a DECT study includes the low-kilovoltage series, but it can also create VMIs that enhance contrast even more than 80 kVp images. As VMIs can be created in a wide range of energies, oncologists can determine which are the best for delineation, including artifact reduction. VMI series have demonstrated superior delineation characteristics in many studies[70,71,72].
- On the other hand, although DECT studies do not have a directly acquired 120 kVp series, it is possible to virtually blend the MIX series, which have similar characteristics to those of SECT 120 kVp. The MIX series can be used both for structure delineation and planning calculations. Radiotherapy departments that do calculations on enhanced images can use MIX series instead of SECT for such calculations.

b) Dual energy in RT planning

Medical physicists plan RT treatments after volume delineation. Planning has different steps depending on the technique applied. Currently, there are three main techniques in external beam photon radiotherapy: 3D static conformal fields, intensity-modulated fields, and volumetric modulated arc therapy (VMAT). All three techniques are planned on CT images. The accuracy of calculations strongly depends on the accuracy of the image acquisition and CT number of each voxel in the images.

Treatment planning systems are computed programs used to calculate RT doses in target volumes and OARs. In a first step, they convert the CT number of each pixel to the equivalent electronic density that determines the absorption of radiation due to the Compton effect at the treatment energy. This step is done by means of a CT calibration curve that depends on the CT scanner and the X-ray spectrum and energy (**Figure 31**).

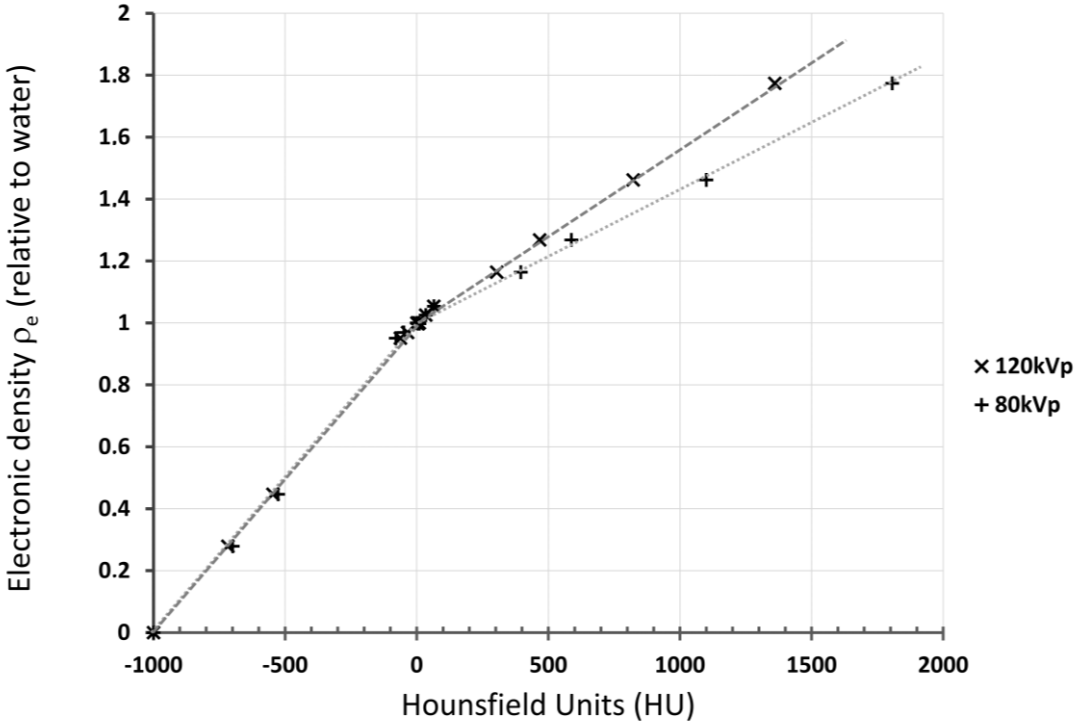

Figure 31. Calibration curves of the Siemens Somatom RT Pro at Hospital del Mar. Curves at SECT 120 kVp and 80 kVp are clearly different.

Since CT numbers depend on electronic density, they are affected by the injection of iodine. Thus, IV contrast has an influence on calculations. When only SECT acquisitions are used, there are two ways to deal with this problem:

1) Acquisition of two series: the first one before iodine injection at 120 kVp, which is meant to be used for dose calculations and planning, and the second one after injection for volume delineation. The series for volume delineation can be at low kilovoltage to increase iodine enhancement and improve structure segmentation.
2) Acquisition of only one series at 120 kVp with iodinated contrast, used for both delineation and calculations. In this case, some degree of increased uncertainty is accepted, but many studies have shown that the impact of iodine is less than 2% of calculated doses[73,74,75].

If DECT is available, the second approach is still possible with the use of MIX (virtual 120 kVp). The same uncertainties may be expected as with SECT 120 kVp with iodinated contrast. The dose uncertainties will be determined in chapter 4.

Nevertheless, material decomposition can be used to improve planning calculations. DECT can be used to virtually remove iodinated contrast from patient tissue. The resulting VNC series have been used for this purpose, and their calculation accuracy has been well established[73,74]. However, there is still a lack of empirical confirmation of dual-spiral DECT uncertainties.

Finally, DECT images can be used to decrease metal artifacts and in turn to delineate volumes in the presence of metal implants, improving calculation accuracy that high-density artifacts may distort. Although DECT reduces metal artifacts, this is not the only strategy to deal with them. IMAR algorithms have demonstrated better results without the need for two acquisitions at different kilovoltage settings.

1.2.8 Questions regarding dual-spiral DECT

Each of the different types of DECT must be studied in depth to understand their particular features and applications. Not all systems can be properly used for all DECT applications due to their acquisition characteristics. Limitations of dual-spiral systems originate in the temporal non-coherence due to the sequential scan acquisition. The 15 s time difference between scans has different consequences that affect series registration.

- Patient motion artifacts due to separate acquisitions: CT couch changes the direction of its movement between scans, stopping and accelerating in the head-to-toe direction.
- Internal organs motion: acquisition time is long enough to allow internal movements between scans such as swallowing or breathing. Those movements may result in registration errors that can change the relative CT numbers between scans (**Figure 32**).
- Differences in iodine uptake due to tissue diffusion and blood flow.

All three issues may affect the capability of DECT to decompose patient tissues in different materials and may affect iodine enhancement in the images. As the series are not taken at the same time, it is not possible to create VMI, MIX, and VNC images in the projection space of the CT. Thus, dual-spiral DECT can only reconstruct derived images in the image space when CT numbers have already been calculated by the filtered

backprojection software. This results in an overall increase in noise in all series, which adds to the uncertainty caused by the aforementioned artifacts.

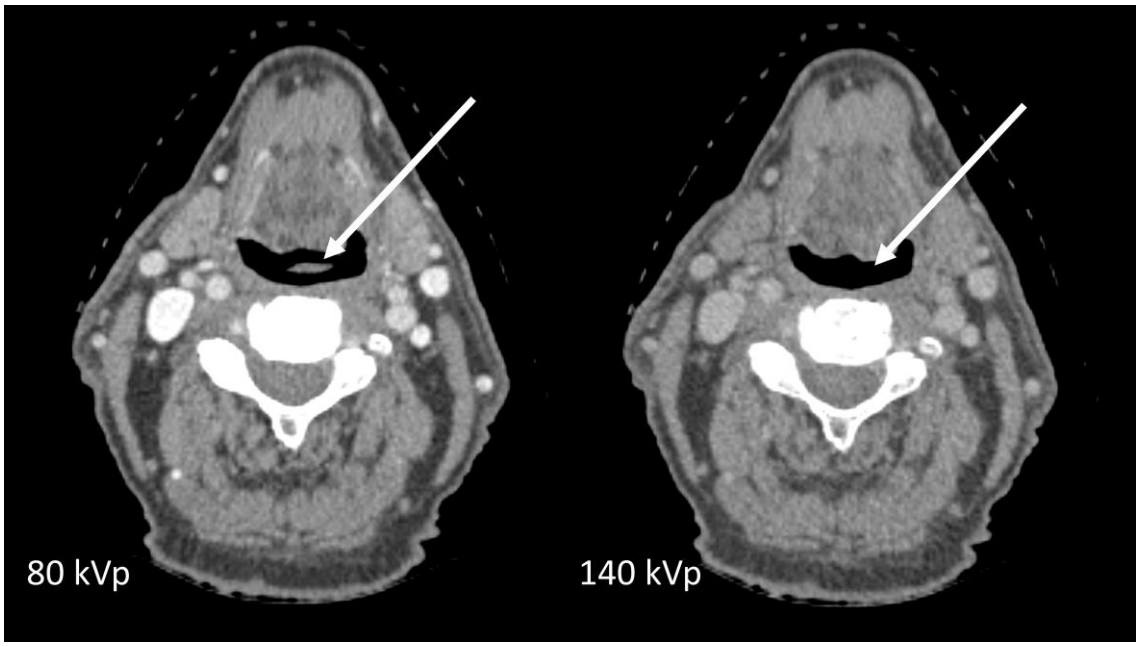

Figure 32. Organ displacement due to swallowing. In the same slice, the epiglottis is present in the 80 kVp image but not in the 140 kV image. Author's data.

VMI series are known to show higher iodine enhancement but also to be affected by increasing noise with decreasing energy[76,77,78]. One advantage of dual-spiral DECT is the possibility to separately tune the high- and low-kilovoltage acquisitions, which can partially compensate for the higher contribution of the low kilovoltage to the overall noise. Additionally, there are now second generation VMI algorithms such as Monoenergetic+ that improve the noise profile of VMI series. Although there are many studies about VMI and VNC characteristics of dual-source, twin beam, dual-layer and fast kV-switching systems, there is still a lack of information about dual-spiral DECT. It is necessary to know the extent to which VMIs from dual-spiral DECT are useful for improving delineation in RT treatments and whether they are equivalent to other systems or not.

Regarding VNC series, these are also affected by higher noise than the SECT 120 kVp images. Many studies have investigated the use and accuracy of VNC images in dose calculations for RT planning, with good outcomes[73,74,75]. However, there are still gaps in evidence about dual-spiral DECT VNC images because of concerns about the influence

of a changing iodine concentration in tissues and blood. So far, it remains unknown whether some injection conditions can reduce VNC uncertainties in dual-spiral DECT and if the size of the calculation matrix can partially compensate for the increased noise. Moreover, there are no studies about the overall uncertainties introduced by dual-spiral DECT VNC in dose calculations. Finally, the relative benefit of those images compared to calculations done on SECT series with injected iodinated contrast is unclear.

In summary, there is plenty of literature about the use of dual-energy CT in RT planning. It is well known that VMIs are useful for better tumor delineation and that VNC images are so accurate for calculations that they can substitute the need for real non-contrast images for planning. Those features have been well investigated in all DECT systems except dual-spiral. In light of the increasing adoption of dual-spiral DECT throughout the world due to its low cost and system simplicity, a deep study of VMI and VNC series and their use in radiotherapy is needed. This study is about dual-spiral DECT and its use in radiotherapy of the head and neck, where iodinated contrast is commonly used, and dual energy can play a crucial role.

1.3 Hypotheses and general objectives

1.3.1 Hypotheses

Like any new technology, dual-spiral DECT has to be compared to existing systems with regard to its characteristics and potential advantages. Therefore, we formulated the following hypotheses about dual-spiral DECT in radiotherapy of head and neck tumors.

1) The quality of VMIs meets international standards for use in CT imaging.
2) There is an optimal energy range for VMIs where quality and iodine enhancement are at a maximum.
3) VMIs are superior to single-energy 120 kVp and 80 kVp images in iodine enhancement.
4) Virtual monoenergetic images improve tumor delineation in RT treatments of the head and neck.
5) Virtual non-contrast images can be used to eliminate the need for a non-contrast CT acquisition in dose calculations for radiotherapy of the head and neck.

6) The condition of a 76 s time delay between the start of iodine injection and the start of CT scanning allows precise calculations of dose on VNC images.
7) Dual-spiral dual-energy CT is not inferior to other types of dual-energy CT.

1.3.2 Objectives

According to our hypotheses, the general objectives of this work are to assess the utility of dual-spiral DECT in delineation, planning, and dose calculations. Specific objectives are as follows.

1. Utility of dual-spiral DECT images in delineation of tumor and organs at risk.
   1.1. To determine the quality of VMIs based on standard CT parameters.
   1.2. To determine the optimal range of VMI energies to make the most of contrast enhancement and image quality.
   1.3. To quantify the overall improvement in tumor delineation using VMIs.
2. Utility of dual-spiral DECT in planning and dose calculations.
   2.1. To determine the acquisition conditions to prevent iodine concentration changes between the 80 kVp and 140 kVp scans.
   2.2. To determine calculation uncertainties introduced by VNC images in comparison to real non-contrast and contrast-enhanced images.
   2.3. To compare dose distributions calculated on single-energy scans to those calculated on VNC and MIX dual-energy scans.

1.4 Structure of the study

After the thorough introduction about Dual Energy and the questions still under discussion, we present the complete research to test our hypotheses, a comprehensive study of dual-spiral DECT. It was designed in three parts:

The first part (chapter 2) focuses on the quality of Virtual Monoenergetic Images derived from a dual-spiral scan. This part has two sections:

- The first is a phantom study that summarizes international standards and recommendations and applies them to VMIs. Based on the parameters employed, we establish an optimal range of use for those types of CT images.
- The second section is a study of 15 real patients where we determine the contrast-to-noise ratio in VMIs and compare it with the single-energy scans at two different kilovoltages: 120 kVp and 80 kVp.

Part 2 (chapter 3) of the study investigates the utility of VMIs for tumor delineation in Radiotherapy treatments of the head and neck. We first present a subjective analysis of oncologists' perception about those images, and then we deal with the problem of measuring interobserver variability in a cohort of 15 patients. In this part, we also propose a graphical method to compare interobserver variability.

Part 3 (chapter 4) of the study deals with the problem of iodinated contrast in dose calculations of RT plans. This part of the work includes 30 patients to whom we injected iodine in order to improve delineation. We present the dose calculations of four RT plans for each patient, calculated on non-contrast, alpha blended MIX series, and Virtual non-contrast images. We compare them and analyze the possibility of doing calculations on VNC images instead of doing an additional CT acquisition without injected iodine.

Finally, we present our final conclusions in chapter 5.

2. Quality of Virtual Monoenergetic Images

2. Quality of Virtual Monoenergetic Images

DECT in radiotherapy of the head and neck area is mainly used to improve visualization of tumors and organs at risk (OARs) through its superior enhancement of iodine contrast. It is assumed that virtual monoenergetic images (VMIs) are useful for that purpose.

As mentioned in section 1.2.6.2, numerous studies have been published about the medical applications of those images. However, there are gaps in the literature with regard to the performance of VMIs in terms of the commonly accepted quality parameters for CT imaging: uniformity, high- and low- contrast resolution, noise spectrum, and quantity and contrast enhancement. Moreover, there are no studies about those factors in dual-spiral DECT.

If VMIs were of insufficient quality, their use might be constrained to applications where their limitations were not critical. Thus, this study aims to determine:

1) whether VMI series are of acceptable quality,
2) if there is an energy interval where VMIs are superior to SECT images for visualizing the head and neck area with the clinical practice protocols used at Hospital del Mar; and
3) whether contrast enhancement is impaired at low energies because of noise.

The work presented here is a phantom study of the VMIs generated from the dual-spiral DECT of a Siemens Somatom Confidence RT Pro CT scanner and the software Syngo Via vB50, with the low noise algorithm Monoenergetic+. The main limitation is that the study only applies to similar systems, and the conclusions cannot be generalized to other types of dual-energy CT. Nevertheless, the main goal is to propose the application of a standard method based on accepted quality parameters to evaluate DECT images, independently of the system.

We also present a study of contrast enhancement in patients to evaluate the potential advantages of VMIs compared to SECT and MIX images.

2.1 Materials and methods

We compared image quality using the parameters mentioned in international guidelines ICRU report 87[79], International Atomic Energy Agency TECDOC19[80], and American Association of Physicists in Medicine (AAPM) TG-233[81]: image uniformity, high-contrast resolution, low-contrast resolution (LCR), and noise. We also added sensitivity to the iodinated contrast, as one of the main advantages of VMI resides in that measure.

Image uniformity was the only parameter compared to an absolute acceptance value, as there are standard values in the guidelines and in the manufacturer's documentation. For the rest of the parameters, values were computed and compared to those of 120 kVp SECT with an eye toward identifying possible improvements in image quality. We used the manufacturer's tolerance where available. Finally, as low-kilovoltage SECT images are known to have an increased contrast-to-noise ratio (CNR) when iodine contrast is injected into the patient, we compared the VMI series to 80 kVp to determine if there is a range of energies where DECT VMIs are superior to SECT in our system.

The image series were acquired using Siemens Somatom Confidence RT Plus CT equipment, and the protocols analyzed were those used in clinical practice at Hospital del Mar for head and neck tumors. For the 120 kVp series, these were: field of view 50 cm, slice thickness 2 mm, pitch 1.0, and BR38 filter. For the 80 kVp and 140 kVp DECT series, pitch was set to 0.8 and 1.2, respectively. We used the series at 120 kVp as a reference, as this is the standard energy used for simulating RT treatments. The series at 80 kVp was chosen because it is recommended by the manufacturer as the lowest energy with acceptable quality, although the Somatom Confidence system can also acquire series at 70 kVp. We compared VMI series at 40 keV to 60 keV versus SECT series at 80 kVp and 120 kVp. **Table 3** presents the set of images used in the study. Each experiment was repeated five times to measure variations.

All series were acquired for the Catphan 604 quality control phantom (**Figure 33**). We applied the dose constancy $CTDI_W$ = 17 mGy to all the series because this is the dose administered to the real patients in our reference studies at SECT 120 kVp, so we could control for the dose effects on image quality[82].

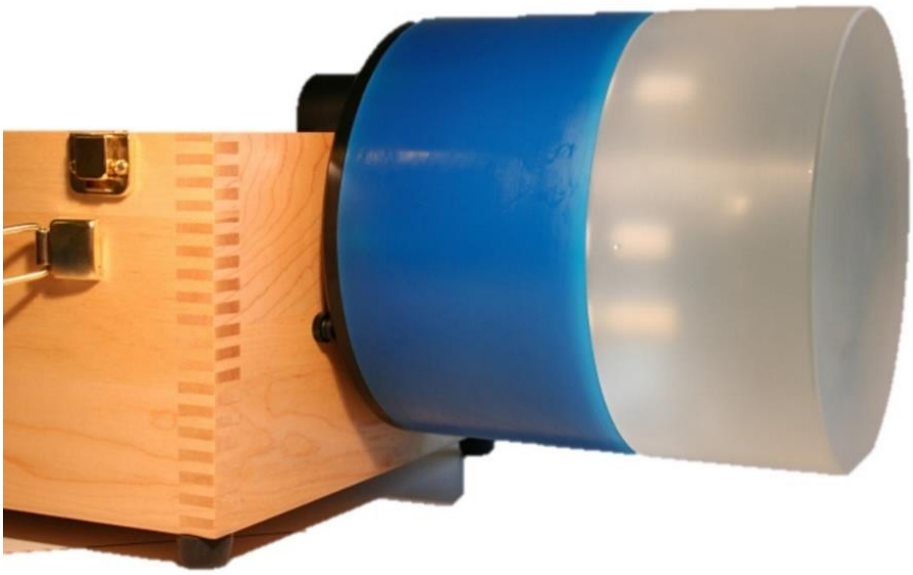

Figure 33. Image of Catphan 604. Courtesy of The Phantom Laboratory Inc.

The VMI series were obtained using the Siemens Syngo Via software v.50 with the algorithm Monoenergetic+ for noise reduction at low energies, based on two sequential acquisitions series at 80 kVp and 140 kVp. Monoenergetic images at energy *E* are calculated as a linear combination of the acquisitions at high and low energy, according to the formula developed by Yu et al.[76]:

$$HU_x(E) = \omega_x\,(E) \cdot HU_{x,low} + (1 - \omega_x(E)) \cdot HU_{x,high}$$

where x is the specific pixel; $HU_{x,low}$ and $HU_{x,high}$, the Hounsfield units of the pixel in the low- and high-energy series, respectively; and ω_x, the weighting factor, which can be calculated from the attenuation coefficients of any two known materials, in this case water and iodine, μ_1 and μ_2, so that:

$$\omega(E) = \frac{\mu_1(E) \cdot \mu_2^H - \mu_2(E) \cdot \mu_1^H}{\mu_1^L \cdot \mu_2^H - \mu_1^H \cdot \mu_2^L} \cdot \frac{\mu_2^L}{\mu_2(E)}$$

Table 3. Number of series and total images used for each test

		CT test characteristics				
		140 kVp DECT	***80 kVp DECT***	***120 kVp SECT***	***80 kVp SECT***	***40-60 keV VMI***
Parameters		***A****	***A***	***A***	***A***	***C***
Uniformity	Series	1	1	1	1	5
	Images	17	17	17	17	85
High-contrast resolution	Series	3	3	3	3	15
	Images	6	6	6	6	18
Low-contrast resolution	Series	1	1	1	1	5
	Images	7	7	7	7	35
Noise	Series	2	2	2	2	10
	Images	4	4	4	4	20
Contrast sensitivity	Series	15	15	15	15	75
	Images	450	450	450	450	33750

DECT: dual-energy CT; SECT: single-energy CT.

(*) A=Acquired, C=Calculated

Note: For low-contrast resolution and noise, all images had to be converted to text by means of the open-source program Image J, in order to handle them with Microsoft Excel.

2.1.1 Image uniformity

The CT numbers in the images of a standard phantom, in our case the CTP486 module of the Catphan, may be higher at the center than in the periphery (capping) or vice versa (cupping). We measured this difference, creating four regions of interest (ROIs) in the periphery, situated at 0°, 90°, 180°, and 270°, plus one at the center, all with a radius of 1 cm (approximately 1% of the surface of the phantom section), and we looked for differences among the 20 slices acquired in the module (**Figure 34a**).

The criterion for standard acceptance is $|HU_{periph}-HU_{center}| < 7$ HU for the mean CT numbers of any of the ROIs, although a difference of less than 5 HU, or another value specified by the manufacturer (in this case 4 HU) is recommended. In this study, our acceptability criterion was 4 HU, allowing up to 7 HU as a minor deficiency.

2.1.2 High-contrast resolution

There are different methods for comparing high-contrast resolution through the determination of the modulation transfer function (MTF)[83-86]. In this study, we used two methods based on the calculation of the discrete Fourier transform (DFT) function: 1) the MTF calculation based on the point spread function (PSF) of a pointed bead, which the manufacturer uses as the standard[86] (**Fig. 34b**), and 2) the slanted edge method[84,85], as described in the ISO standard 12233.

a) MTF calculated with a point bead

The image of a point object in a perfect system should be a point. However, real imaging systems have physical limitations that produce signal spreading around the point. In a CT scanner, those limitations come from the acquisition and digitalization system of the scanner itself, and from the selected reconstruction algorithm or filtered back projection. The MTF measures that point spreading, which is one of the best methods to assess system performance in terms of high contrast resolution.

The Catphan phantom has a point bead with a diameter of 0.18 mm, nearly 5 times smaller than the pixel size used in this study (**Figure 34b**). Ideally, the point bead should occupy only one pixel in the image, but in practice it spreads around (**Figure 35**). The result of this spreading resembles a normal distribution, which is fitted by a polynomial fit with 6

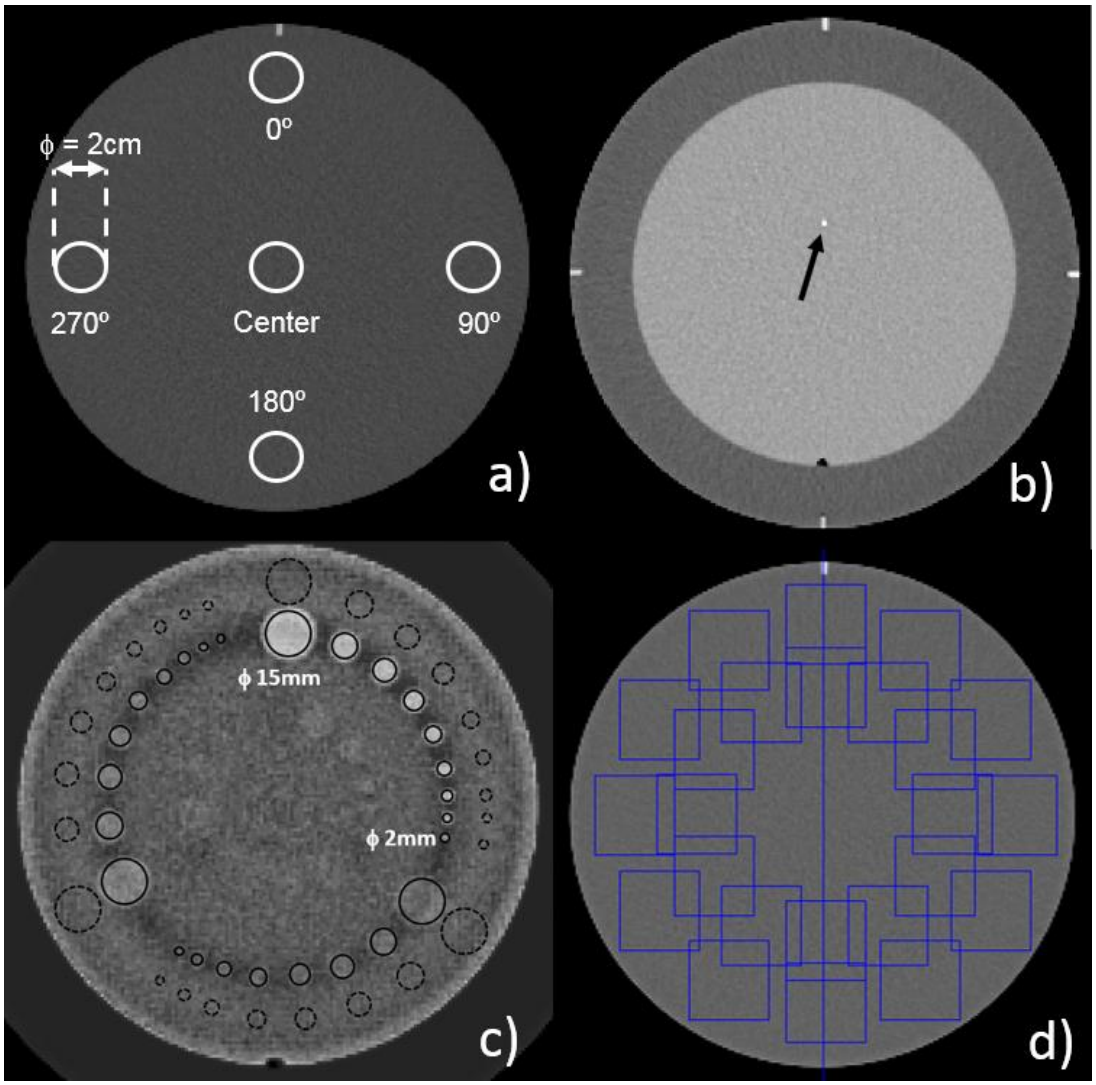

Figure 34. Regions of interest (ROIs) designed for quality control in the Catphan phantom a) ROIs for uniformity calculations. b) Point bead for modulation transfer function (MTF) calculation. The arrow points to the tungsten carbide bead, which has a diameter of 0.28 mm. Pixel size is 0.97 mm. c) ROIs for low-contrast resolution at 120 kV, low-noise image averaged over 17 slices. d) ROIs for noise power spectrum (NPS) calculations. Squares are all 32 × 32 pixels wide.

degrees of freedom. The resulting polynomial is known as the point spread function (PSF).

As point spreading arises in the X and Y directions, the line spread function (LSF) is obtained by averaging the PSF in X and Y directions. Finally, MTF can be calculated as the DFT of the LSF:

$$\mathrm{MTF} = \mathrm{DFT}[\mathrm{LSF}]$$

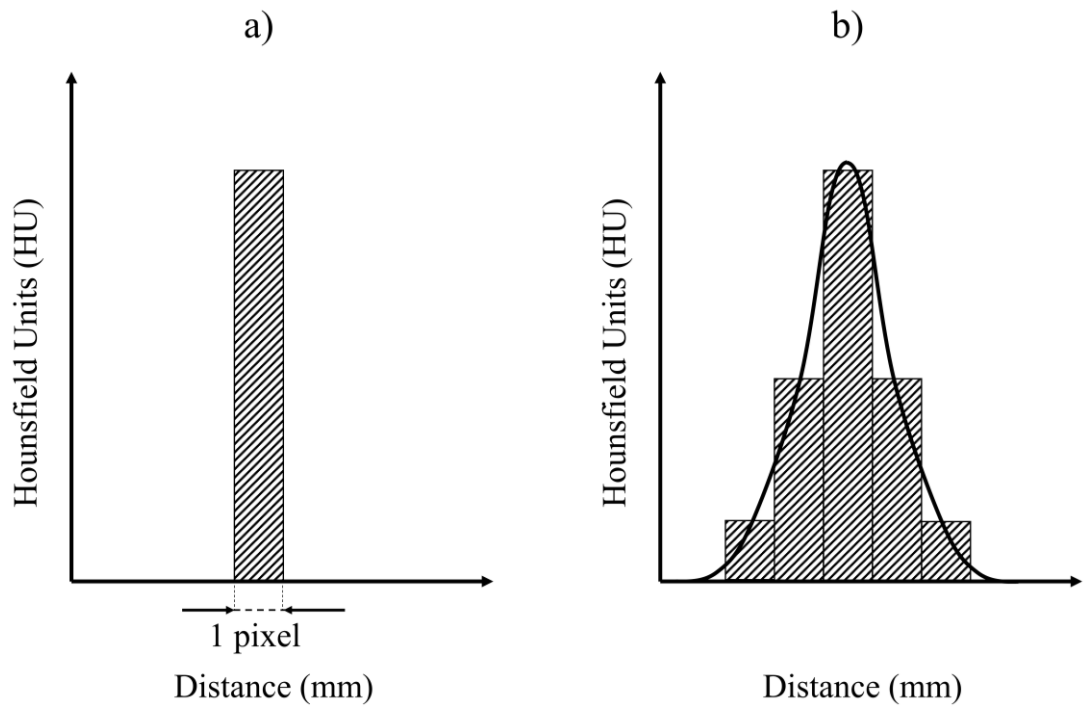

Figure 35. Ideal point spread function (PSF). a) Ideal system where the subpixel bead occupies only one pixel in the image. b) Real system with point spreading. The solid curve is obtained by polynomial fit (6 degrees of freedom) and represents the PSF.

We compared the different series using each method independently and observed the variations produced between them. We calculated the different MTFs using IQWorks open-source software. The MTF, as assessed by the PSF method, was used as the reference because the manufacturer tolerances referred to this method. The values compared were the MTF_{50} (frequency at which the MTF is at 50% of its maximum value) and MTF_{10}. The reference values for MTF_{50} and MTF_{10} supplied by the manufacturer are 3.14 ± 0.3 lp/mm and 5.81 ± 0.58 lp/mm, respectively, which correspond to a 10% tolerance.

b) MTF calculated with the slanted edge method

To calculate the MTF using the slanted edge method, we used a cubic phantom made of solid water. The contrast relationship between edges and background was 1000:1, and the inclination of edges was 5º with respect to the horizontal and vertical directions. We analyzed the four edges. As IQWorks had problems calculating the left and bottom edges, we first analyzed the top and right, and then rotated the image (not the phantom in the acquisition) 180º for the other two (**Figure 36**).

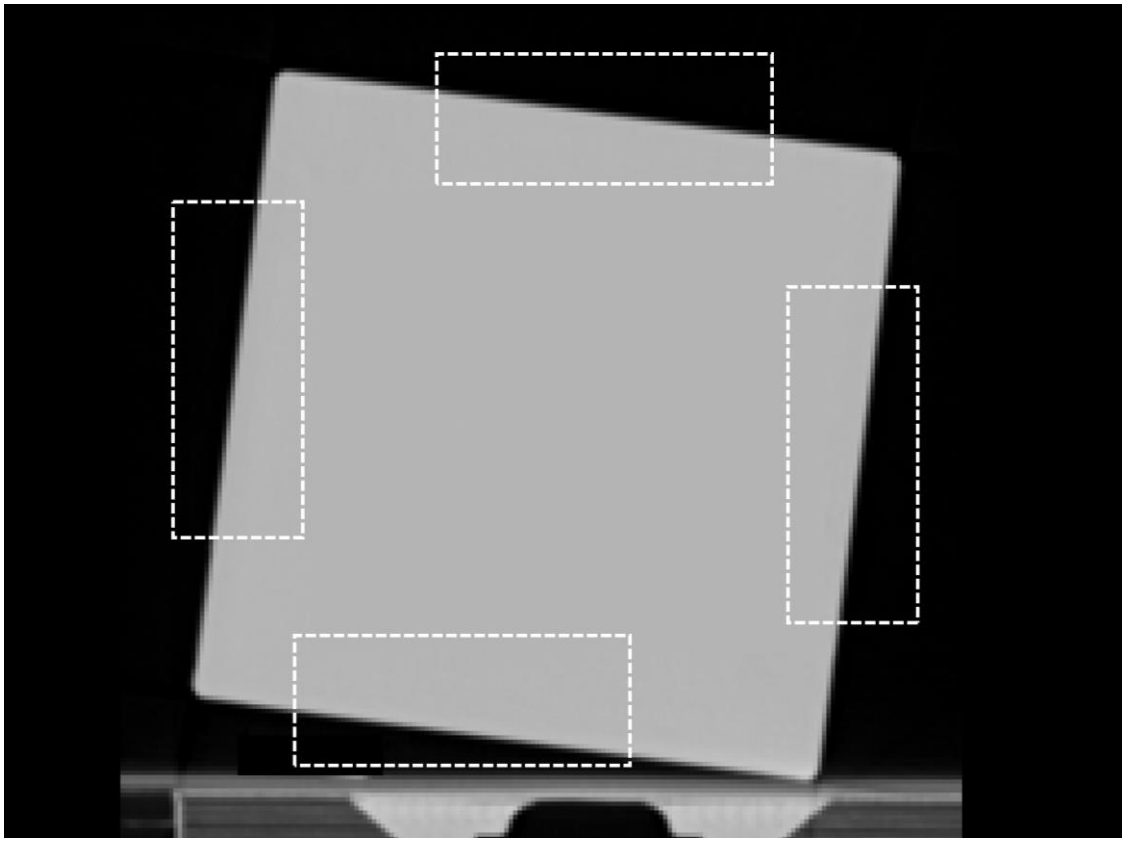

Figure 36. Scan of the cubic phantom for the modulation transfer function (MTF) slanted edge method. The four rectangles correspond to the averaged edges.

2.1.3 Low-contrast resolution

For the parametrization of the LCR, we used the images from the CTP515 module of the Catphan phantom, which consists of nine cylindrical targets with diameters of 2 mm to 15 mm, and three contrast levels: 0.3%, 0.5%, and 1%. Although the classical method of evaluation consists of visual observation of the cylinders, different quantitative methods have been described for observer-independent determination of the LCR[87,88]. We evaluated LCR through the statistical validation of the difference in mean CT number values between the inserts and the local background. We also calculated the CNR for each cylinder and contrast level in order to observe the numerical relationship between the CNR and statistical significance of our method.

As the LCR is greatly affected by the noise of the images, and therefore the dose[89], we acquired a series at 120 kVp with the maximum milliamperage that the CT permitted (600 mA), and we calculated the average image from 17 images of the CTP515 to obtain the clearest possible vision of the cylindrical positions and thus create the corresponding ROIs. This image was used to identify all the inserts in the phantom, their positions, and boundaries. All other scans were

acquired in the same session with no lateral or vertical movement of the phantom to ensure that all the inserts remained in the same positions in all series.

To apply the statistical method, we created 27 ROIs on the inserts in the low-noise image, and for each, we created an additional ROI, with the same dimensions but farther away in a radial direction. This ROI served to measure local noise (**Figure 34c**). We did not use concentric ROIs, as proposed in the document TG-233, for two reasons: first, in most cases, the ROI with the largest diameter overlapped with the next insert, and second, the presence of an artifact between inserts (dark grey in **Figure 37**) changed the CT number distribution.

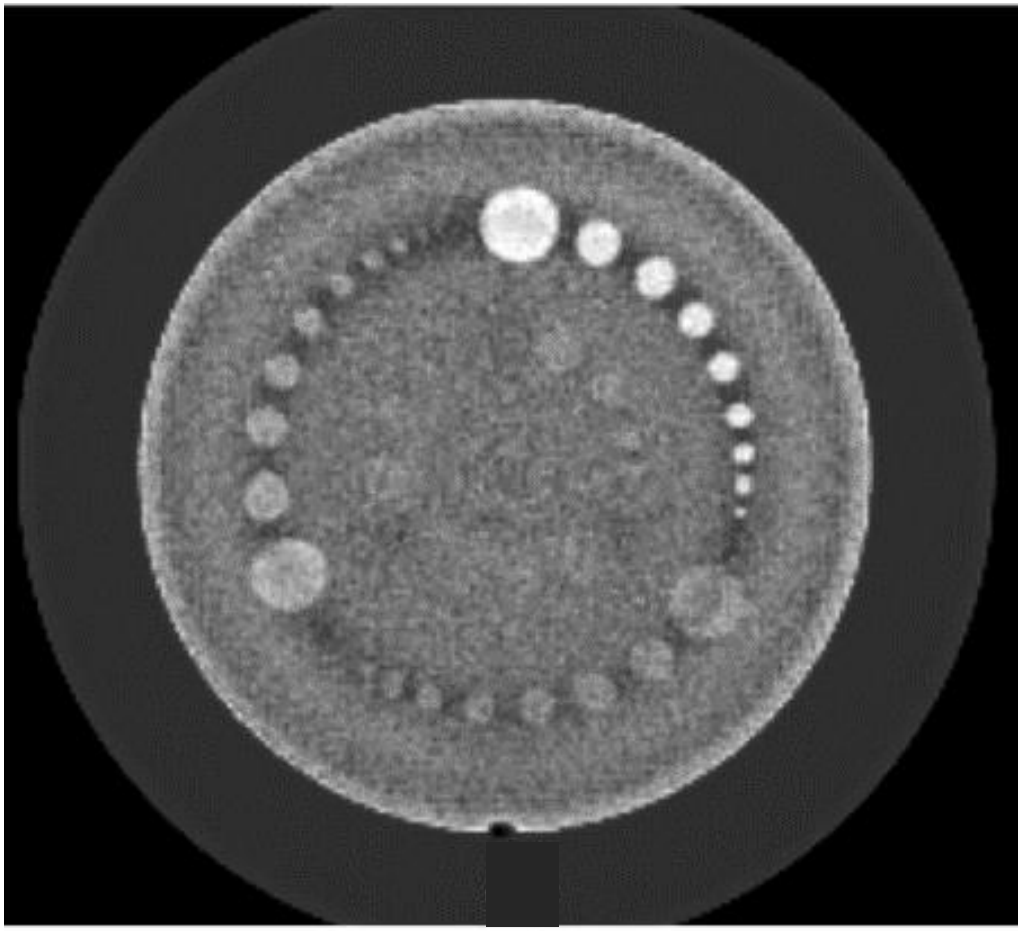

Figure 37. Reference image at 120 kVp SECT, where all 27 rods can be identified and a dark artifact between cylinders is apparent.

To reduce the effect of noise on the series (**Figure 38**), we used the seven central images for each, ensuring that the entire CT beam stayed within the LCR module, thus avoiding undesired artifact effects due to scatter from other zones with different density distributions. This decision was also useful to provide a statistic with sufficient points on

the smallest ROIs. Since the 2 mm insert is represented by only 5 pixels in one image, using 7 images for statistics increased the number of points to 35 for the smallest insert.

We copied the three sets of ROIs onto each of the series, comparing each ROI with its counterpart of the same dimensions for noise, by means of a one-tailed student's t test in order to assess the statistical significance of the difference in mean CT number values. All calculations were done using Microsoft Excel Visual Basic macros.

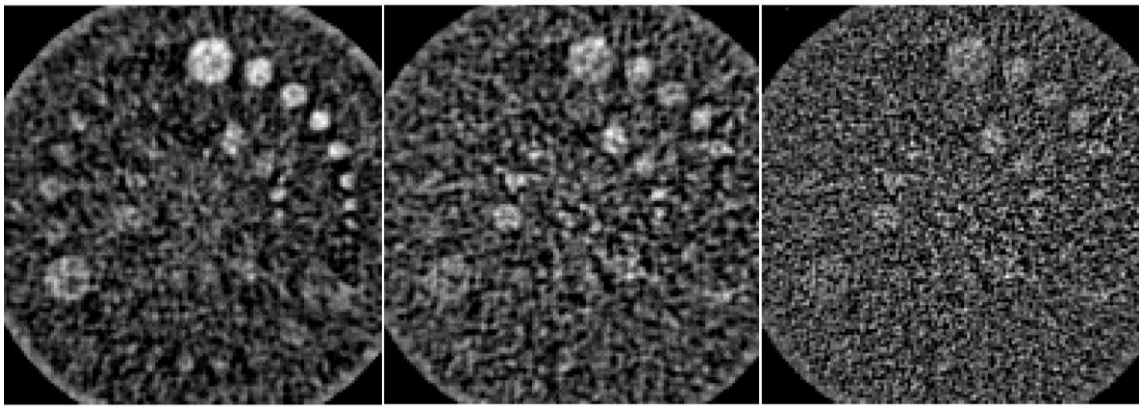

Figure 38. Example of noise influence in low-contrast resolution. a) 45 keV with 7 slices averaging. b) Same with 2 slices. c) No averaging. It is clear that more rods are visible in a) than in b) and c).

We considered the first mathematically non-visible ROI at each contrast level to be the first that presented a non-significant difference ($p > 0.05$) between the distribution of the cylinder versus that of the noise, in diameters of descending order. The LCR was established as the diameter immediately above it.

For model validation, we checked the two extreme situations. First, we applied the method to a uniform phantom with no rods, and then we applied it to the low-noise 120 kVp series, where all the rods are visible. In the first case, all ROIs showed non-significant differences, indicating there were no rods. In the second, all ROIs showed statistically significant differences, and all the rods were observed.

2.1.4 Noise

Noise is one of the main concerns about VMIs[90], warranting an in-depth study on it. The simplicity of the standard deviation (SD) and the existence of a manufacturer's reference at 120 kVp provides a straightforward way to quantify noise. However, this method fails to provide important information about noise texture when reconstruction algorithms are

involved, as is the case with VMIs. In order to acquire this information, the complete calculation of the noise power spectrum (NPS) was performed, as recommended by the standards AAPM TG-233 and ICRU report 87. We used peak frequency as the texture indicator and area under the curve as the total noise parameter for comparison.

Since the manufacturer uses the SD of noise as a reference, we studied noise using both methods: 1) assessing the SD of a ROI, and 2) calculating the NPS according to international guidelines[91].

a) Standard deviation of a region of interest

The manufacturer specifies that the SD of noise should be measured using an ROI of 8 cm in diameter (40% of the diameter of the phantom), in a cylindrical water phantom of 20 cm in diameter. For each series, we determined the mean SD in the eight central slices of the standard phantom module. Our reference was the mean SD of the 120 kVp series.

According to the CFR-21[92], the value of noise S_n should be calculated according to the formula:

$$S_n = \frac{100 \cdot CS \cdot s}{\mu_w}$$

Where CS is the contrast scale, s the SD of the CT numbers in the ROI, and μ_w the linear coefficient of the air attenuation.

The contrast scale is calculated as:

$$CS = \frac{\mu_x - \mu_w}{CT_x - CT_w}$$

where CT_x and CT_w are the CT numbers (in HU) of any material x and of water, respectively, and μ_x and μ_w their linear attenuation coefficients. Considering that the calibration curve of the equipment is rectilinear for densities between air and water, that $CT_{air} = -1000$ and $CT_w = 0$, and that $\mu_{air} << \mu_w$, the previous expression is simplified to:

$$S_n \approx 0.1 \cdot s$$

b) Calculation of noise power spectrum

To obtain the 2D curves of the NPS for each energy, we first subtracted the images from a single slice in two consecutive acquisitions in order to eliminate the low-frequency

component stemming from the cupping phenomenon, using the method described by Yang et al.[93]

Thus, the formula used for calculating the NPS in a set of *N* ROIs is as follows:

$$\mathrm{NPS}(f_x, f_y) = \frac{1}{N} \frac{\sum_{i=1}^{N} |\mathrm{DFT}_{2D}[K_i(x,y) - \overline{K}_i]|^2}{2} \frac{\Delta_x \Delta_y}{N_x N_y}$$

where $\overline{K}_i$ is the mean CT number value in the ROI K_i.

We calculated the values of f_x and f_y using a custom-developed Visual Basic macro in Microsoft Excel, which determined the NPS of 22 squared ROIs of 32×32 pixels, distributed as shown in **Figure 34d**. We obtained the final NPS for each series by averaging the NPS of all ROIs in a single image. As the NPS is a 2D function with radial symmetry (**Fig. 39**), we used the radial frequency for comparison, calculated using the equation:

$$f_r = \sqrt{f_x^2 + f_y^2}$$

The total noise variance s^2 was evaluated as the surface under the curve NPS(f_r):

$$\sigma^2 = \iint \mathrm{NPS}(f_x, f_y) df_x df_y$$

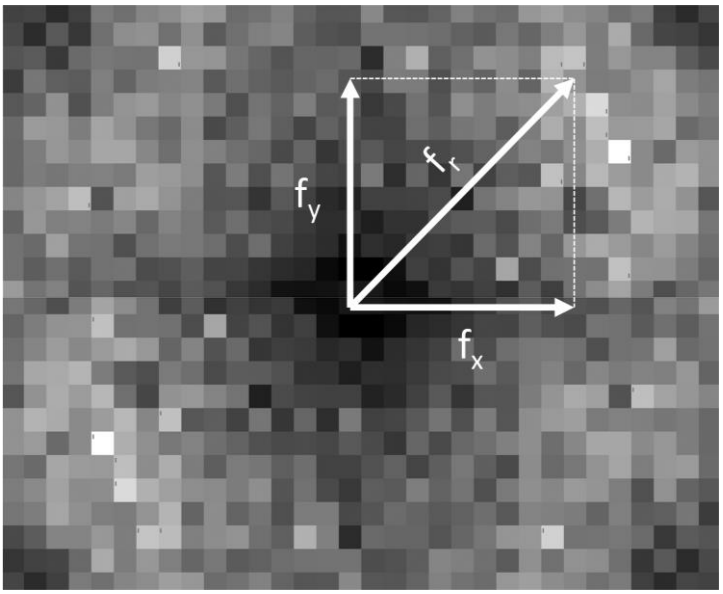

Figure 39. Noise power spectrum calculated with regions of interest of 32 × 32 pixels. NPS is radially symmetric, with a toroidal shape. Calculated by means of an Excel macro based on author's data.

2.1.5 Contrast enhancement

Although accepted standards hold that the accuracy of CT numbers is a critical parameter for image acceptance, we propose contrast enhancement (CE) by means of the CNR quantification for VMI evaluation, for three reasons: 1) CT numbers change as imaging energy changes, and it is not possible to compare CT numbers to those at 120 kVp; 2) the main advantage of VMIs is their higher CE, which increases at lower energies[70]; and 3) noise affects the CNR of VMIs[78] and may reduce differences between energies.

To assess the CE of the VMIs and their values relative to 120 kVp, we measured the CT numbers for a cylindrical water phantom (diameter 8.5 cm, length 13 cm), injecting Optiray Ultraject iodinated contrast into the concentration interval from 0 mg I/l to 4500 mg I/l. Since we observed 1 HU of increment relative to pure water at a concentration of 30 mgI/l in the 120 kVp images, we chose that value as the minimum iodine concentration for the study, considering the system was unable to detect lower concentrations.

We represented the dependence of the difference in CT numbers between a cylindrical ROI with a 6 cm diameter and a 6 cm length centered in the phantom, on the one hand, and the CT number value of distilled water for each energy on the other. We considered the CE value in $HU \cdot l \cdot mg^{-1}$ to be the slope of the regression line for each of the series. We chose a large ROI to avoid small volume effects on the CT numbers, thus obtaining the intrinsic iodine sensitivity for all the series.

After checking CE in the phantom, we proceeded to test the extent to which that enhancement was present in 15 real patients. The parameter to compare was CNR, defined as follows:

$$\mathrm{CNR} = \frac{\mathrm{HU\ blood} - \mathrm{HU\ muscle}}{\mathrm{SDref}}$$

SD_{ref} is the standard deviation of CT numbers in a reference material. Usually, air is used as a reference in CT images because of its homogeneity. For air, the SD of CT numbers corresponds only to the random noise due to the acquisition system and the filtered back projection (FBP) algorithm. SD_{air} is exactly the same for all the VMIs, because all series are derived from the same set of images at low and high kilovoltage, so the random variations in CT numbers of air are fixed between VMI energies. Thus, using SD_{air} as

reference equals noise for all VMI energies. This does not correspond to the real situation in patients because in VMIs, noise increases as energy decreases. To overcome this limitation, we used muscle as reference material for noise. With this assumption, the CNR expression becomes:

$$\mathrm{CNR} = \frac{\mathrm{HU\ blood} - \mathrm{HU\ muscle}}{\mathrm{SD\ muscle}}$$

The CT numbers for blood (HU blood) were calculated as the mean in the jugular vein and the carotid artery on both sides of the patients. The CT numbers of muscle (HU muscle) were considered the mean between the sternocleidomastoids and the trapezius (**Figure 40**).

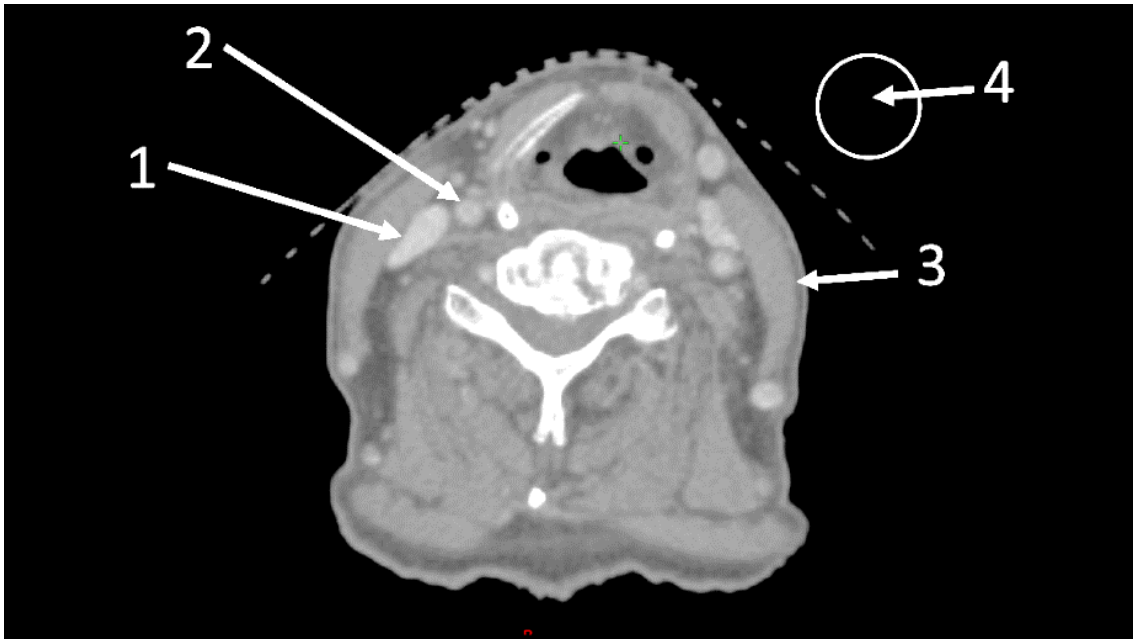

Figure 40. Location of organs for the determination of contrast-to-noise ratio. 1) Jugular vein, 2) carotid artery, 3) sternocleidomastoid, 4) air ROI.

2.2 Results

2.2.1 Image uniformity

Decreasing VMI energy resulted in decreasing uniformity (**Table 4**). The best uniformity was found in the reference series of SECT 120 kVp, and the maximum deviation was observed at 40 keV. At this energy, the lack of uniformity reached a maximum value of

5 HU. However, this result was observed in only one slice of the measured set of 20. In 6 of the 20 slices (30%), variations in CT numbers were between 4 HU and 5 HU, still within the tolerance permitted by international standards but over the manufacturer's recommended maximum 4 HU. Nevertheless, the mean value at 40 keV did not reach that value.

Table 4. Summary of results

Quality parameters	**Energy**						
	120 kVp	**80 kVp**	**60 keV**	**55 keV**	**50 keV**	**45 keV**	**40 keV**
Uniformity	HU						
Maximum difference	1.6	3	2.1	2.5	3.1	3.9	5.1
Average difference	1	1.9	1.4	1.8	2.2	2.8	3.5
High contrast resolution	lp/mm						
MTF_{50} point bead	0.29	0.3	0.29	0.31	0.3	0.3	0.3
MTF_{50} slanted edge	0.32	0.3	0.32	0.31	0.31	0.31	0.3
MTF_{10} point bead	0.51	0.51	0.5	0.52	0.51	0.51	0.51
MTF_{10} slanted edge	0.55	0.53	0.54	0.57	0.56	0.56	0.56
Low contrast resolution	Minimum ϕ (mm)						
Contrast 1%	3	3	2	2	2	2	2
Contrast 0.5%	4	5	3	4	4	4	4
Contrast 0.3%	7	8	9	7	7	8	8
Noise	HU						
S_n SD model	0.709	0.715	0.831	0.763	0.872	1.014	1.195
σ Area NPS curve	3.12	5.08	5.39	6.05	6.92	8.04	34.97
Contrast enhancement							
HU·l/mg	0.027	0.042	0.038	0.046	0.055	0.068	0.084

Over 40 keV, none of the series exceeded the manufacturer's reference value in any of the images. Moreover, when comparing the low-energy SECT series at 80 kVp to VMI, they presented similar uniformity to that at 50 keV, and worse than those at 55 keV and 60 keV.

2.2.2 High-contrast resolution

For the reference series, 120 kVp SECT, the values obtained for MTF50 and MTF10 were 0.29 lp/mm and 0.51 lp/mm, respectively, for the point bead model, and 0.32 lp/mm and 0.55 lp/mm, respectively, for the slanted edge model. All values fell within the tolerance limits established by the manufacturer (**Table 4**).

On analyzing the series, the maximum differences in MTF in comparison to the 120 kVp series for both models have a value of 0.02 lp/mm, analyzed separately, and they also remain within the manufacturer's accepted 10% tolerance limit (**Figure 41a**, **Table 4**). The lowest uniformity and the highest noise are at 40 keV. High- and low-contrast resolutions are similar between the series, and contrast enhancement is higher for VMI series for energies up to 55 keV.

Differences between models were under 10% in all cases. Moreover, on comparing the results between them, the slanted edge model provided somewhat higher MTF values for the two parameters studied. In the case of MTF50, the maximum difference was 0.03 lp/mm for the series at 120 kVp, and for MTF10 it was 0.05 lp/mm for the series at 40 keV (**Figure 41b**).

2.2.3 Low-contrast resolution

We started by applying the proposed statistical method to a uniform phantom and to the low-noise 120 kVp series to validate the extreme values (no ROI visible vs all visible). All rods were visible in the low-noise image, so we delineated the corresponding ROIs to apply the method (**Fig. 42**). As expected, on the uniform phantom, all ROIs showed non-significant ($p > 0.05$) differences in CT numbers with the background. Nevertheless, in the low-noise series, all the ROIs showed significant differences with respect to the background, at any diameter or contrast level.

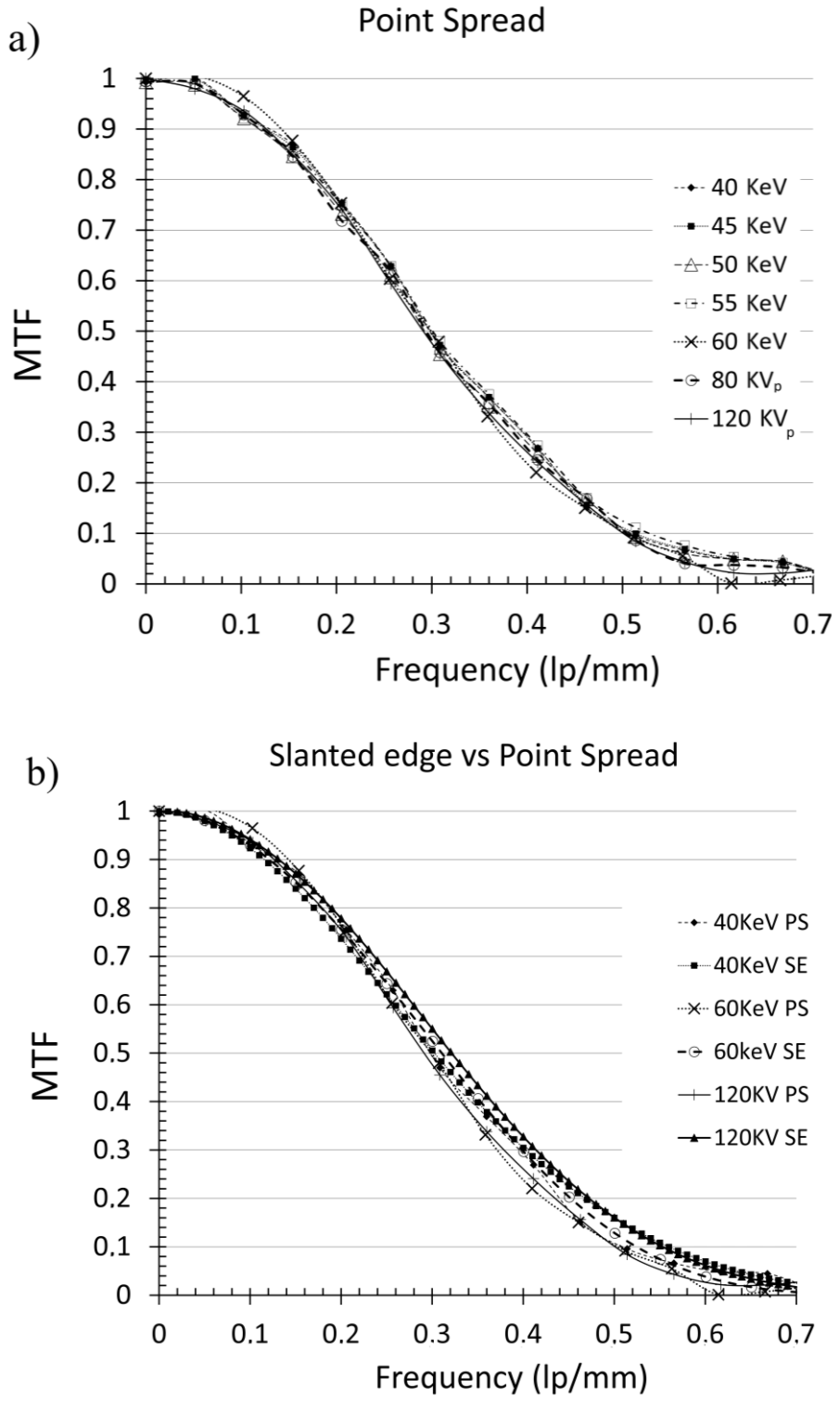

Figure 41. Calculated modulation transfer function (MTF) with two models. a) Modulation transfer function (MTF) calculated from the point spread function of a point bead for all energies. There are no evaluable differences between energies. b) Comparison of both models for the lowest VMI at 40 keV, the highest at 60 keV and the reference at 120 kVp. PS = point spread, SE = slanted edge. Only small differences can be observed between models for a particular energy.

For the cylinders at a contrast level of 1%, the VMIs presented better LCR than the reference 120 kVp (**Table 5**). Moreover, for the 2 mm ROIs, no statistical difference was seen between the series at 80 kVp versus 120 kVp. However, the 2 mm rod may be the most affected by noise because of the low number of statistical points, 4 per slice, so we did not consider this difference as remarkable.

For the 0.5% contrast, we likewise did not observe any appreciable differences between series; all of them had a resolution of 4 mm, although in the 80 kVp SECT the last observable cylinder was 5 mm, while for 60 keV VMI it was 3 mm.

For the 0.3% contrast, the 40 keV and 45 keV series showed a larger loss of LCR, probably due to greater residual noise than at other energies, while at 120 kVp, 50 keV, and 55 keV, the resolution was better.

Halting the averaging of the 7 images in each series resulted in an important loss of resolution. For the contrast levels of 1% and 0.3%, the least affected series were the VMI ones, which did not lose definition.

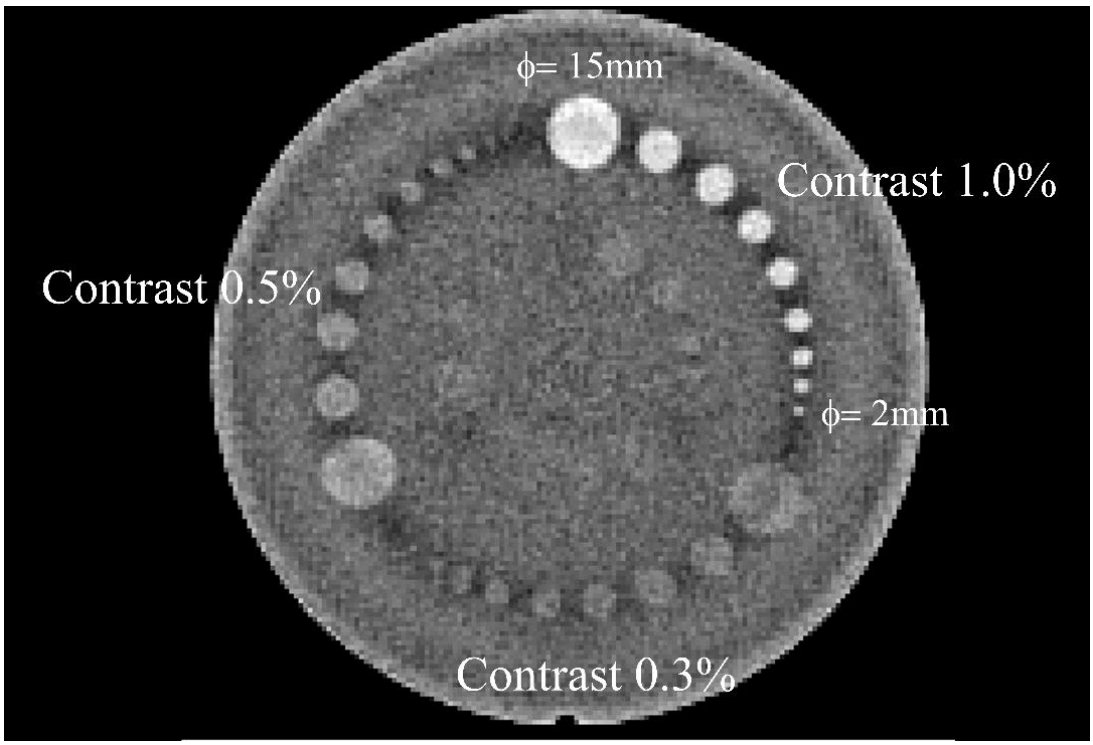

Figure 42. Low noise image at 120 kVp. All 9 rods from the three contrast levels are visible, defining the ROIs used by the statistical method described in the text.

2.2.4 Noise

According to the literature, low VMI energies result in an increase in noise. Our results confirmed that, because the analysis of the SD proposed by the manufacturer showed an increase in value with a reduction in series energy (**Table 4**). The maximum noise value was observed in the series at 40 keV, with nearly 70% more noise than that at 120 kVp. Moreover, the value of the series at 55 keV was quite similar to that at 80 kVp.

On analyzing the non-normalized NPS curves (**Figure 43**), a large increase in noise was clearly apparent for the low-energy VMI series, which is consistent with the SD model. **Table 5** presents the areas under the curves, with important differences between them. As with the previous method, reducing energy increases the area under the curve, and the NPS curve at 60 keV is very similar to that of the SECT image at 80 kVp. We can conclude, then, and in agreement with previous studies, that VMIs present high levels of noise that increase as energy decreases.

The spectral distribution of the normalized curves at the maximum frequency at each energy level is the same for all the VMI series but presents some differences compared to the SECT images: VMIs present a component with a higher 0 frequency, which is related to worse uniformity due to the capping or cupping effect. This result is in line with the observed decrease in uniformity at low energies. Moreover, SECT series have lower noise at high frequencies, which can be related to a smoother appearance of images. Nevertheless, all differences are small, and we consider that the texture of the noise is similar across the whole set of the series.

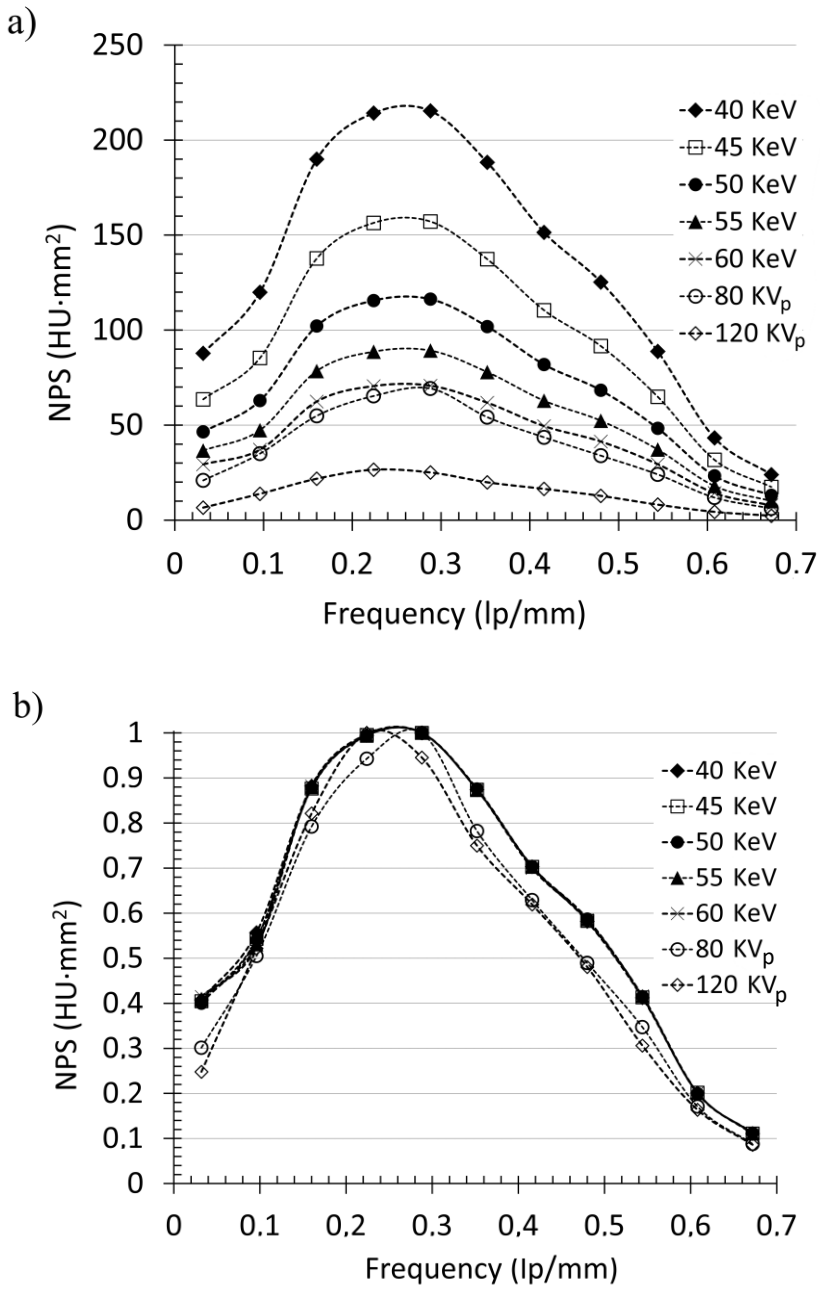

Figure 43. Noise power spectrum curves. a) Not normalized. Noise increases dramatically as energy decreases for the VMI series. b) Normalized curves for frequency domain and texture comparison show only small differences between SECT and DECT images. All the VMI series are equivalent.

2.2.5 Contrast enhancement

All series showed perfect linearity along the studied range of iodine concentrations, even at concentrations as low as 30 mg I/l. **Figure 44** shows the detail of the first 300 mg I/l

and how a reduction in energy in the VMI series increases the contrast enhancement. This feature is what makes VMI a useful tool for delineating target volumes.

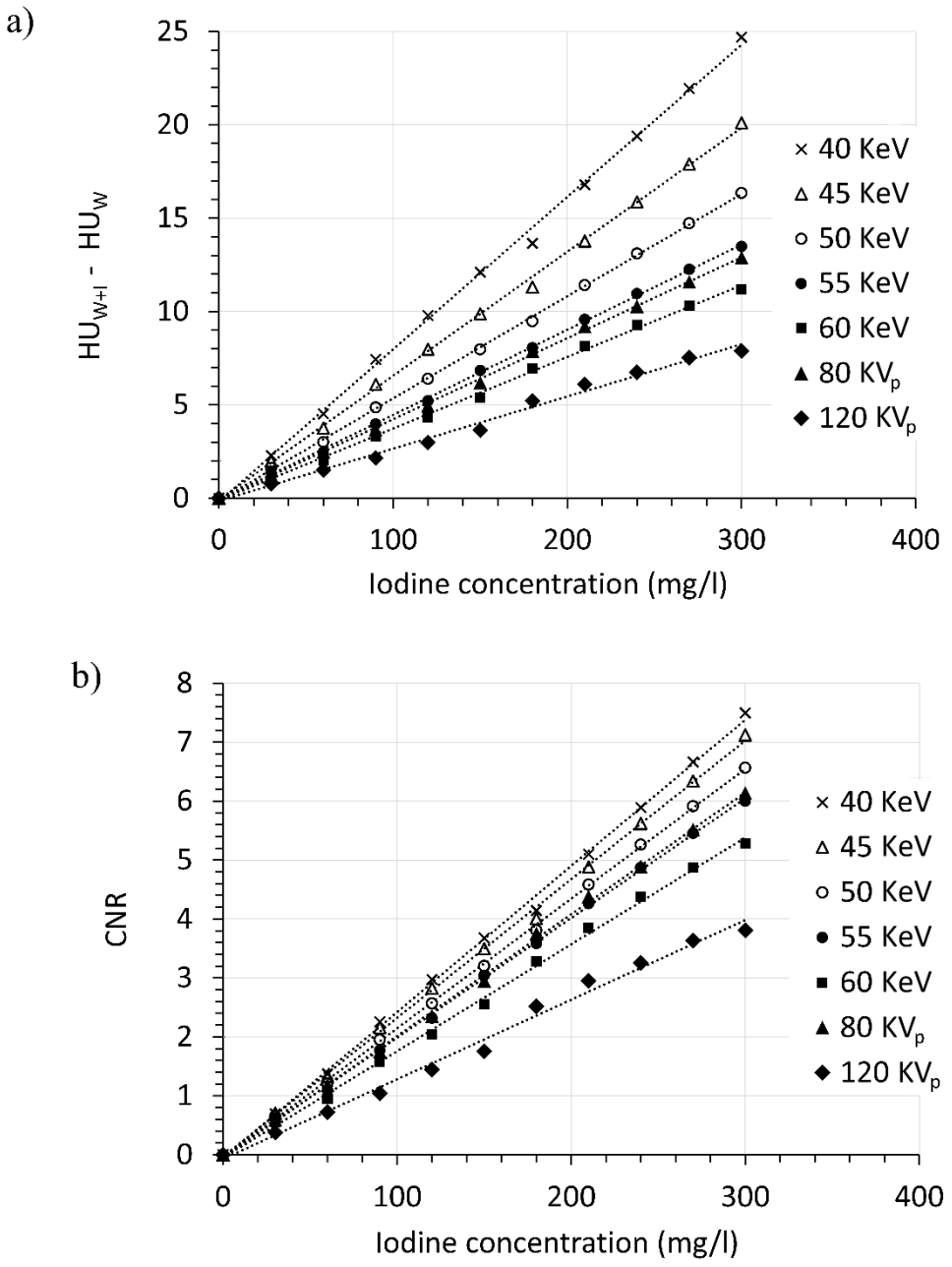

Figure 44. Differences in CT numbers of distilled water and iodinated solution. a) Differences in CT numbers of distilled water (HU_W) and iodinated solution (HU_{W+I}) related to iodine concentration for all energies at very low concentrations. Contrast enhancement is higher at 80 kVp than at 60 keV but similar to 55 keV. b) Representation of contrast-to-noise ratio (CNR) at the same concentrations. 80 kVp shows a higher CNR than 55 keV.

The series with energies at or below 55 keV showed a higher increase in CT numbers than the SECT series at 80 kVp and 120 kVp (**Figure 44a**, **Table 4**). The series at 60 keV was lower than that at 80 kVp, so the upper limit of energy in VMI series should be under 60 keV to obtain an increase in CT numbers relative to SECT.

However, on considering the CNR (**Figure 44b**), the differences between energies declined due to the greater noise at low energies, and even SECT at 80 kVp presented a greater CNR than VMI at 55 keV. Thus, even though CE is higher at 55 keV, noise compromises that value and seems to limit the DECT improvement to 50 keV in the phantom. This result is important for CT scanners that may have the possibility of using 70 kVp SECT. In those cases, the upper limit of VMI energy, which shows a CNR over that of 70 kVp, can change and strengthen the interval of VMI utility.

In the analysis in patients, we applied the formula in point 2.1.5, with both air and muscle as reference materials. Results are shown in **Table 5** and **Figure 45**.

Table 5. Results of contrast-to-noise ratio (CNR) relative to the MIX series (with iodine contrast) in the study of 15 patients

		CNR relative to MIX						
Reference material		**40 keV**	**45 keV**	**50 keV**	**55 keV**	**60 keV**	**80 kVp**	**MIX**
Air	Mean	3.9	3.1	2.5	2	1.7	1.3	Ref = 1
	SD	0.6	0.4	0.3	0.2	0.2	0.2	1
Muscle	Mean	2.1	2	1.8	1.7	1.4	1.2	1
	SD	0.4	0.3	0.3	0.2	0.2	0.1	1

Note: Standard deviations (SD) refer to the CNR, not to the SDs of CT numbers observed in the reference materials.

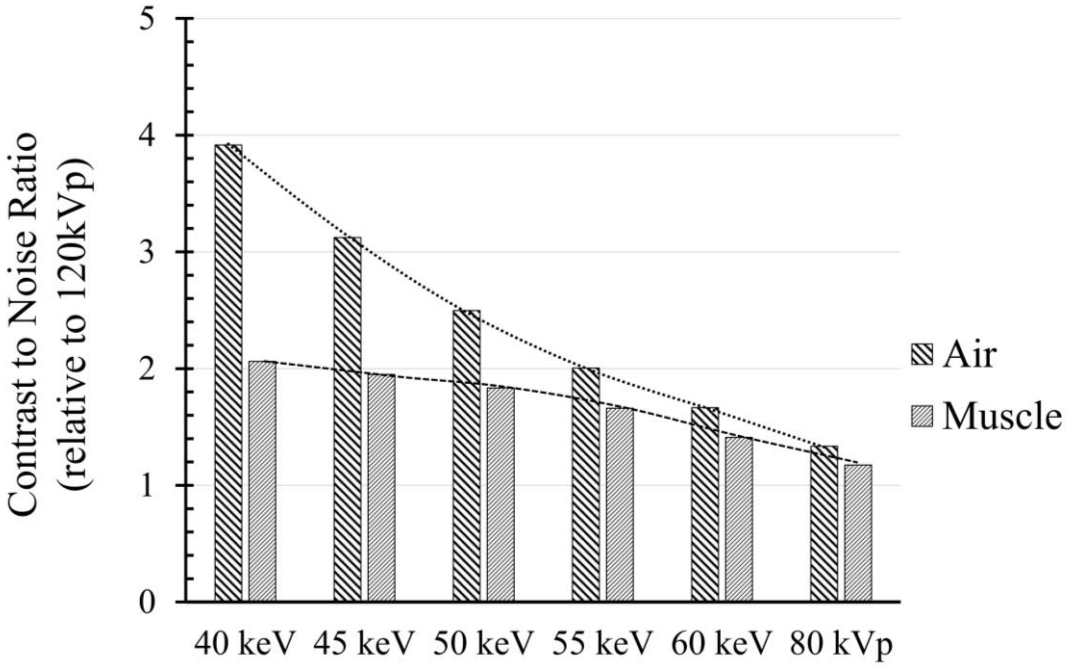

Figure 45. Contrast-to-noise (CNR) results relative to MIX series with iodinated contrast. When using air as reference material, CNR shows a great increase at low energies. However, when muscle is used, CNR tends to saturate at low VMI energies, due to the increase in noise. In real patients, doctors compare tissues, so the CNR is more similar to that calculated with muscle. Author's data.

2.3 Discussion

Uniformity is an important issue in CT imaging. The International Electrotechnical Commission (IEC)[94] recommends the same value as our manufacturer, ± 4 HU between central and peripheral regions. However, the IEC allows a maximum tolerance up to ± 7 HU, slightly more the manufacturer.

VMI series at 45 keV or higher showed sufficient uniformity to be used for diagnostics and simulations in RT treatments. In fact, all the series presented acceptable values of uniformity according to the established criteria in the common standards. However, those at 40 keV were at the limit of acceptability, and a substantial proportion (35%) exceeded the standards set by the manufacturer. In addition, these series showed a high level of noise. Therefore, 40 keV should be outside the range of normal use for VMI. Due to the high contrast enhancement of those images, they can be useful in regions where iodine uptake is low, but using them for CT number comparisons should be done with caution due to their lack of uniformity.

With regard to image resolution, the series between 45 keV and 60 keV yielded very similar values to the SECT series at 80 kVp and 120 kVp, indicating that they can be used without compromising this quality parameter. Specifically, the deviations observed in comparison to the series at 120 kVp show a comparable high-contrast resolution for all the series studied, with no appreciable differences between VMI and SECT.

For the LCR, the American College of Radiology accreditation program proposes the CNR method with a minimum value of 1.0 for head protocols. Our results with this method were not conclusive. None of the cylinders had a CNR over 1 at the contrast levels of 0.5% and 0.3%, even though some of these cylinders were visible to the naked eye in the averaged low-noise images. This result is similar to Gulliksrud et al.[95], suggesting that the remaining noise after averaging still affects CNR. Due to this limitation, we propose the statistical method presented by other authors[87,88], with a modification to avoid the undesired effects of a circular artifact. This model shows a better fit to the visual observation while being less sensitive to noise. If we translated this result to clinical situations where it is difficult to decrease noise, as we did in this study, we could not affirm that LCR is worse or better in one type of series or another. What we found was a high decrease in resolution in all series when noise increases.

On comparing the method based on CNR versus the method proposed here for measuring LCR, we observed that in all the series and at all contrast levels, a CNR of more than 0.5 corresponded to a statistically significant difference between the ROIs of the cylinders and the local noise. For CNR values under 0.5, there was a statistical correlation between the two factors, with a Pearson's correlation coefficient of −0.673, indicating that a reduction in the CNR led to a decrease in the p value.

Upon analyzing the magnitude and texture of the noise, the VMI series at 60 keV presented an NPS that was very similar to the SECT at 80 kVp, suggesting a quasi-equivalence between them in terms of noise. Matsumoto et al.[96] found that between 67 keV and 72 keV, the noise level was less than for the SECT images at 120 kVp, a result that could indicate that the range of use for VMIs could be around 70 keV. Our results seem to be in line with that because we observed a decrease in noise with an increase in energy, with equivalent values at 80 kVp and 60 keV. The explanation to that effect comes from the acquisition itself. The higher the VMI energy is, the higher the Compton effect

and the 140 kVp contribution. The 80 kVp series account for the photoelectric effect, while the 140 kVp series have only Compton scattering. When VMI energy increases, the balance between the low and high images tends to approach the 140 kVp level, which is less noisy than the 80 kVp series. That is why noise decreases as the weight of the 140 kVp images increases.

Matsumoto et al. also assessed iodine sensitivity in terms of CNR, finding that it peaked at 68 keV for concentrations of 5 mg/mL to 15 mg/mL, much higher than the concentrations used in our study. Their study was done before the introduction of the new generation VMI algorithms used in this work, the so-called Virtual Monoenergetic+ (MonoE+)[24,34,97], which radically decreased the noise level. With MonoE+, the noise reduction increases CNR at low energies, bringing sensitivity to contrast at the very low concentrations used here. That is why we found a CNR increase even at energies as low as 40 keV.

According to our results, series at 40 keV to 55 keV improve the CNR relative to 60 keV. Moreover, Matsumoto et al. did not compare the CNR with the SECT series at 80 kVp, and our results show that this series brings a higher iodine sensitivity than at 60 keV or even 55 keV. The use of 80 kVp thus cancels out the advantages of any energy levels over 60 keV. Furthermore, it is necessary to combine two acquisitions to obtain VMIs, so the SECT series at 80 kVp may present fewer uncertainties in the reconstruction due to series registration or changing iodine concentration, than those at 55 keV and 60 keV, as they require only one acquisition.

The series at 55 keV show a somewhat higher iodine sensitivity compared to that at 80 kVp, but the opposite occurs with the CNR, even though the difference between them is very small. This result suggests that the upper limit of the range for using VMI should be approximately 55 keV.

Leithner et al.[98] concluded that images at 40 keV of real patients with iodinated contrast, calculated by means of the algorithm MonoE+, show better image quality in a Siemens Dual Source CT in terms of CNR. Our results for CNR in a phantom are in line with their results, even though our system is a dual-spiral DECT. However, Leithner et al.'s results did not translate into better diagnostic performance. We observed that 40 keV images lack

uniformity and have a higher noise in our phantom analysis, suggesting that limitations in diagnostics could be related to the quality characteristics of the images.

Our in-phantom results are in line with previous clinical studies analyzing the range of energies in VMI for both diagnostics and radiotherapy, which concluded that for most sites, images at 40 keV present too much noise, and the range for using VMI should be between 50 keV and 70 keV[78]. For head and neck tumors, some authors have also demonstrated that even though images present greater CNR at 40 keV, the subjective assessment of the series at 55 keV is better for clinicians[97]. This result is also in line with our work.

When we analyzed CNR in real patients, we observed an increase in CNR related to the 120 kVp series in all the analyzed range of VMI. However, looking at the results in **Figure 45**, CNR with muscle as noise background tends to saturate at low energies because of the increased noise. In fact, 40 keV shows a non-significant difference with 45 keV ($p = 0.18$), and 45 keV is not statistically different from 50 keV ($p = 0.15$). Nevertheless, 50 keV is different from 55 keV ($p = 0.038$). Those results suggest that the interval of VMI energies between 45 keV and 50 keV maximize CNR and produce similar results when applied to real patients. Above this interval, CNR decreases and tends toward the SECT 80 kVp, and below that interval there is no improvement in CNR.

Finally, in Albrecht et al.'s[70] review, the authors recommend the series at 50 keV for having an optimal combination of quality and sensitivity to the contrast in clinical cases, a result that coincides with the conclusions of our study. This concordance suggests that the physical parameters of image quality translate directly to objective and subjective quality characteristics in real-life patients. Therefore, the implementation of dual-energy protocols with VMI in other anatomical locations should be preceded by the physical parametrization of image quality in phantoms in order to establish the optimal range of utilization.

2.4 Conclusions

According to our results and discussion, we can affirm that

1) Dual-spiral DECT allows the creation of VMI series with good quality according to CT standards.
2) VMIs have a high contrast-to-noise ratio when iodine is injected.
3) The optimal range where VMIs are clearly superior to SECT 80 kVp and 120 kVp in terms of contrast-to-noise ratio is between 45 keV and 50 keV.

NOTE:

This part of the research study has been published in the Medical Physics journal (The International Journal of Medical Physics Research and Practice). https://aapm.onlinelibrary.wiley.com/journal/24734209:

Fernandez-Velilla Cepria E, González-Ballester MÁ, Quera Jordana J, et al. Determination of the optimal range for virtual monoenergetic images in dual-energy CT based on physical quality parameters. *Med Phys*. 2021;48(9):5085-5095. doi:10.1002/mp.15120

3. Utility of Virtual Monoenergetic Images in Target Delineation

3. Utility of Virtual Monoenergetic Images in Target Delineation

The correct delineation of the gross target volume (GTV) is critical in RT treatment planning. Several factors influence GTV delineation, with interobserver variability (IOV) standing out as one of the most important[69]. Together with the observers themselves, imaging modality and quality are the most important factors that may affect IOV.

Radiation oncologists use a multimodal approach to improve volume delineation. Particularly in the head and neck region, the usual way to do this is by registering computed tomography (CT) images to fluorodeoxyglucose (FDG)-positron emission tomography (PET) and magnetic resonance imaging (MRI), which decreases the IOV[99,100,101].

Registration of different imaging modalities is a challenging task, and its accuracy is hampered by uncertainties stemming from different patient positions, acquisition times, geometrical distortions, and image resolution. In order to reduce such uncertainties, a CT-based imaging procedure with a better contrast between tissues may have some advantages because CT images are used for RT treatment planning and calculations.

Dual-energy virtual monoenergetic images (VMIs) show high contrast enhancement in the presence of injected iodine, which may lead to improved diagnostics and evaluation of head and neck tumors[102]. Currently, the most common use of DECT images in radiotherapy is to delineate GTV with the help of the VMI series because DECT images may help radiation oncologists to better identify GTV[103,104] and improve delineation. It is still unclear whether they reduce IOV, and few studies consider delineation time as an indicator of improvement in delineation. Decreasing IOV means smaller discrepancies between observers when delineating the same GTV.

However, IOV measurement is not straightforward because there is no single method or parameter that represents it. To assess IOV, we studied the objective reduction of IOV with different parameters, volumetric and vectoral, and assessed a possible improvement in GTV visualization as a function of oncologists' subjective preferences and the time needed for delineation.

Our study tries to bring to light the potential advantages of DECT in GTV delineation. We studied the objective reduction of the IOV and assessed a possible improvement in tumor visualization and delineation as a function of oncologists' subjective preferences and the time needed for delineation.

The main limitation of the present work was the type of DECT imaging. Our CT system, Siemens Somatom Confidence RT Pro, is a dual-spiral DECT system. This procedure introduces some uncertainty due to motion artifacts and a changing concentration of iodine in the patients. There are no studies about IOV using DECT in other systems, but our results might not be generalizable to such systems.

3.1 Materials and methods

This part of the study included 15 consecutive patients affected by tumors of the head and neck region who were candidates for RT treatment. 3D CT simulation was performed in all patients with the standard 120 kVp protocol without iodinated contrast for planning calculations (slice thickness 2 mm, field of view 50 cm). For all patients, an additional dual-energy study with iodinated contrast (Optiray Ultraject) was performed for better tumor visualization. Acquisition was done immediately after the injection of iodine in one phase (total injection time 33 s). The DECT study was acquired by means of consecutive acquisitions at 80 kVp and 140 kVp with the Siemens Somatom Confidence RT Pro CT. We reconstructed VMI series at 40 keV, 45 keV, 50 keV, and 55 keV.

Although the aim of the study was to determine the potential advantage(s) of VMI delineation over SECT 120 kVp, we skipped the acquisition of a third scan at this kilovoltage with iodine enhancement in order to limit the imaging dose to the patients. Instead of 120 kVp, we used the MIX images because they are known to be almost equivalent.

Six senior radiation oncologists and two resident physicians were asked to delineate the GTV in all patients and series. Thus, each GTV had eight delineations per series. All contours were created in the Contouring module in the Varian Eclipse v.13.6 Treatment Planning System.

3.1.1 Delineation and contrast

Before starting delineation, we performed a subjective analysis of the images. Doctors were asked to examine all series for each patient and rank them from 1 (best series for delineation) to 6 (worst). The best series for delineation was defined as the one with the least noise and the most contrast. The worst were the series with the most noise or where the GTV was not visible due to a lack of contrast. The aim of this part of the study was to identify any existing correlation between the subjective score and IOV.

Each doctor delineated the GTV for all 15 patients in one week but only performed one series per patient. Since a patient might have more than one GTV, only one GTV per patient was chosen and marked with a cross. The order of series to be delineated was selected randomly and conducted by an automatic workflow. After each delineation, volumes were hidden, and the window was reset to 2000 with center = 0. Window resetting was considered an important point because standard windows do not apply in VMI and 80 kVp series, and this could cause IOV (Fig. 46)**.**

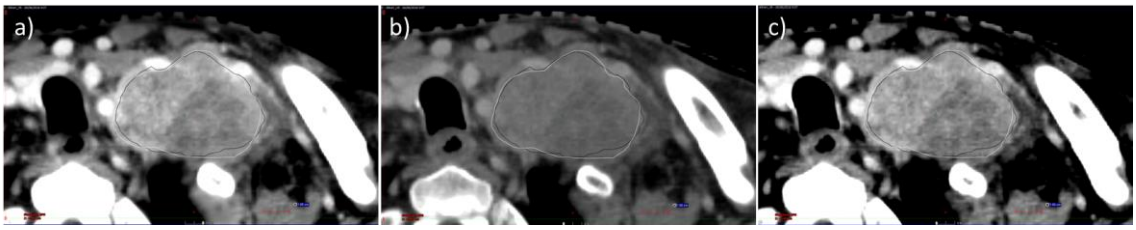

Figure 46. Importance of a correct windowing when using VMI. a) VMI at 40 keV. Window (W) = 420, center (C) = 110. CNR = 71.4 b) Image at 120 kVp. CNR = 6.8. Same window and center as in a). The lower CNR causes a lack of optimization. This forces the manual selection of W and C. c) Optimized image at 120 kVp. W = 160, C = 60. Settings of W and C are very different from that of 40 keV.

In a parallel test, doctors had to annotate the time between the moment they opened the series and the moment they saved the delineated volume. We wanted to know whether delineation on DECT images was faster or not, compared to delineation in SECT. We considered agility in delineation as an indicator of ease for oncologists and thus an improvement over SECT. We also calculated the correlation coefficient (Spearman rank test) between those values and the results of the subjective ranking.

After delineation, we measured the CNR of all the GTVs to compare the VMIs to SECT in terms of contrast enhancement and to have a patient-related factor to correlate with any difference in IOV we could find in this study.

3.1.2 Interobserver variations

As our objective was to assess variability, not quality of delineation with respect to a gold standard, for each series we considered the overlap between the eight doctors' GTVs as the reference to evaluate variations. This selection had many advantages when evaluating IOV, as described below.

All volumes were delineated in the Varian Eclipse 13.6 Contouring module, exported in digital imaging and communication in medicine (DICOM) RT format, and converted to text files by means of the Plastimatch freeware application. Text files were imported into Microsoft Excel, and all calculations were performed with Visual Basic macros programming.

According to Vinod et al.[105], there is a wide range of methods for evaluating IOV, and no single parameter gives enough information for a rigorous assessment. Thus, we measured IOV using several methods, encompassed within two types: 1) methods based on volume relationships and 2) methods based on point-to-point distances (**Table 6**).

a) Methods based on volume relationships

We calculated three commonly used volume-related factors: the Jaccard index (JI), Sorensen-Dice coefficient (DC), and the geographical miss index (GMI).

Numerically, the JI, DC and GMI between two volumes *A* and *B* can be calculated following these formulas:

$$\mathrm{DC} = \frac{2 \cdot A \cap B}{A + B} \qquad \mathrm{JI} = \frac{A \cap B}{A \cup B} \qquad \mathrm{GMI} = \frac{A - (A \cap B)}{A} \mathrm{x}100$$

In our study, the selection of the overlap as the reference volume in all series created a numerical relationship between the DC, GMI and JI:

When volume *B* is the overlap, $A \cap B = B$, and $A \cup B = A$. Then,

$$\mathrm{DC} = 2 \cdot \frac{\mathrm{JI}}{\mathrm{JI} + 1}$$

And with the same assumption:

$$\mathrm{GMI} = (1 - \mathrm{JI}) \cdot 100$$

From the previous expressions, using the overlap of a series as reference volume for comparisons, variations in GMI and DC are directly related to those of the JI. We computed the three factors to check the accuracy of our Visual Basic macros, but we used DC as volumetric comparison factor because it is the most commonly used in the literature[106].

Table 6. Summary of methods used in this study for geometrical comparisons and their results

Type of method	**Parameter**
Volume comparison	Jaccard Index
	Dice coefficient
	Geographical Miss
Distance between surfaces	Hausdorff distance (HD)
	Vectoral distance to agreement $\overrightarrow{r_\Delta}$
Combination	Combined Dissimilarity Coefficient CDF

Note: Description and formulas described in the text.

b) Methods based on point-to-point differences

We first computed Hausdorff distance (HD) as a commonly accepted method. As HD accounts only for maximum distance and misses information about the complete set of points, the literature describes several methods to fill these information gaps[107-109]. We used a radial method to parameterize the point-to-point distance between the overlap and the GTV drawn by the different doctors. The description is as follows (**Figure 47):**

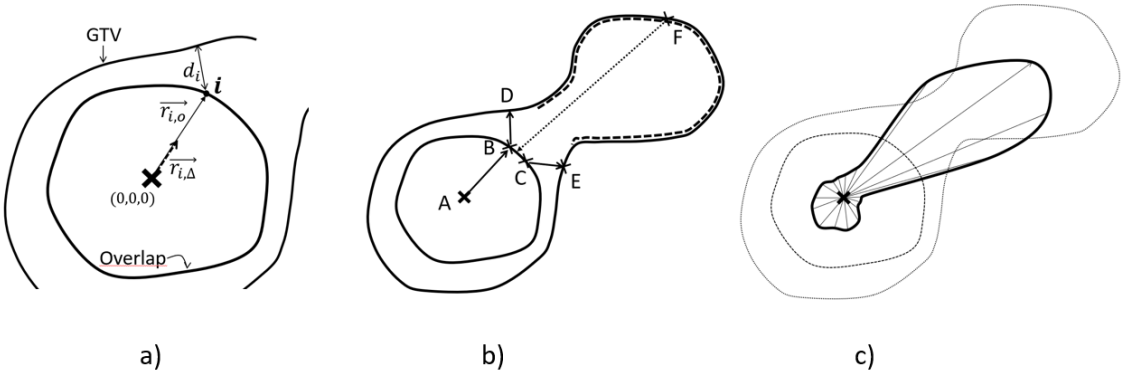

Figure 47. Vectoral interobserver variations. a) Values of $\overrightarrow{r_{i,o}}$, d_i and $\overrightarrow{r_{i,\Delta}}$ for any point *I* in the overlap between GTV delineated by any doctor. b) Points *B* and *C* have their shortest distances at points *D* and *E*. The region where point *F* is located (dotted line) needs to be identified because its points are not the shortest distance for any of the overlap points. Thus, GTV to overlap distances measured at these points must be considered separately. c) The bold line represents the final shape composed by all the vectors $\overrightarrow{r_{i,\Delta}}$.

First, we calculated the centroid of the GTV overlap, establishing this point as the origin for coordinates (X, Y, Z), where X is the right-to-left direction, Y front-to-back, and Z head-to-toe. Let d_I be the minimum distance from point *I* to the GTV under analysis. Selecting the overlap as reference guaranteed that all d_I were positive or zero (**Fig. 47a**). Each point *I* of the overlap GTV has a position vector $\overrightarrow{r_{I,\Delta}}$. Then we calculated a difference volume with its points $\overrightarrow{r_{I,\Delta}}$ located in the same directions of the overlap points but their module equal to d_I (**Figure 46a**):

$$\overrightarrow{r_{I,O}} = d_I \cdot \frac{\overrightarrow{r_{I,O}}}{\left|\overrightarrow{r_{I,O}}\right|}$$

To prevent skipping areas like the one shown in **Figure 47b**, our software analyzed possible areas of the volume not considered in the calculation and forced those points to be measured in the opposite direction, from GTV to overlap. The final distribution of vectors $\overrightarrow{r_{I,O}}$ can be seen in **Figure 47c**.

In the next step we calculated the mean vector of differences:

$$\overrightarrow{r_\Delta}(X, Y, Z) = \frac{\sum_I \overrightarrow{r_{I,O}}}{\sum_I \left|\vec{r}_{I,\Delta}\right|}$$

The mean vector $\overrightarrow{r_\Delta}$ is an indicator of symmetry, and its direction indicates the overall direction of volume variations. We analyzed the $\overrightarrow{r_\Delta}$ deviations of all series and volumes to find out if there was a predominant direction for differences.

c) Combined dissimilarity factor

After applying volume- and coordinate-related methods, we combined the two by means of the DC and the $\overrightarrow{r_\Delta}$. For each GTV we made a graphical representation where the Y axis was the value 1 − DC and the X axis was $r_{\Delta,\mathrm{nor}} = \left|\frac{\overrightarrow{r_\Delta}}{\vec{r}_{\Delta,\mathrm{max}}}\right|$, where $\vec{r}_{\Delta,\mathrm{max}}$ was the maximum value of $\overrightarrow{r_\Delta}$ for the studied volumes (**Figure 48**).

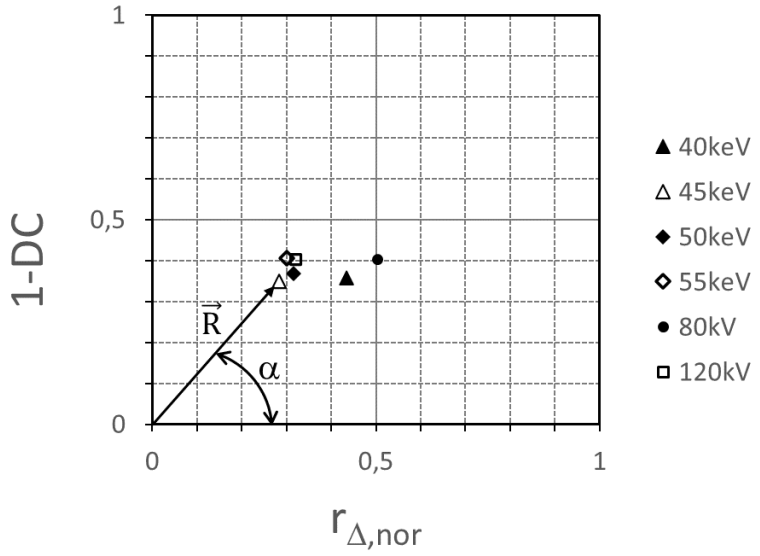

Figure 48. Bi-dimensional representation for one patient at all energies. The origin (0,0) represents a perfect matching of volumes. Contours approaching point (0,1) show a big difference in volume (DC near 0) but good symmetry, and contours approaching point (1, 0) show a good volume similarity but a lack of symmetry. The shorter the R, the better the similarity. In this case, differences in volumes (Y axis between 0.35-0.41) are smaller than differences in symmetry (X axis 0.28-0.50).

The selection of both factors was done because the DC has an interval of values between 0 and 1, with 1 indicating total coincidence and 0 no coincidence at all, and so 1 − DC gives the opposite values, where 0 shows total coincidence. On the other hand, $r_{\Delta,\mathrm{nor}}$ has a value of zero when perfect symmetry exists, and its values are between 0 and 1. In this graphical representation, the distance to the origin becomes an indicator of how different volumes are, and the argument of the vector shows which kind of differences predominate: volumetric or symmetrical.

Finally, the combined vectoral parameter for volume comparison is (**Figure 47**):

$$\vec{R} = (r_{\Delta,\mathrm{nor}}, 1 - \mathrm{DC})$$

From this expression we can derive a combined dissimilarity factor (CDF) as:

$$\mathrm{CDF} = \sqrt{{r_{\Delta,\mathrm{nor}}}^2 + (1 - \mathrm{DC})^2}$$

Additionally, its argument can be calculated as:

$$\propto = \mathrm{Arg}(\vec{R}) = \tan^{-1}\frac{(1-\mathrm{DC})}{r_{\Delta,\mathrm{nor}}}\ (0 \leq \mathrm{Arg(R)} \leq \prod/2)$$

We qualitatively compared the combined vectoral analysis of dissimilarity with the DC and the vectoral distance to agreement. In our study, we used the overlap as the reference volume. Different situations can be observed in **Figure 49**. Their representation in the 2D space is shown in **Figure 50**. The qualitative comparison is done by comparing the distance between each point to the axis origin.

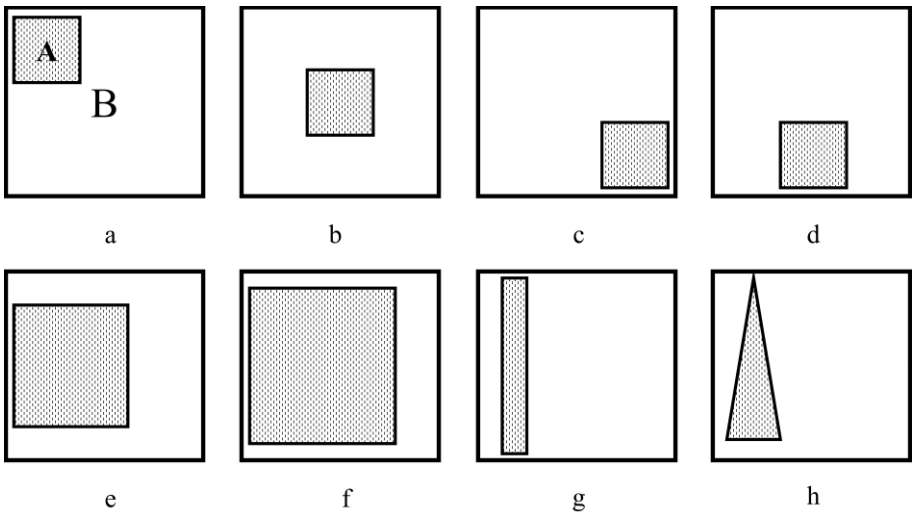

Figure 49. Different situations selected among the infinite possibilities to check if the combined dissimilarity accounts for differences.

Situations like the one shown in **Figures 49a**, **c**, and **d** are the same in terms of DC. Namely, they are equal in dissimilarity because they have the same volume relationship and there are only geometrical displacements. However, the displacement in **Figure 49d** is lower than in **a** and **b**. Thus, d is slightly better than the others. While DC does not account for this difference, CDF in **Figure 50** shows a horizontal displacement of point **d**.

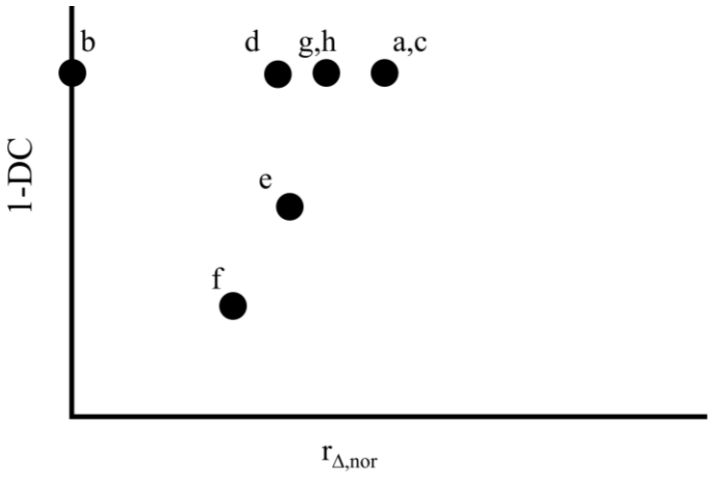

Figure 50. Qualitative 2D graphical representation of volumes shown in **Figure 49**.

Figures 49 e and **f** are well accounted for by means of DC because there is a difference between volumes. Again, there is a difference position that is accounted for by *r*. Volumes A and B are more similar in **f** than in **e**, and far more similar than **a-d**. In the graphical representation, points **e** and **f** are clearly closer to the origin of coordinates.

Unfortunately, neither DC nor *r* can account for the differences observed in **Figures 49 g** and **h**. The A and B areas are exactly the same, and so is the DC coefficient. Additionally, *r* is the same for both. In this kind of situation, the combined dissimilarity factor cannot account for differences in shape.

In summary, the combined dissimilarity factor is a graphical method to easily compare dissimilarities, but some limitations of DC and vector distance remain with regard to the particular volume shapes.

3.2 Results

3.2.1 Subjective and time analysis

Subjective analysis was done before any delineation. Doctors looked over the images and ranked them according to which series they thought would be the best and the worst for delineation. In this step, the window was 2000 and center = 0. Doctors were free to change windowing to improve visualization.

Table 7 shows the results of the subjective and time analysis. In 48% of the 120 combinations of patients and doctors (8 doctors × 15 patients = 120), 40 keV was selected as the best series for delineation (48%), followed by 45 keV (15%). The lowest scores were for 80 kVp and 120 kVp (5% each). When analyzing the oncologists' preferences one by one, one doctor preferred 120 kVp (in 6 patients, 40%) and never selected 40 keV.

Table 7. Results of subjective image ranking

Energy	Rank in subjective analysis[a] (1 best, 6 worst)	Mean rank in time for delineation[b] (1 shortest, 6 longest)
40 keV	1 (48.3%)	1 (2.26)
45 keV	2 (15%)	5 (2.62)
50 keV	3 (9.2%)	2 (2.24)
55 keV	4 (8.3%)	4 (2.57)
80 kVp SECT	5 (5%)	3 (2.4)
120 kVp SECT	5 (5%)	6 (2.9)

[a]In the subjective analysis, SECT 80 kVp and 120 kVp share the same score because they were identified as the best in the same number of cases (5% each). The total percentage is 90.2% because oncologists considered quality to be equal in 9.8% of cases. Results in parentheses show the percentage of cases where each energy was ranked as the best.

[b]Rank of mean time for delineation. In parentheses, mean score for each energy. 45 keV and 55 keV showed only a small difference that cannot be considered relevant. The same occurred with 40 keV and 50 keV.

Regarding the time for delineation, doctors were instructed that the time counter started at the instant when they double-clicked the mouse to open the images and finished when they clicked the "save" button. Even though instructions were clear, many clearly erroneous times were recorded. In fact, results showed a substantial variability that made it impossible to find a trend or relationship with energy. Nevertheless, some results could be gleaned from the data: for the maximum and minimum times, 40 keV was the quickest in 21.9% of the cases, followed by 50 keV (16.7%). On the other hand, 120 kVp was the slowest series in 25% of the volumes, followed by 55 keV (16.7%). Spearman's rank test showed that these results were significantly correlated to the subjective ranking with 95%

confidence ($\rho = 0.957$). However, we did not observe a significant correlation between CNR and time for delineation.

When analyzing the mean score of the time rank, including not only the extreme values but also the intermediate ones, images at 40 keV and 50 keV still had the lowest scores (2.26 and 2.24, respectively). The slowest energy was 120 kVp, followed by 45 keV and 55 keV (2.62 and 2.57, respectively). However, variations were too big to derive conclusions.

3.2.2 Volume-related factors

The objective here was to find out whether the use of VMIs reduces IOV. Results are summarized in **Table 8**.

To check the accuracy of our Excel macros for factor calculations, we plotted the DC in terms of the JI. Results are shown in **Figure 51**.

For the DC (as well as the JI and GMI), we observed only negligible differences between energies. The mean DC between energies and patients was 0.703, with the lowest value at 50 keV (0.684) and the highest at 80 kVp (0.715). Between patients, mean values of DC varied from 0.562 to 0.850. We did not observe a relationship between DC and CNR or energy. When analyzing SDs to assess the possible increase in uncertainty at different energies, the same results were obtained for DC (min SD 0.083, max 0.15).

When analyzing patients one by one, we found that doctors ranked patients according to their DC in almost the same order. This result suggests that some patients have more delineation complexity than others, which can affect IOV. However, we did not find any relationship between DC, energy, and complexity.

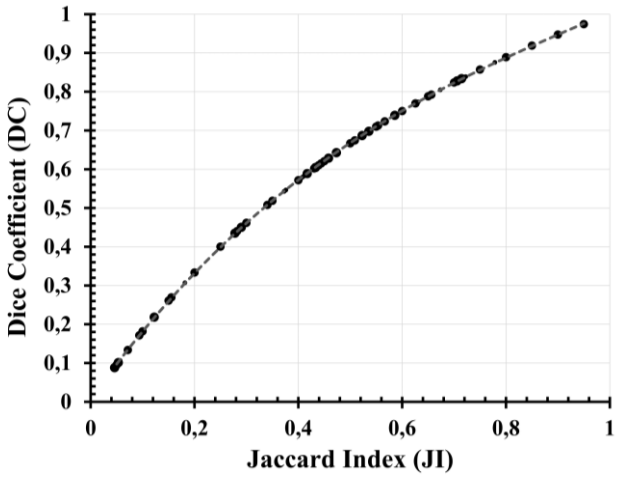

Figure 51. Plot of Dice coefficient vs Jaccard index. Black points represent experimental data of real gross target volumes. The dotted line is the analytical function DC = 2·JI/(JI+1), showing an almost exact fit.

Table 8. Summary of results grouped by types of methods. Standard deviations (SD) are high in relationship to mean and maximum values. Only vectoral distance to agreement shows a reduction when using VMI images, but the high SD values make that result statistically non-significant.

Parameter		VMI (40-55 keV)	80 kVp SECT	120 kVp SECT
Volume comparison				
Jaccard index	Mean	0.47 (SD 0.19)	0.48 (SD 0.21)	0.47 (SD 0.21)
	Max	0.48 (40 keV)		
	Min	0.46 (55 keV)		
Dice coefficient	Mean	0.70 (SD 0.1)	0.71 (SD 0.1)	0.71 (SD 0.1)
	Max	0.71 (45 keV)		
	Min	0.68(50 keV)		
Geographical miss	Mean	52.7 (SD 19)	51.7 (SD 21)	52.7 (SD 21)
	Max	53.8% (55 keV)		
	Min	51.8% (45 keV)		
Distance between surfaces				
Hausdorff distance (mm)	Mean	9.7 (SD 5.1)	10.2 (SD 5.6)	11.2 (SD 6.4)
	Max	10.4 (55 keV)		
	Min	8.9 (40 keV)		

Vectoral distance to agreement $\lvert\overrightarrow{r_\Delta}\rvert$(mm)	Mean	0.33 (SD 1.44)	0.62 (SD 1.65)	0.61 (SD 2.28)
	Max	0.44 (40 keV)		
	Min	0.18 (45 keV)		
Combination				
Combined dissimilarity coefficient	Mean	0.53 (SD 0.20)	0.56 (SD 0.24)	0.56 (SD 0.25)
	Max	0.54 (45 keV)		
	Min	0.51 (40 keV)		

3.2.3 Geometrical factors

Mean Hausdorff Distance (HD) increased with CT energy (**Figure 52**). The lowest mean values and SDs were found at 40 keV (mean 8.9 mm, SD 4.4), and the highest at 120 kVp (mean 11.2 mm, SD 6.4). When considering mean HD values, the Pearson correlation coefficient between HD and CNR was −0.865.

The analysis of vector $\overrightarrow{r_\Delta}$ shows only a small variation in symmetry in the X and Y directions, which are the horizontal and vertical axes in a CT image. The averaged maximum lack of symmetry in the X direction was 0.1 mm (SD 0.48) at 80 kVp and the minimum 0.01 mm (SD 0.45) at 50 keV. For the Y axis, the maximum measured value was 0.22 mm (SD 0.58) for the 55 keV series, and the minimum was 0.05 mm (SD 0.49) at 45 keV. SDs were similar for all energies in the X and Y directions (in-slice). Thus, as shown in **Table 9**, differences are small and not related to energy. It is remarkable that deviations in the head-to-toe direction (inter-slice) are clearly higher that those in the in-slice directions.

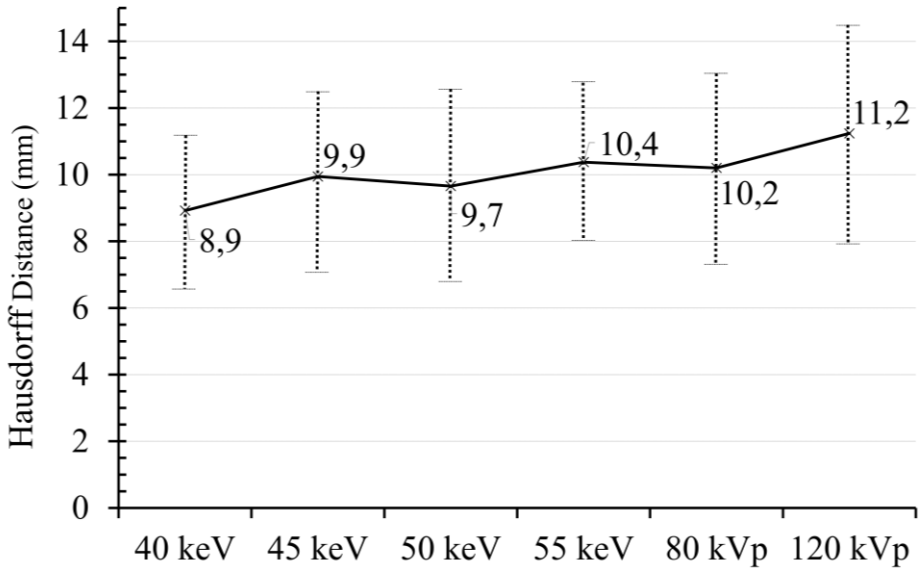

Figure 52. Hausdorff distance increases with energy. However, this result is not statistically significant due to the large standard deviations (vertical lines correspond to 1 SD).

In the Z direction (head-to-toe), values were higher because the acquisition protocol had less resolution. While in X and Y directions resolution was 0.97 mm, in Z it was 1.5 mm. Thus, Z variations were bigger than X and Y at all energies. Both mean values and SDs in the Z direction showed the lowest values at 45 keV and the highest at 80 kVp and 120 kVp. An example of how these differences appear is shown in **Figure 53**.

The analysis of the combined dissimilarity factor (CDF) showed small differences: the maximum value was 0.56 at 120 kVp (SD 0.25) and the minimum 0.51 at 40 keV (SD 0.21). CDF increased with energy, as did its SD. Pearson statistics between mean CDF and mean CNR yielded a correlation factor of −0.859, but when introducing data for all patients and volumes, no correlation was found.

Table 9. Results for the vectoral differences (mm)

		40 keV	45 keV	50 keV	55 keV	80 kVp	120 kVp
X direction	Mean	0.03	0.07	0.001	0.01	0.10	0.03
(left-right)	SD	0.55	0.49	0.45	0.37	0.48	0.77
Y direction	Mean	0.11	0.05	0.15	0.22	0.08	0.16
(front-back)	SD	0.41	0.49	0.47	0.59	0.43	0.53

Z direction	Mean	0.42	0.16	0.43	0.30	0.61	0.59
(head-toe)	SD	1.40	0.98	1.39	1.29	1.52	2.08

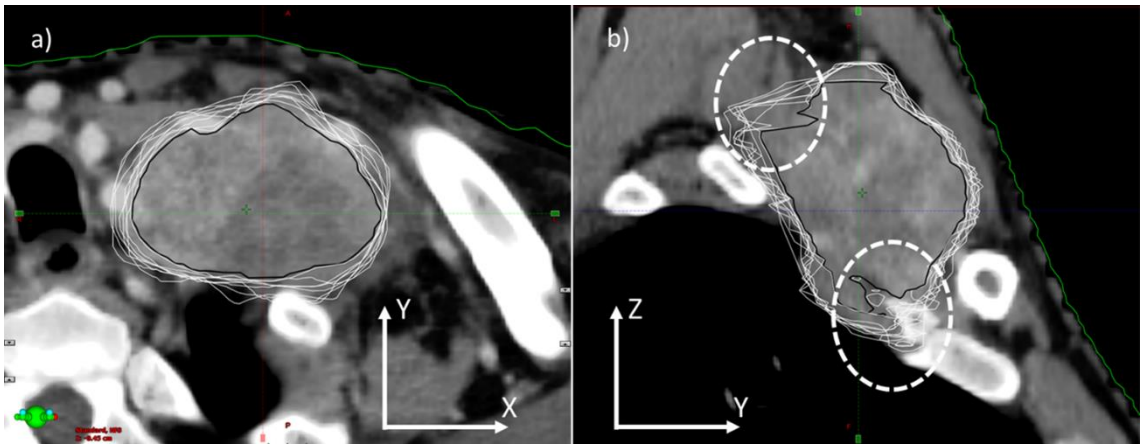

Figure 53. Example of X, Y, and Z variability in delineation. a) Cross-sectional slice. The white lines are the different gross target volumes delineated by doctors. The black line is the overlap. Interobserver variability (IOV) is similar in the X and Y directions. b) Sagittal reconstruction of the same volume. Dotted lines highlight zones with a superior IOV in the Z direction.

3.3 Discussion

Despite the higher noise observed at low VMI energies, CNR showed the same characteristics in all patients. First, the highest values were at 40 keV; second, the higher the energy, the lower the CNR; and third, SECT 80 kVp and 120 kVp showed the lowest CNR values. However, we found large differences between patients. These results are in keeping with the expected improvement in tumor visualization due to the use of DECT VMIs[102]. However, studies such as Leithner et al.'s[98] cast doubt on whether an increased CNR improves diagnostics. These doubts do not apply to our work because we do not deal with the problem of diagnostics; in RT planning oncologists already know the extent and location of the tumor, and they just use images for delineation. Thus, the important issue for radiotherapy is a high CNR that allows a clear delineation of the tumor or tissues boundaries in a known location. Moreover, radiation oncologists usually delineate in a multimodal environment, assisted by MRI and/or PET.

Several studies have analyzed the subjective characteristics of DECT images[71,110], lending support to the idea that VMIs improve imaging in the head and neck due to their

superior contrast enhancement. In our subjective analysis, doctors preferred 40 keV and 45 keV for delineation. These results are consistent with studies by Forghani et al.[43] and Albrecht et al.[70] but differ from Wichmann et al.[71], who defined 60 keV as the best for tumor delimitation when comparing DECT images at 40 keV, 60 keV, 80 keV, and 100 keV. In our study, we compared DECT images up to 55 keV at intervals of 5 keV and added 80 kVp and 120 kVp SECT. We did not include 60 keV because 65 keV is commonly considered similar to 120 kVp, and we had also studied 80 kVp, which is similar to 55 keV. According to our work, 40 keV images have similar CNR but higher noise compared to 45 keV and 50 keV. Wichmann et al. did not assess the interval between 45 keV and 55 keV, which showed the best results in our study. Our results indicate that the best visualization interval in the head and neck region lays between 45 keV and 50 keV, and VMI energies over 55 keV are not appropriate.

We also assessed the time needed for delineation as an improvement factor. This parameter has been studied as one important feature of automatic or semi-automatic delineation algorithms[111,112,113], but our review did not identify any literature about that parameter in radiotherapy assisted by dual-energy CT.

Series at 45 keV to 55 keV showed a shorter delineation time compared to those at 80 kVp and 120 kVp, but there was no clear relationship between energy and time. On the other hand, the longest times for delineation were observed at 120 kVp, which coincided with the lowest CNR and the least preferred series. In summary, the extreme values were clear and statistically significant: 40 keV was the preferred and fastest for delineation, while 120 kVp was the least favorite and the slowest. For energies in the middle, we did not find any statistically significant results. This seems to support the idea that the real change is not between VMI energies, but in the leap between SECT 120 kVp and VMI at low energies.

A good measure of whether DECT improves delineation is to examine IOV, which should be objectively lower than for SECT images. To parameterize the IOV, we followed the recommendations of Fotina et al.[114], combining a descriptive analysis, overlap measure, and statistical measure of agreement to fully report variability in delineation. Several studies have shown that variability in GTV delineation is highest in the head and neck region when only CT imaging is used. Our results are in line with these studies, which

also report that IOV decreases in a multimodal environment[99,100,115]. For this reason, radiation oncologists commonly use MRI and PET to assist them in RT simulation. Our objective was to determine whether using VMIs from DECT improved IOV.

There is abundant literature about indexes for IOV determination. Following the recommendations of Remeijer et al.[107] and Vinod et al.[105], we combined volume- and distance-related factors.

For the distance-related factors, we settled on the models described by Rao et al.[108] and Pevsner et al.[109] and selected overlap between doctors for each series as a reference. This selection had two advantages: all minimum distances for GTV overlap were positive or zero, and the DC, JI, and GMI were analytically related. This redundancy was used to check the accuracy of the Excel macros used for calculations.

After finding the distribution of minimum distances, we calculated the average vector $\overrightarrow{r_\Delta}$ as an indicator of asymmetry. The direction of this vector shows the overall asymmetrical orientation, and its module is a measure of asymmetry. $\overrightarrow{r_\Delta} = 0$ is an indicator that any existing differences between volumes are symmetrical, but this does not mean there are no differences. According to our results, the lack of symmetry was the same in the in-plane X and Y directions, and smaller than the pixel size in mean. In the inter-plane direction, $\overrightarrow{r_\Delta}$ was higher because of the slice thickness, which was greater than the pixel size. These variations in $\overrightarrow{r_\Delta}$ agree with previous studies reporting the biggest deviations in the cranio-caudal (Z) direction[116,117]. The main reason is that our scanning protocol for head and neck had a slice thickness of 1.5 mm, while the in-plane resolution was only 1 mm. Nevertheless, this limitation itself does not explain the clear positive correlation that $\overrightarrow{r_\Delta}$ had with imaging energy, whereas SECT images showed the worst values in the Z direction. This finding suggests that VMIs decrease uncertainties in the Z direction, possibly because a better CNR reduces error in the identification of GTV in the upper and lower slices where the partial volume artifact can be present. Thus, DECT appears to be especially useful in doubtful areas.

Considering the other point-to-point parameter, Hausdorff distance, it was lower in VMIs. This means that the maximum values of separation between points were found in the SECT series, suggesting again some level of uncertainty related to areas where CNR at high energies is not high enough but can take advantage of the enhanced contrast at low

VMI energies. However, that observed trend was not statistically significant due to the high variability in HD between delineations. In summary, the HD results are congruent with the observed vectoral differences even though HD is neither a vectoral nor an averaged magnitude.

Regarding volume-related factors, we did not find differences between energies or any improvement in the overall IOV between series in the DC index. Thus, as $\overrightarrow{r_{\Delta}}$ and DC provide supplementary information, we proposed combining them in a single vector, $\overrightarrow{R}$, to account for both volume and symmetry. This vector provides an easy way to visually compare GTV volumes in a 2D representation that can be reduced to a single factor, *R*, for numerical comparison. In our study this approach did not yield any remarkable results.

Moreover, our results showed that the combined dissimilarity factor (CDF) was statistically correlated with energy. However, due to the limitations of all the parameters commonly used to calculate IOV, such small differences do not support the idea that the use of dual energy decreases IOV.

In summary, we did not find any reduction in IOV due to the use of dual-energy CT. These negative results seem to support the conclusions of Leithner et al.[98], who called into question whether improved CNR translates to better diagnostics. Our work seems to extend that affirmation to tumor delineation in radiotherapy. That conclusion can be a consequence of different considerations at play.

- VMIs do not have standardized windows for visualization in treatment planning systems, so radiation oncologists have to manually select the windowing, with all the uncertainties entailed in this procedure.
- Iodine enhancement depends not only on the concentration and imaging energy but also on the visualization window.
- Motion artifacts, pixel size and slice thickness may blur points with a high iodine uptake, making delineation more difficult and subject to differences between oncologists.

Nevertheless, the subjective analysis showed that VMIs give oncologists more confidence in delineating the tumor boundaries, even though this confidence does not result in a smaller IOV.

Finally, an important limitation of our IOV study is that we did not divide patients in groups depending on clinical conditions such as primary site, stage, previous lymphadenectomy, or other variables. Such a grouping could result in more specific results on IOV in different patient subgroups and help to identify cases that might see a real improvement with DECT.

3.4 Conclusions

1) Dual-energy virtual monoenergetic images (VMIs) have some characteristics, like contrast enhancement, that make delineation easier for radiation oncologists.
2) Interobserver variability is not different between dual-energy and single kilovoltage CT, but VMIs help delineation in areas where volumes are not clear.
3) A graphical representation of the Dice coefficient and vectoral difference can bring a visual interpretation to compare dissimilarity between delineated volumes.

4. Accuracy of Dose Calculations on Virtual Non-contrast Images

4. Accuracy of Dose Calculations on Virtual Non-contrast Images

Iodinated intravenous (IV) contrast is commonly used in the RT delineation process, particularly in the head and neck region. Usually, IV use is accompanied by two CT acquisitions, before and after injection. Images without iodine are used for dose calculations, and the enhanced ones are used for tumor delineation. Although this is a common procedure, several studies have demonstrated that calculations on iodine-enhanced images are safe, and the derived uncertainties can be kept at tolerable levels, under 1%[75,118,119].

DECT is an alternative way to deal with iodine. Three-material decomposition algorithms allow a virtual removal of iodine that results in virtual non-contrast (VNC) images. Several papers have described features of VNC in different types of DECT (dual-source, twin-beam, dual-layer, and fast kV-switching), but there is a lack of evidence about the accuracy of plan dose calculations with dual-spiral DECT. The main concern about this technique is the temporal variation of iodine concentration in blood from the low- to the high-kVp acquisition. VMI- and VNC-derived series can be majorly influenced by those variations as well as by motion artifacts.

Different authors have determined some uncertainties in the CT number values in VNC images, related to the body dimensions and iodine concentration[120]. These are especially sensitive to temporal variations in iodine concentration during the acquisitions, which is why most previous studies have evaluated VNC images only from the aforementioned types of DECT. However, VNC images can also be obtained from dual-spiral DECT if enough time passes after iodine injection to avoid transient variations in iodine concentration. Different authors have estimated this interval to be at least 70 s after the start of the injection[118,119,120].

As dual-spiral DECT is a simple technological solution, many hospitals have adopted it, so its features in dose calculation must be well determined. For this reason, we studied the VNC images obtained by a dual-spiral DECT CT (Siemens Somatom Confidence RT Pro) and their accuracy in RT planning.

We calculated VNC images by means of Siemens SyngoVia vB.50 software. As our objective was to check the feasibility of calculations in VNC images obtained from a

dual-spiral DECT and to show their possible advantages, our conclusions may open the door to using that type of acquisition in RT planning.

The main limitation of our study comes from the fact that we did not study the influence of different IV injection patterns. We analyzed their application with a particular set of acquisition conditions that fulfill the requirements of VNC creation, following the manufacturer's recommendations and the literature.

4.1 Materials and methods

This study included 30 patients who underwent radiotherapy of the whole head and neck area (both tumor and lymph nodes). All cases had a SECT 120 kVp series without iodine enhancement for reference calculations, plus a DECT study with iodinated contrast. From the DECT study, we derived VMI 45 keV and MIX series in all patients, but VNC images were obtained in only 15 because of the limited availability of patients. The selection of 45 keV was based on the results and conclusions in chapter 2. All images were acquired by a Siemens Somatom Confidence RT Plus (field of view 50 cm, slice thickness 2 mm).

We injected the same quantity of 100 mL iodine solution (GE Healthcare Omnipaque 350 mgI/mL) to all patients in a single injection of 33 s. Patients were divided in two groups depending on the injection/acquisition pattern (**Table 10**).

1) In the first group (15 patients), the DECT scan was done immediately after the iodine injection was finished. This pattern was taken from the radiology department protocol for head and neck in hospital del Mar. In theory, the time between injection and acquisition was meant to maximize iodine concentration in blood and achieve a high CNR regardless of the influence of iodine in dose calculations. No VNC images were obtained in this group of patients.
2) In the second group, the acquisition of DECT images started 76 s after the start of injection (injection time 33 s, meaning the start of image acquisition was 43 s after the end of the injection) to allow enough time to establish a steady iodine concentration in blood. This time delay of 76 seconds is based on several studies analyzing the time to achieve a steady concentration of iodine in blood after different injection schedules[121,122,123] (**Figure 54**). This group of patients had VNC images.

Table 10. Summary of series created for two patient groups, according to time delay after end of iodine injection

	Time delay after end of injection	120 kVp SECT No iodine	DECT MIX With iodine	DECT VMI	DECT VNC
Group 1 (n = 15)	0 s	Yes	Yes	Yes	No
Group 2 (n = 15)	43 s	Yes	Yes	Yes	Yes

We did not acquire any series at SECT 120 kVp with injected iodine contrast because the increased uncertainty in dose calculations due to iodine had been determined in the preceding literature[118,124,125] and made these images unnecessary. Moreover, an additional series would needlessly increase the imaging dose to the patients.

The dual-spiral DECT studies were acquired with iodinated contrast at 80 kVp and 140 kVp. The MIX series were derived by means of the Siemens Syngo Via v.50 software, which uses an alpha-blending algorithm with $\alpha = 0.3$ (30% low kilovoltage, 70% high). VMIs were created with the Monoenergetic+ algorithm, based on two-material decomposition, and VNC images with the Liver VNC application, based on three-material decomposition.

For the VNC images, we first determined the ability of the software to separate water and iodine by measuring the CT numbers of the VNC images of a water-iodine solution in the interval of 0 mgI/mL to 6 mgI/mLH_2O. We considered the VNC generation acceptable if the CT number of water was 0 ± 4 HU. That value is the reference standard for the value of water given by the manufacturer in a SECT study. We did this analysis to find a possible interval of usability for the VNC algorithm and to know whether the iodine concentrations in the patients fell within that interval.

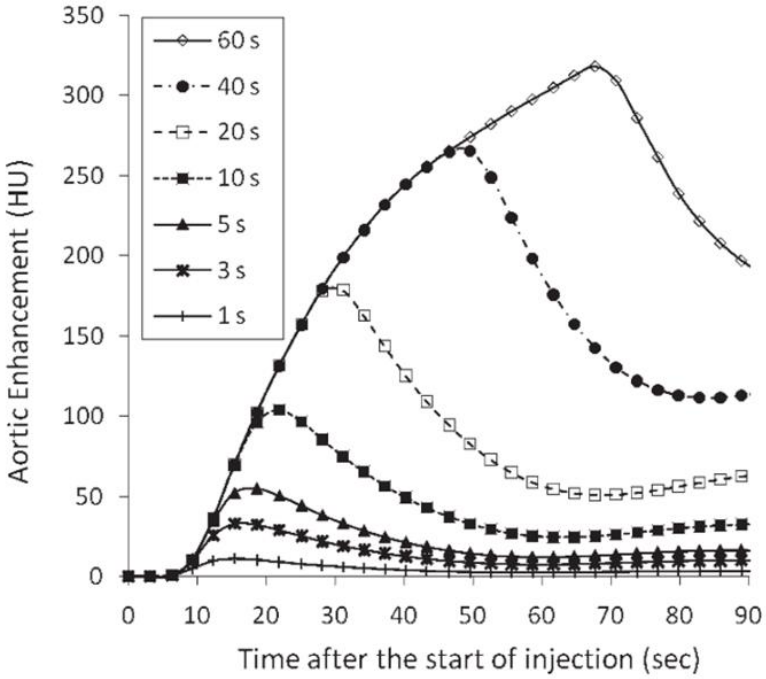

Figure 54. Simulated abdominal aortic enhancement curves based on a hypothetical adult male (30 years old; weight, 70 kg; height, 170 cm) subjected to varying injection durations (1 s, 3 s, 5 s, 10 s, 20 s, 40 s, and 60 s) of contrast medium (350 mg of iodine per mL) injected at 3 mL/sec. Font: Bae et al. 2010[123].

As dose calculations are sensitive to the relationship between electronic density and CT numbers, the planning system requires a calibration curve specific to this relationship for any energy, CT system or type of images used for calculations. VNC images are not equivalent to SECT 120 kVp images, so we considered measuring the specific calibration curve of the VNC images as mandatory. The calibration curve was constructed by means of a Gammex Electron Density Phantom.

We performed two analyses: imaging contrast and dose differences.

4.1.1 Comparison of image contrast

The common delineation procedure with DECT consists of one CT acquisition without iodine at 120 kVp SECT, plus a second one with DECT and iodine. From the DECT study, VMIs are used for delineation, but they cannot be used for dose calculations. At this point, if VNC images are not available, the SECT study is used for planning. However, when VNC images are available, using them for delineation makes no sense

because the virtual removal of iodine results in a decrease in iodine enhancement. It is therefore not necessary to calculate or compare CNR in VNC images.

Calculation of VNC images in a dual-spiral DECT system must be done with care. According to **Figure 54**, iodine concentration in blood changes with time, necessitating a delay of about 76 s between the start of iodine injection and the start of CT acquisition to get a relatively steady concentration. Observing that picture, iodine concentration is lower than the maximum. In chapter 2 we measured CNR in real patients, but injection conditions were selected to maximize iodine concentrations, not calculate radiation dose. Thus, as conditions change, it is necessary to measure CNR with the time delay. The VMI series to assess was that of 45 keV, as the results of our previous study in chapter 2 showed that this energy fulfills the quality requirements and presents the maximum CNR compared to superior energies. If CNR at 45 keV were inferior to SECT 120 kVp or 80 kVp, the advantages of DECT would be cancelled out due to the decrease in iodine caused by the time delay.

4.1.2 Dose differences

For each patient, we planned four 6 MV photon plans to be treated with a Varian Truebeam. Plans were first created on the SECT 120 kVp series. Treatment plans were created to include typical geometries and types of treatments. Those plans were:

1) 2 volumetric modulated arc therapy (VMAT) arcs of 360º, with a collimation difference of 60º.
2) 2 lateral opposite fields with a boost of the same technique.
3) 1 dynamic conformal arc with a boost of the same technique.
4) 5 static fields at 0º, 90º, 135º, 225º and 270º with a 2 lateral opposite fields boosts.

Field geometry can be observed in **Figure 55**.

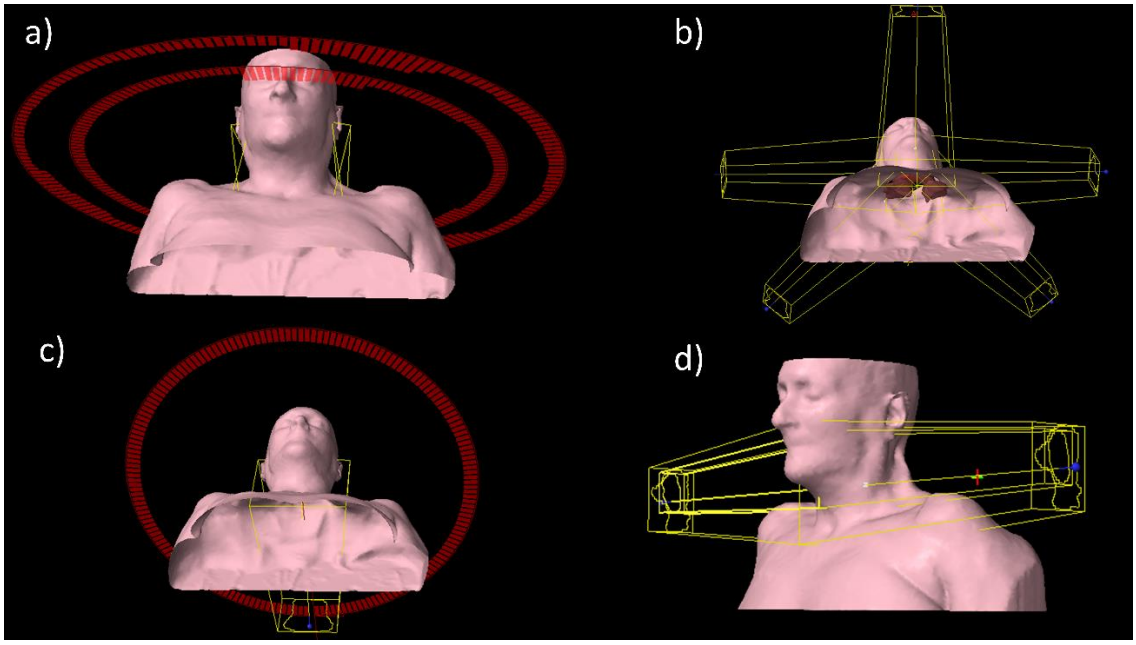

Figure 55. 3D representation of the four plans used in this study. a) RapidArc plan, where multi-leaf collimator (MLC) shape and radiation dose rate vary while accelerator gantry is rotating. b) Five-static plan. c) Conformal arc plan, where MLC moves but the dose rate is fixed. d) Two-static plan.

Planning target volumes and the main organs at risk are shown in **Figure 56**.

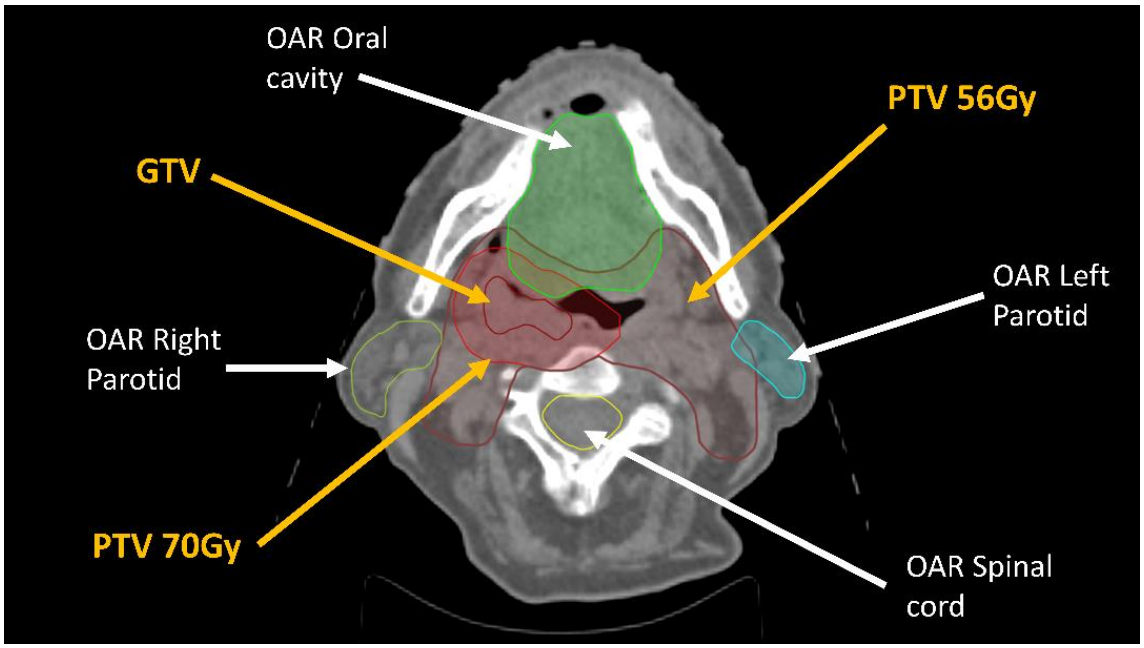

Figure 56. Planning target volume (PTVs) and organs at risk (OARs) in a reference non-contrast SECT image. Author's data.

Plans calculated in the SECT non-iodinated series were taken as reference. The prescribed dose for the tumor was a mean dose of 70 Gy in the planning target volume (PTV) and with the 66.5 Gy (95%) isodose covering at least 98% of the PTV volume. PTVs in laterocervical chains were prescribed a dose of 56 Gy, with 98% of the PTV volume encompassed by the 53.2 Gy isodose (**Figure 57**). Doses to organs at risk (OARs) were those mentioned in section 1.1.7, **Table 2**.

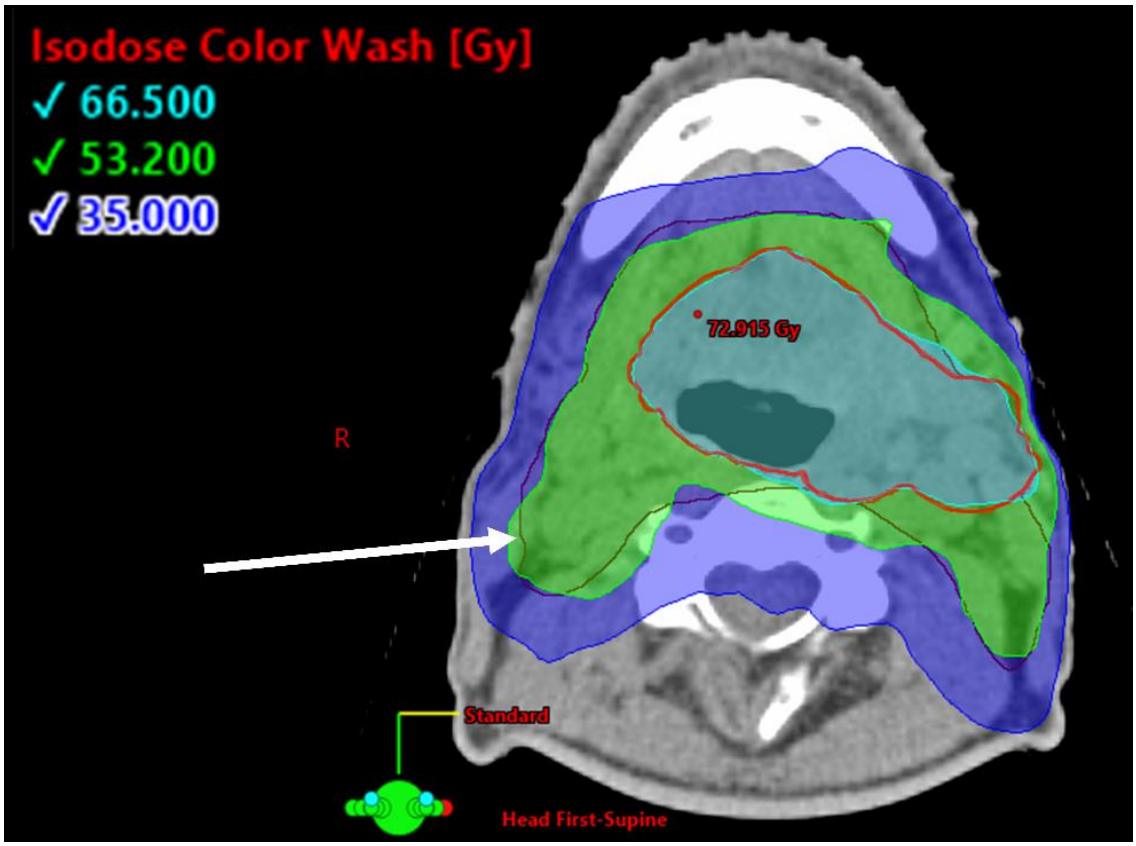

Figure 57. Example of volumetric modulated arc therapy dose distribution. The red line is the tumor PTV. Laterocervical PTV is the volume signaled by the arrow.

All plans were calculated using the Varian Eclipse v.13.6 Treatment Planning system, with the algorithm AAA. After dose calculation on the SECT 120 kVp, plans were copied to the MIX and VNC series. Calculated monitor units were kept the same as in the 120 kVp series, which was the reference. No further normalization was done in the MIX or VNC plans. The calculation matrix was set to $2 \times 2 \times 2$ mm^3. With this value, each point of the matrix encompassed 8 image voxels. This is important for calculations because the resulting electronic density for each matrix point is the average of 8 points, reducing the

possible influence of noise. The calculation matrix for all treatments except stereotactic radiotherapy is set to 2.5 × 2.5 × 2 mm^3 in the planning protocols at Hospital del Mar, resulting in a 12-voxel average per point. In this study, we decided to be more restrictive, intentionally forcing a worse situation because VNC images have more noise than SECT, and we wanted to assess this impact on calculations.

Special care was taken to exactly match the calculation matrix and the anatomy between series: each point of the calculation matrix should correspond as exactly as possible to the same anatomical point of the patient in all series.

Since the CT calibration curve (relationship between electronic density and CT numbers) depends on the image acquisition, we used the same curve for the SECT 120 kVp and the DECT MIX. Our decision was based on the assumption that MIX and 120 kVp are almost equivalent. In our study, SECT images did not have iodine contrast, but MIX did. For the VNC series, we measured a specific calibration curve on a 1467 Gammex Electron Density Phantom (**Figure 58**), which is shown in the Results.

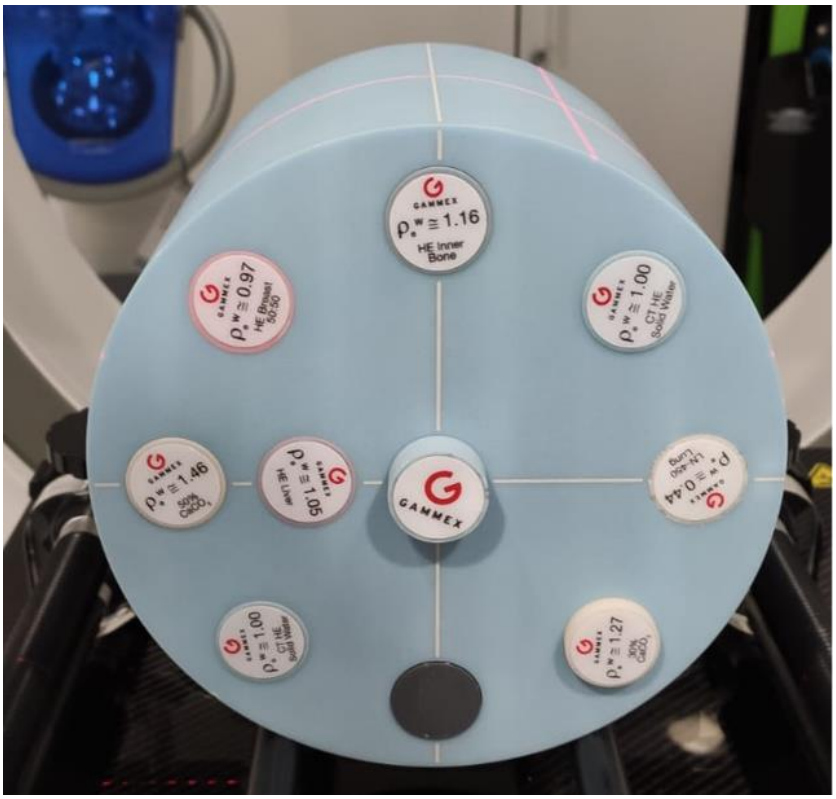

Figure 58. Gammex phantom for electronic density calibration. Each insert is made of a different material with known electronic density. Author's image.

As in clinical practice, we started to compare RT plans using dose-volume histograms. When analyzing plans one by one, these did not show relevant differences between series (**Figure 59**). Moreover, dose-volume histograms miss geographical information on dose differences, so we preferred to use a point-to-point comparison. This way, any observed difference could be exactly located on the patient's anatomy.

We performed two different analyses: a) a 3D Gamma analysis to check dose distributions, and b) an analysis of point-to-point differences. Both were calculated by means of Visual Basic macros in a Microsoft Excel worksheet. Since dose distributions are exported by the planning system in digital imaging and communication in medicine (DICOM) RT format, we used the freeware Image J to convert them to text files and import them to Microsoft Excel.

We divided the calculated points into three regions: high dose (at least 95% of the total dose), medium dose (50% to 94%), and low dose (less than 50%). This classification of points was arbitrary but performed as it was for different reasons:

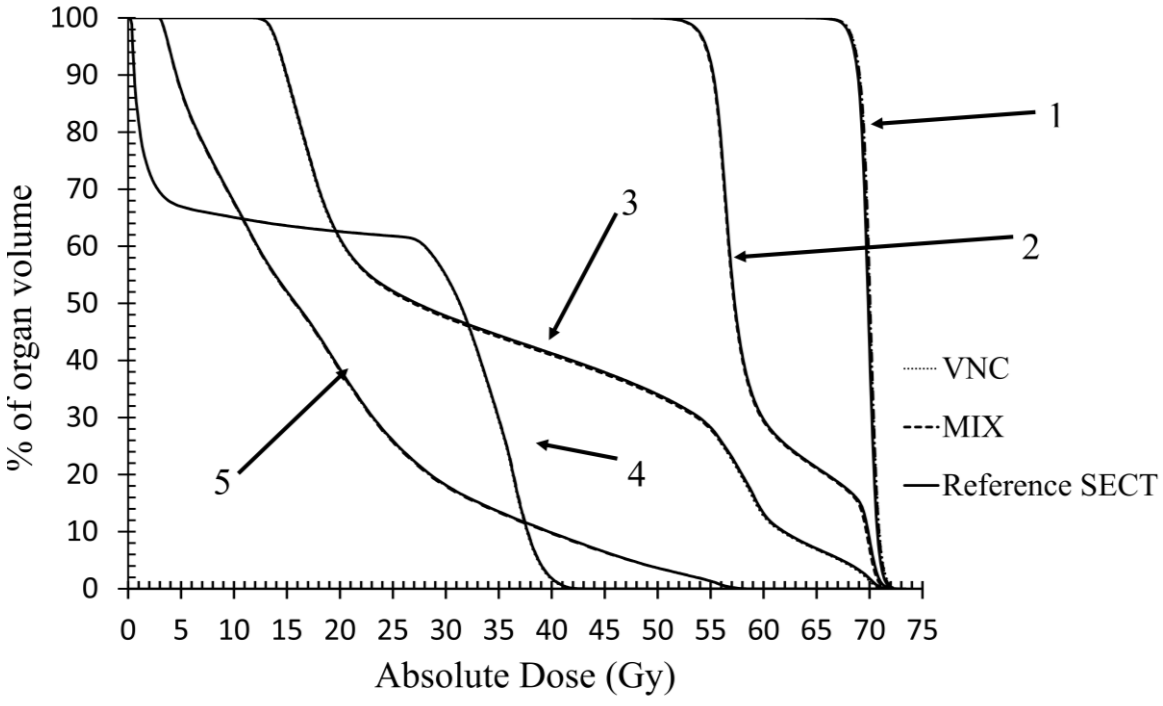

Figure 59. Example of comparison by dose-volume histograms. There are no remarkable differences between series. Numbered organs are: 1) planning target volume (PTV) 70 Gy, 2) PTV 56 Gy, 3) oral cavity, 4) spinal cord, and 5) left parotid. The dose-volume histogram corresponds to the RapidArc plan of one patient. Similar results were found in all patients.

- The high-dose region encompasses the tumor PTV. Plans are intended to achieve a dose distribution as homogeneous as possible. Here an active tumor is present, and doses must be kept between 95% and 107% of the total dose if possible. Thus, this is a region of quasi-homogeneous doses.
- Medium-dose regions, between 50% and 94% of total dose, include the 56 Gy PTV and organs at risk in high-dose areas. Here, dosimetrists try to keep PTV doses as homogeneous as possible while keeping OAR doses under their tolerance limits, so high gradients of dose in contact to OARs are expected.
- Low-dose regions are outside the PTVs, where dose distribution is not intended to be homogeneous but rather as low as possible in OARs.

a) Gamma analysis

2D Gamma analysis is commonly used in radiotherapy to check the similarity between two (or more) plans. It is defined in a 3D space where spatial coordinates occupy the horizontal plane (X,Y), and the point dose the vertical Z. Any point *P* in the reference distribution will be represented by its coordinates (X_{ref}, Y_{ref}, D_{ref}) (**Figure. 60**). For the Gamma analysis, a distance to agreement (DTA) in mm and a maximum dose difference δ must be defined. These values define an ellipsoid around *P* where point P_c (X_c, Y_c, D_c) of the dose distribution to compare must exist. The relative position of P_c is defined by the vector:

$$\vec{r} = (r_x, r_y, \Delta d)$$

where

$$r_x = x_c - x_{ref}\,;\; r_y = y_c - y\,;\; \Delta d = d_c - d_{ref}$$

The Gamma value for point P_c relative to point *P* is calculated as:

$$\Gamma(P_c, P) = \frac{|\Delta d|}{\delta} \cdot \left(1 - \frac{|r|^2}{DTA^2}\right)^{-1/2}$$

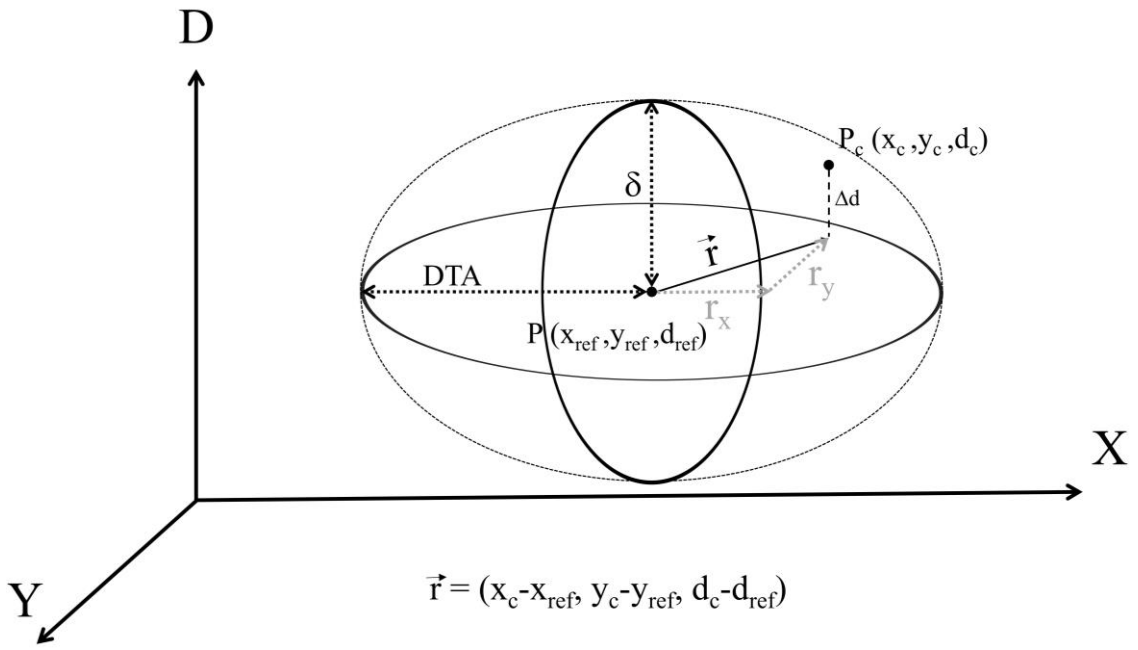

Figure 60. Definitions in the Gamma analysis. In this study, point *P* corresponds to the reference SECT 120 kVp series without iodinated contrast. Points P_c correspond to the dose distributions to compare.

We can compute Gamma of point *P* by calculating $\Gamma(P_c, P)$ for all the points P_c of the compared distribution as follows:

$$\Gamma(P) = \min\{\Gamma(P_c, P)\}\ \forall P_c$$

The meaning of a value $\Gamma(P) \leq 1$ is that a point P_c exists in the compared dose distribution that lays inside the ellipsoid defined by the Gamma tolerance $\Gamma(\delta, \mathrm{DTA})$ for point *P*. In this case, evaluation for point *P* is positive. We can define a variable p_i with two values 0 and 1 as follows:

$$p_i = 1\ if\ \Gamma(P) \leq 1$$

$$p_i = 0 \text{ in all other cases}$$

Finally, it is possible to summarize the Gamma analysis as a single value, as the percentage of passing points. If *N* is the number of points in the reference distribution,

$$\gamma(\delta, \mathrm{DTA}) = (100\%) \cdot \frac{1}{N} \cdot \sum_{i=1}^{N} p_i$$

2D Gamma analysis can be extended to 3D with the addition of the Z (cranio-caudal) coordinate. In this study, we used the 3D Gamma analysis. Thus, for each point in the

120 kVp dose distribution matrix, 27 points were evaluated in the distributions in MIX and VNC, as shown in **Figure 61**.

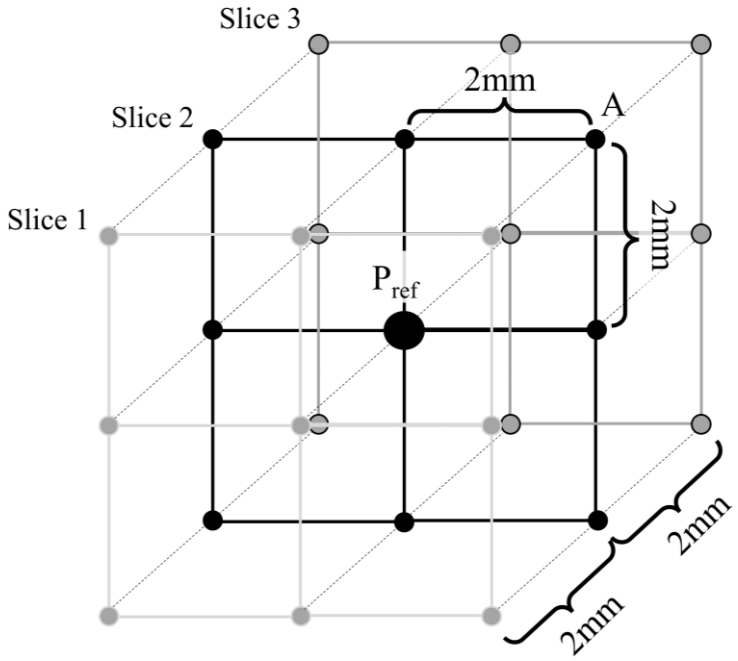

Figure 61. Calculation matrix for a point P_{ref}. Slices 1 and 3 correspond to the previous and the following slices in the image series. Only points located in the centers of the squares are 2 mm from P_{ref}. Points at the edges of the cube are over 2 mm away. In those directions, dose has been linearly interpolated to calculate at 2 mm.

Comparisons in radiotherapy are usually done with a Gamma analysis of Γ(2%, 2 mm)[104,105]. Nevertheless, in this study we selected a stricter criterion with Γ(1%, 2 mm). We compared the relative number of points with $\Gamma \leq 1$ for each dose distribution and set 95% as the minimum number of points with $\Gamma \leq 1$.

b) Point-to-point differences

Since Gamma analysis compares each evaluated point in the dose distribution to the same point and the surrounding in the reference dose distribution, it seeks the best agreement for each point. We did an additional point-by-point study by comparing the dose of each point in the analyzed series to the dose at a point located at the same coordinates in the reference images. Doing so, we did not seek the best agreement but the exact difference in the same geometrical point of the patient.

The difference was calculated in relation to the total dose, not the local dose. Thus, a 1% difference corresponded to 0.7 Gy regardless of the local dose:

$$\Delta D\ (P) = (100\%)\ \frac{D(P) - D(P_{\mathrm{ref}})}{70\ \mathrm{Gy}}$$

Where *D(P)* is the dose at point *P* in the distribution being compared, $D(P_{\mathrm{ref}})$ the dose at the same point in the reference (120 kVp without iodine) series, and 70 Gy the total dose of the plan.

We calculated the distribution of Δ*D* for all points and series, their distributions, average values, and SDs for comparisons.

4.2 Results

4.2.1 Calibration curves

In the first step we determined the iodine concentration interval where the VNC algorithm was able to successfully remove iodine from enhanced images. To do this, in an initial step we measured the linearity of the system to an increasing concentration of iodine (**Figure 62**).

A VNC algorithm creates two sets of images: one is the VNC itself, with no iodine present, and the second is an iodine map, presenting only the local iodine concentrations. A VNC image of a mixture of iodine and pure water should keep CT numbers closer to zero while the iodine map should be a linear distribution proportional to iodine concentration. So, in an ideal VNC algorithm, that is, a pure water-iodine solution like the one shown in **Figure 62**, the lines for CT numbers in iodine and the total should match, and the water line should be zero in all concentration ranges. The larger the separation between iodine and the total, the less accurate the algorithm.

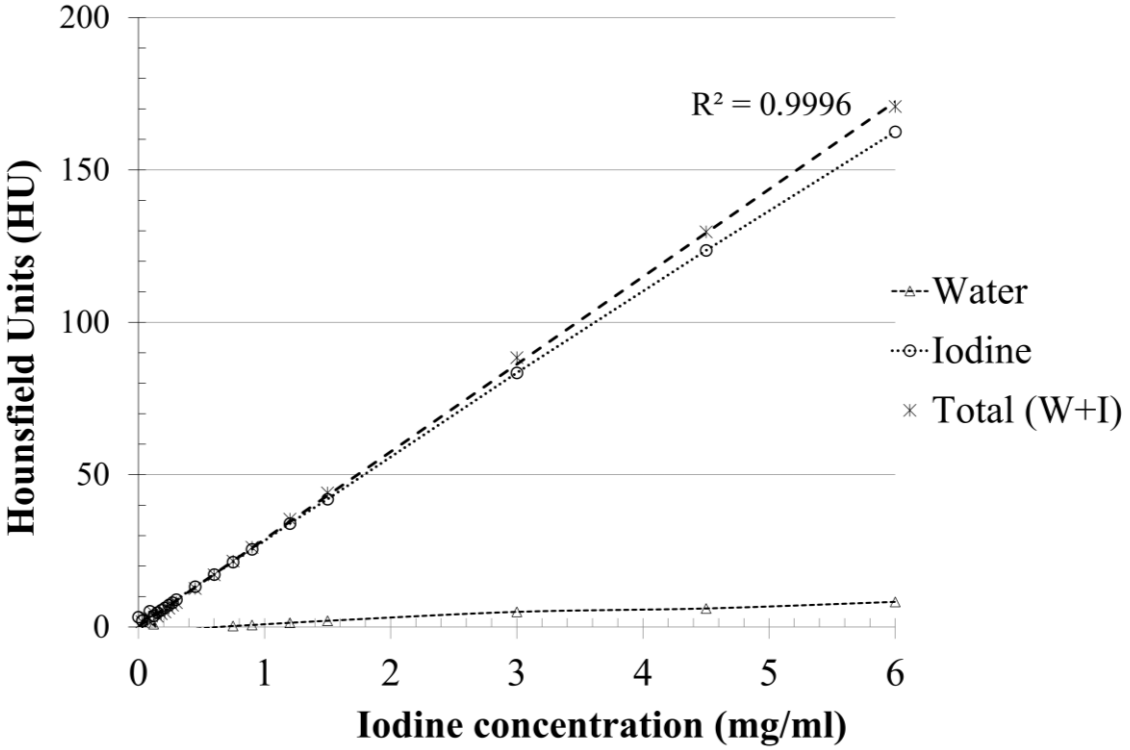

Figure 62. Representation of CT numbers in an iodine-water solution. The linearity of the system is represented by the linear correlation of the total (W+I) plot. The correlation coefficient is represented in the graphic. The iodine curve represents the CT numbers due to iodine according to the VNC algorithm. The separation between total and iodine plots correspond to water alone after iodine virtual extraction.

Thus, according to our result, VNC loses accuracy as iodine concentration increases. To determine the interval where VNC is correct, we considered that the water CT numbers must be in the interval of uncertainty of the CT itself, i.e., 0 ± 4 HU.

Figure 63 presents the water part of the VNC images as a function of iodine concentration.

Values remained under 4 HU until reaching an iodine concentration of about 3 mg/mL. At this value, according to **Figure 62**, iodine increased CT numbers by 84 HU (SD 6) with respect to the nominal 0 HU of water. Values near a concentration of 0.6 mg/mL present a mean value of zero in **Figure 62**. Below that concentration, CT numbers adopt negative values until reaching a concentration of 0.1 mg/mL. At such low concentrations, values present more variations that converge to a mean value of −2 HU for pure water. This result suggests that the Liver VNC algorithm subtracts a small contribution of photoelectric effect to pure water, giving a result of −2 HU instead of 0 HU.

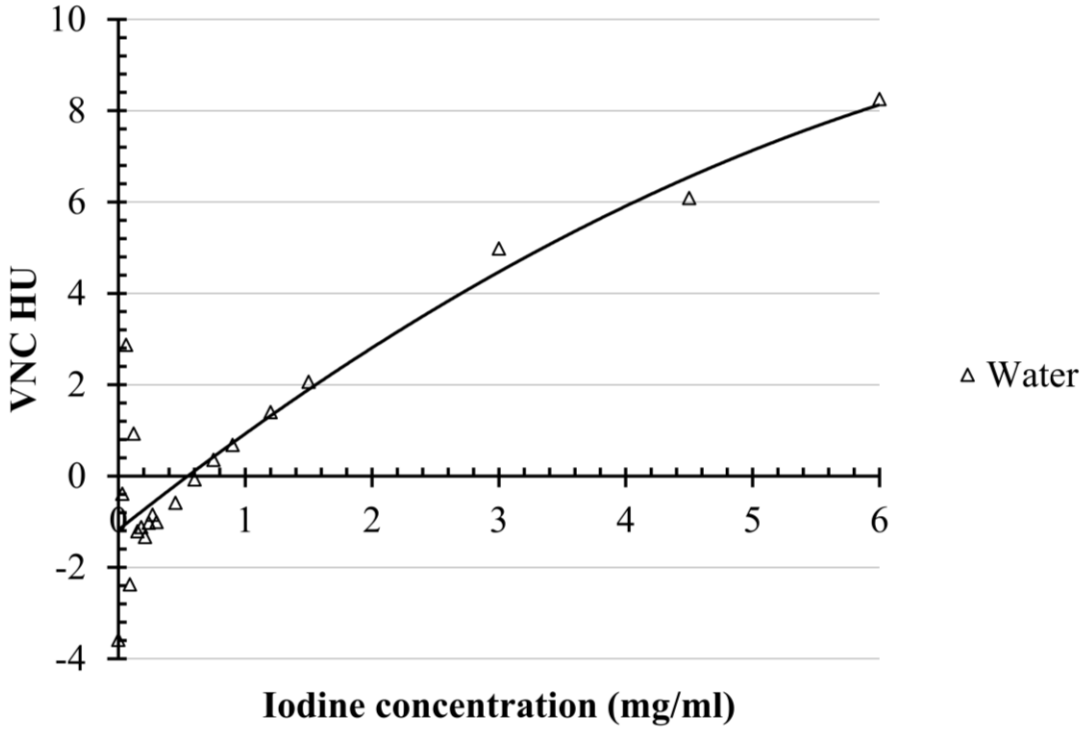

Figure 63. Water part of **Figure 62**. Sensitivity of the algorithm to water is not linear. As shown, the CT numbers of water have negative values under 0.6 mg/mL of iodine.

Figure 64 shows the calibration curve of VNC images to be used in dose calculations by the planning system. As expected, it resulted in a straight line with a correlation factor of 0.998. The meaning of this result is that the virtual subtraction of iodine is based on the subtraction of any contribution from the photoelectric effect, leaving only Compton scatter, which is proportional to electronic density. **Figure 64** shows the VNC calibration curve compared to the SECT 120 kVp. Differences are important for materials with CT numbers superior to water because of the contribution of their photoelectric effect. This justifies the need for a specific calibration curve for VNC images in the planning system.

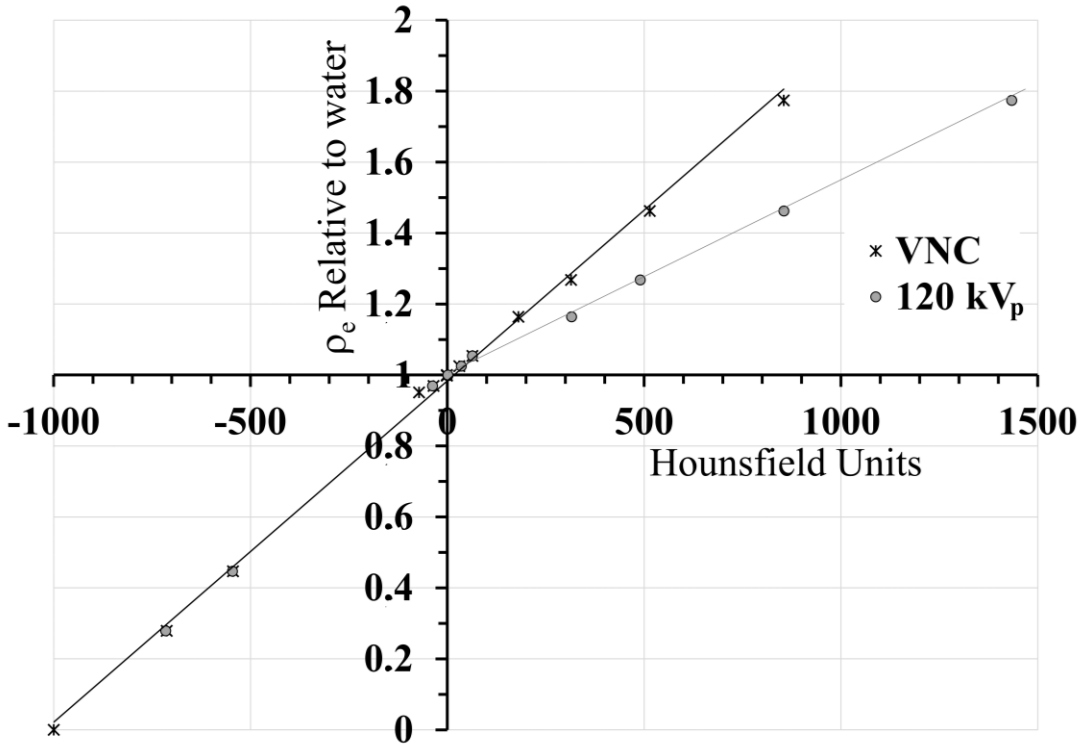

Figure 64. Measured calibration curve for VNC images. For tissues with negative CT numbers, there are no differences between curves. However, for positive values the measured virtual non-contrast (VNC) curve must be used in the planning system because of large differences.

4.2.2 Comparison of image contrast

Results of the comparison of image contrast are presented in **Table 11**. Both groups of patients showed a similar blood-to-muscle CNR in the iodine-enhanced MIX images (group 1, 11 [SD 3.7] and group 2, 12 [SD 3.8]). Nevertheless, the 45 keV VMI series had CNR values of clearly superior to the MIX series but equal in both groups. Group 2 VMIs presented a higher SD.

The thyroid gland showed equivalent behavior: the increase in CT numbers due to iodine with respect to the non-iodinated SECT was similar in both groups: 75.5 HU for group 1 and 74.7 HU for group 2.

Applying the formula for CNR considering muscle as reference material for noise, in the same way as we did in point 2.2.5, the observed results in terms of CNR are lower than with air as background, but VMIs do still have a higher CNR than the MIX series in both groups.

Those results can be referenced to the MIX series of group 1 (**Table 12**) as we did in point 2.3.5 (**Table 5** and **Figure 45**). This enables a comparison of the potential loss of CNR in the second group versus the first. Although the characteristics and waiting time of the acquisitions were different, the relative CNR of VMI was similar with air as background and equal to muscle. That result suggests that both groups are at points with a similar iodine concentration as in **Figure 54**, but the two groups fall at each side of the maximum iodine concentration for a single injection of iodine, as shown in **Figure 65**. However, the exact shape of the curve and the real concentrations should be addressed in a specific study and are beyond the scope of the present work.

Table 11.Contrast results (standard deviations). CNR: contrast-to-noise ratio; HU: Hounsfield units; SD: standard deviation; SECT: single-energy computed tomography; VMI: virtual monoenergetic image.

	HU (SD)						
	Blood	**Muscle**	**Thyroid**	**SD Air**	**SD Muscle**	**CNR Air**	**CNR Muscle**
Groups 1 and 2							
120 kVp SECT	41.5 (6.5)	51.9 (8.2)	79.7 (10.3)	4.5	11.1	2.3 (1.9)	0.2 (0.15)
Group 1							
MIX	154.5 (23.4)	63.6 (6.1)	154.2 (11.9)	2.9	8.6	32 (10.9)	11 (3.7)
45 keV VMI	365.3 (65.5)	84 (9.9)	342.1 (50.4)	2.8	13.5	100 (28)	22 (7)
Group 2							
MIX	166.5 (28.3)	62.9 (7.1)	154.4 (19.1)	3.5	9	30 (8.4)	12 (3.8)
45 keV VMI	381.4 (79.3)	83.7 (13.2)	341.9 (58.8)	3.5	14.2	88 (24.2)	22 (6.3)

To examine the previous result more closely, we compared the CT numbers of thyroid in the mixed series with both injection conditions. The results were 154 HU (SD 12) for the conditions used in **Table 6**, and 155 HU (SD 15) for the VNC conditions. Those similar values seem to be in line with the equivalence of CNR.

Table 12. Contrast-to-noise ratio between VMI 45 keV in groups 1 and 2 and MIX of group 1

	Relative to group 1 MIX	
	CNR Air	**CNR Muscle**
Group 1	3.1	2
Group 2	2.8	2

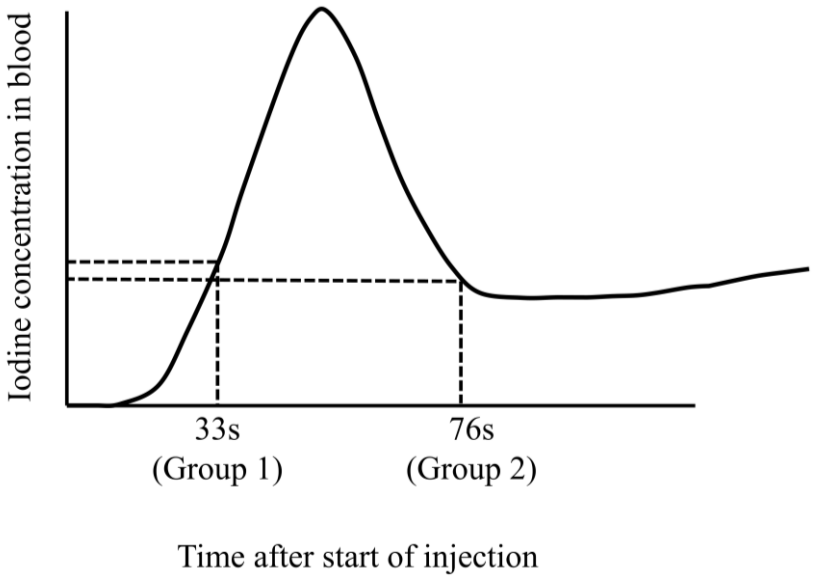

Figure 65. Qualitative curve of iodine concentration in blood in relation to time after the start of injection. Our iodine enhancement suggests that both groups have similar concentrations and are at each side of the maximum.

4.2.3 Dose differences

a) Gamma analysis

RT plans are optimized by dosimetrists to show a dose distribution with low variability inside the PTV. In a perfect situation, all points inside the PTV would have the same dose.

Therefore, in the high-dose region the percentage of points with Γ(1%, 2 mm) ≤ 1 should be about 100% at any point in the PTV.

Our results are shown in **Tables 13** and **14**. In high-dose regions, the number of points with Γ(1%, 2 mm) ≤ 1 was close to 100% in both groups and DECT series.

Table 13. Results of the Gamma analysis passing rate (standard deviation)

	Γ ≤ 1 (%)		
Series	**High-dose regions (D ≥ 95%)**	**Medium-dose regions (95% > D ≥ 50%)**	**Low-dose regions (D < 50%)**
SECT 120 kVp no iodine	Reference	Reference	Reference
MIX Group 1	99.6 (1.0)	97.4 (3.2)	96.3 (3.3)
MIX Group 2	99.9 (0.1)	98.9 (1.8)	98.3 (2.0)
VNC (Group 2)	99.9 (0.3)	98.8 (1.1)	98.2 (1.4)

On analyzing the high-dose areas plan by plan (**Table 14**), we likewise found no remarkable differences. The Gamma passing rate was near 100% for all plans. Thus, all distributions were almost equivalent in the high-dose regions.

The Γ passing rate decreased in the medium- and low-dose regions. The worst results were in patients from group 1, but differences were acceptable (Γ > 95%) in all cases but one. Plan 2 (two lateral static fields) did not pass the Gamma analysis in that group.

The results for the dose distributions calculated on MIX and VNC series in group 2 were almost equivalent and really closer to the reference SECT 120 kVp without iodine.

Table 14. Results of the Gamma analysis plan by plan. Standard deviations in parentheses

		Γ ≤1 (%)		
		High-dose regions (D ≥ 95%)	**Medium-dose regions (95% > D ≥ 50%)**	**Low-dose regions (D < 50%)**
MIX group 1	Plan 1	99.9 (0.4)	98.2 (2.4)	97.1 (3.1)
	Plan 2	99.7 (0.5)	96.1 (3.8)	94.7 (5.4)
	Plan 3	99.3 (1.8)	97.6 (3.0)	97.0 (2.0)
	Plan 4	99.6 (0.9)	97.9 (2.5)	96.3 (3.3)
MIX group 2	Plan 1	100.0 (0.1)	99.4 (0.4)	99.1 (0.3)
	Plan 2	100.0 (0.0)	98.1 (1.1)	97.2 (1.6)
	Plan 3	100.0 (0.1)	99.3 (0.4)	98.8 (0.4)
	Plan 4	99.9 (0.3)	98.8 (1.1)	98.2 (1.4)
VNC (group 2)	Plan 1	100.0 (0.1)	99.4 (0.5)	99.1 (0.4)
	Plan 2	99.8 (0.5)	97.8 (1.2)	96.9 (1.6)
	Plan 3	100.0 (0.1)	99.3 (0.5)	98.7 (0.4)
	Plan 4	99.9 (0.3)	98.8 (1.1)	98.1 (1.4)

b) Point dose differences

Results of the point-to-point analysis are presented in **Table 15**. In the high-dose regions, mean dose differences were less than 0.3% for all distributions, in line with the results of the Gamma analysis. Calculations on VNC images gave the best results and were equivalent to the non-contrast series in those regions. Moreover, calculations on MIX images were equivalent in both groups of patients regardless of the pattern of iodine injection, and their uncertainty with respect to the non-contrast series was as low as 0.2% to 0.3%.

As average values may cancel out negative and positive differences, we calculated differences regardless of the sign. Thus, this is an approach of the most common deviation. When considering differences regardless of the sign in the high-dose regions, results showed a slight worsening: Group 1 MIX 0.79% (SD 0.51%), Group 2 MIX 0.34% (SD 0.10%), and VNC 0.22% (SD 0.10%). Again, VNC series showed the best agreement, at less than 0.2%.

Table 15. Results of point-to-point differences with respect to the non-contrast 120 kVp series

	High-dose region (D ≥ 95%)		**Medium-dose region (95% > D ≥ 50%)**		**Low-dose region (D < 50%)**	
	Dose diff (%)	**Dose diff. No sign (%)**	**Dose diff (%)**	**Dose diff. No sign (%)**	**Dose diff (%)**	**Dose diff. No sign (%)**
Group 1 MIX	−0.28 (0.33)	0.79 (0.51)	−0.45 (0.45)	**1.95** (1.16)	−0.38 (0.26)	**2.25** (1.26)
Group 2 MIX	−0.23 (0.10)	0.34 (0.10)	−0.16 (0.10)	0.50 (0.32)	−0.13 (0.08)	0.50 (0.32)
Group 2 VNC	−0.05 (0.08)	0.22 (0.10)	−0.02 (0.07)	0.41 (0.19)	−0.03 (0.03)	0.43 (0.22)

Note: In bold, results over 1%.

In the medium- and low-dose regions, mean dose differences were negligible for the VNC series. For the group 2 MIX, under VNC injection conditions, differences were also very small, always under 0.5% even when sign was not considered. However, the Group 1 MIX series, which had different injection conditions to keep CNR as high as possible, showed differences of about 2% in mean when sign was not considered.

Summarizing, in the high-dose regions all series produced similar results, with VNC slightly better. In the medium- and low-dose regions, calculations on Group 1 MIX images were not so accurate and yielded deviations near 2% (1.4 Gy), while VNC injection conditions improved calculations and narrowed the uncertainty interval to 0.5%.

4.3 Discussion

There are four ways to deal with the issues related to injecting IV iodinated contrast for delineation of target volumes and organs at risk:

1) Acquiring a unique series at single-energy 120 kVp with iodinated contrast and doing calculations on it. As we have shown, this does not take full advantage of all the possibilities of iodinated contrast, because CNR is not high at 120 kVp. On the positive side, it is easy to control the radiation dose due to imaging, but as we will discuss below, there are some concerns about RT doses.
2) Acquiring a single-energy 120 kVp series without iodine for calculations, plus another at a lower kilovoltage with iodine for delineation. Again, this study shows that such an approach does not take advantage of the increased CNR obtained with the VMIs or fix the problems related to image registration, and the total imaging dose is higher than that of a unique 120 kVp.
3) Acquiring a single-energy 120 kVp CT without iodine for calculations plus a DECT study with it for delineation. Although this approach improves tumor delineation, it increases the imaging radiation dose and does not solve the registration uncertainties.
4) Acquiring a dual-energy study with iodinated contrast only. In this case VMIs are used to take advantage of the iodine, and VNC or MIX series are used for calculations. The radiation dose in this approach can be the same as that of a single-energy 120 kVp acquisition. The following section discusses this approach.

As stated in the literature, VMIs do not fulfill the requirements for dose calculations in radiotherapy[124,126]. However, VNC series have been proposed as a good approach for RT dosimetry[73,74]. There is plenty of literature about the quality of VNC images and their limitations. Many authors have found that these reconstructions can be noisier[127,128], even though some articles argue that this increase does not negatively affect their utility[128,129]. Moreover, there are some known issues about their craniocaudal homogeneity and uncertainties due to different iodine concentrations[120].

Noise is an important issue in CT imaging. Nevertheless, RT dose calculations are not as sensitive to it because of the limited resolution of the calculation matrix. As explained in point 4.1.2, each point of the dose calculation matrix has an assigned electronic density, calculated by averaging the electronic densities of several points. This limits the impact

and importance of noise. Our results in dose calculations on VNC images, especially those related to point-to-point differences, support the idea that the increased noise in these images does not have a remarkable impact on dose calculations.

In our study, we did not analyze the imaging quality of the VNC series because they are not used for delineation. Therefore, resolution, contrast, and noise are not relevant here. We did an end-to-end analysis, meaning that we compared only the planning results of calculations done on VNC for Hospital del Mar's specific acquisition protocol.

Although VNC characteristics for most RT calculations are well established, published studies cover all types of dual-energy CT except dual-spiral dual-energy. That omission necessitates an analysis of the characteristics of that type of DECT. In this research we studied the Siemens solution for VNC with dual-spiral DECT, in particular the Liver VNC algorithm, and its capability to correctly remove iodine from enhanced images.

We observed that the predicted CT numbers of water using the VNC algorithm were within the acceptance interval of ± 4 HU up to a concentration of 3 mgI/mL. Below 0.6 mgI/mL, CT numbers were negative, and the value for 0 mgI/mL (pure water) was −3.6 HU. This result suggests that at very low concentrations the algorithm overestimates iodine presence, and there is a lower limit for correct iodine removal. This result is in accordance with the observations by Li et al.[130] and Jacobsen et al.[131] However, because the measured values were below the tolerance limits for water, we considered that the VNC algorithm had acceptably removed iodine up to a concentration of 3 mgI/mL in our phantom study. At that concentration, iodine increased CT numbers by 84 HU with respect to pure water. At higher concentrations, the three-material decomposition model was not able to correctly separate iodine and water. In our patients, the increase in CT numbers for the muscle and the thyroid compared to non-iodinated images were lower than the upper limit of 84 HU. However, blood surpassed that limit by 40 HU. Even though the maximum value for the iodine uptake was exceeded, the results did not seem to be influenced. Calculation points located inside the great vessels did not show worse results than others located outside them. Thus, the calculation algorithm seems to be robust to excesses in the VNC upper limit in small structures, possibly because their influence on electronic densities in the photon beam path is small.

One important question was whether the special characteristics of the iodine injection and acquisition to derive dual-spiral VNC, which meant a waiting time of 76 s, would affect the Contrast to Noise Ratio of VMIs. If VMIs had a lower CNR than the classical Single-energy CT images at 120 kVp, their utility would be called into question. Our reference was the iodine injection and imaging protocol used in our department before the acquisition of the Liver VNC application. We did not acquire CT images at SECT 120 kVp with iodinated contrast. Thus, we compared VMI series in VNC conditions to the dual-energy VMI and MIX series in the reference protocol. Thus, we assumed that MIX images were very similar to SECT 120 kVp. This assumption was motivated by the fact that an additional SECT scan at 120 kVp would have needlessly increased the imaging dose to the patients.

On comparing **Tables 5** and **11**, 45keV Virtual Monoenergetic Images show a higher CNR than MIX and SECT 80 kVp images in both groups of patients. As MIX are almost equivalent to SECT 120 kVp, we can affirm that VMI 45 keV of dual-spiral Dual Energy are superior in terms of CNR to SECT studies under VNC and non-VNC conditions, and could be better for tumor delineation.

The contrast enhancement measured in terms of CNR, with muscle as the background tissue, was about twice as high in the VMI 45 keV series as in the MIX images and about 20 times the non-contrast CNR. Even though this result was expected considering previous studies referenced by Kruis et al.[132], it is of crucial importance for the dual-spiral DECT because VMIs can compensate for a potential decrease in iodine concentration under VNC conditions caused by the delay after injection. Nevertheless, when looking at our results, we found that the protocol used before having VNC resulted in an iodine concentration similar to it. This result was unexpected because the early protocol was introduced in the department without a thorough study of iodine concentration dependence over time. If the time delay in the first protocol had been long enough to achieve the maximum concentration of iodine in blood, the results of the comparison between VMIs might have been different.

As described by Miller et al.[133], image quality is affected by the three-material decomposition model used in this work, Liver VNC (Siemens Healthineers), although Toepker et al.[134] reported that these limitations seem to have a very small influence on

plan calculations. However, neither of these studies was done on dual-spiral DECT images.

Regarding the uncertainty in dose calculations on enhanced images, our results are in line with previous studies done in dual-source, fast kV-switching, and dual-layer DECT. In general, for the head and neck regions, some authors have observed that dose deviations between iodine-enhanced and non-enhanced images are small[125], generally less than 0.5%, and they have a low impact on dose-volume histograms[5]. Our results support those conclusions in dual-spiral DECT. Indeed, we found a Gamma pass rate over 95% in all series. Liugang et al.[135] published similar results for a dual-source DECT system.

Calculated doses were lower in the enhanced images when keeping monitor units fixed on the non-contrast values. Authors like Rankine et al.[6] warn that planning in contrast-enhanced images can lead to an overdose near 2% in some cases. Our calculations on MIX images were not in line with that result when considering dose at the tumor PTVs, because we observed an overdosage of about 0.3% when normalizing plans to the mean PTV dose. What we found was an increase in dose uncertainty in the medium- and low-dose regions of about 2%.

Finally, in all dose regions, VNC images showed the lowest mean difference, −0.05%, standing at 0.2% when sign was not considered. This result means that VNC images from dual-spiral DECT do not increase the calculation uncertainty of monitor units in RT planning in the head and neck areas relative to real non-contrast images. In fact, they show an almost exact dose matching. Yamada et al. reported similar results in a dual-source DECT system[74].

When analyzing the areas outside the PTV, in the medium- and low-dose regions, differences increase as dose decreases. As our study only measures differences related to the total dose of 70 Gy at each point, a 1% difference translates to a difference of 0.7 Gy at the studied point. We did not find relevant differences between medium- and low-dose regions.

On comparing the results between MIX series of both protocols, we found that the MIX in VNC conditions had better accuracy in the medium- and low-dose regions. This result can be explained by the different injection and acquisition protocols. MIX series acquired just after iodine injection suffer from non-steady iodine concentration, as shown in

Figure 54. In fact, acquisition takes place when iodine concentration is quickly accelerating. This situation causes a greater difference in iodine uptake between the high- and low-kilovoltage acquisitions than under VNC conditions.

A thorough examination of images indicated that the points with differences over 1% were related to registration uncertainties due to motion artifacts, especially near the patient surface (**Figure 66**).

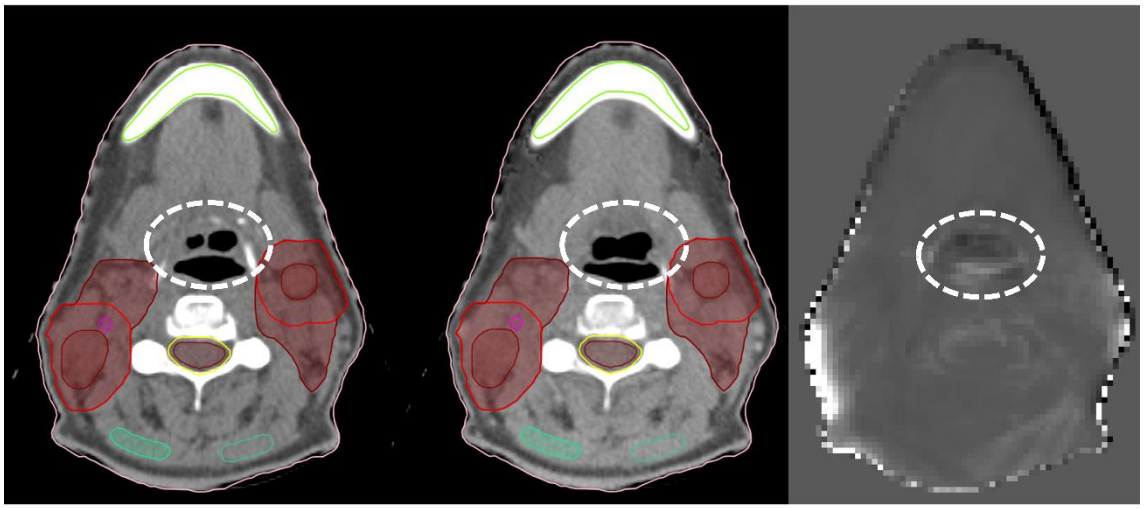

Figure 66. Results on a slice. Image on the right corresponds to the dose difference in a volumetric modulated arc therapy plan. White and black pixels are the minimum and maximum differences, respectively. The major uncertainties are at the patient skin, due to motion artifacts, and in the dotted area, where swallowing causes a registration error.

Summarizing, the literature holds that RT dose calculations can be done on iodine-enhanced images with a small increase in uncertainty. All differences with non-contrast calculations are acceptable according to RT clinical practice. Nevertheless, our study found that dual-spiral DECT can reduce those uncertainties to almost negligible levels by means of VNC images. As long as a time delay of at least 76 s from the beginning of the injection to the start of DECT acquisition is respected, dose calculations on VNC images derived from a dual-spiral DECT scan yield the same results as other types of DECT.

However, the Liver VNC computation algorithm is not a freeware solution. Thus, departments where VNC is not available have only the two classical approaches for the iodine problem: 1) acquiring two series, with and without iodine, or 2) calculating on

contrast images. However, there may be an alternative to the latter option: as VMIs increase the CNR, their use may allow a decrease in the quantity of iodine injected into the patient. Several authors[136-138] have proposed this idea, especially in patients with impaired kidney function. The potential improvement in the accuracy of dose calculations on MIX images in a low-contrast concentration environment has not been studied yet.

4.4 Conclusions

1) Virtual non-contrast (VNC) images obtained with a dual-spiral CT system are more accurate in plan dose calculations than single kilovoltage series when iodine enhancement is used.
2) A waiting time of 76 s is necessary to stabilize iodine concentration in blood and allow accurate calculations with dual-spiral virtual non-contrast images.
3) When VNC is not available, alpha-blended DECT images with a time delay also yield acceptable results, which are better than those without a time delay.
4) Although a time delay is introduced, virtual monoenergetic images have a higher contrast-to-noise ratio than single-energy 120 kVp and 80 kVp images.
5) Dual-spiral DECT VNC images have the same results in dose calculations as the other types of DECT.

5. Final conclusions and Future Work

5. Final conclusions and Future Work

5.1 Final conclusions

In radiotherapy of the head and neck, the results of the three studies presented show the following.

1) Dual-spiral, dual-energy CT (DECT) is a useful tool for delineating tumors and organs at risk in radiotherapy because:
    a. it allows the creation of good-quality virtual monoenergetic image (VMI) series that meet CT quality standards;
    b. VMIs have a high contrast-to-noise ratio (CNR) when iodine is injected;
    c. in the optimal range of 45 keV to 55 keV, VMIs are clearly superior to single-energy CT (SECT) 80 kVp and 120 kVp in terms of CNR;
    d. interobserver variability does not show differences between dual-spiral DECT and SECT.

2) Dual-spiral DECT is useful in planning and dose calculations:
    a. virtual non-contrast (VNC) series show better accuracy in calculations than SECT images with iodine enhancement;
    b. when VNC is not available, the use of MIX images brings better results than SECT;
    c. a waiting time of 76 s is necessary to stabilize iodine. VMIs with dual-spiral DECT under this condition have a higher CNR than SECT images at 120 kVp and 80 kVp.

All the previous conclusions can be summarized as follows:

Under certain conditions, dual-spiral DECT shows similar results in image enhancement and dose calculations as the other types of DECT currently in use.

5.2 Future work

Our study has raised new questions about dual-spiral DECT that need to be addressed in future assays.

1) The influence of different acquisition protocols and iodine injection patterns must be studied to determine the generalizability of our results under other conditions.
2) The question of a reduction in iodine injection and its impact on the calculations on iodine-enhanced images is still unclear. New studies should determine if this strategy could improve accuracy, thus eliminating the need for a non-contrast acquisition when VNC is not available.
3) The application of our methods to other patient regions must be studied to determine whether DECT is equally useful and precise as in the head and neck.
4) Volumetric modulated arc therapy (VMAT) plans in our study have been optimized on non-contrast images. It would be of interest to know whether optimization on VNC images may lead to the same distributions or not.
5) Since contrast is enhanced in VMI and we know how to deal with the problem of iodine in calculations, it would be very interesting to apply automatic delineation algorithms to VMIs in order to automatize delineation of tumors and organs at risk.

6. References

6. References

1. Shivaramu. Effective atomic numbers for photon energy absorption and photon attenuation of tissues from human organs. Med Dosim. 2002;27(1):1-9. doi:10.1016/s0958-3947(01)00078-4
2. Plechaty, E F, Cullen, D E, and Howerton, R J. Tables and graphs of photon-interaction cross sections from 0. 1 keV to 100 MeV derived from the LLL evaluated-nuclear-data library. United States: N. p., 1981. Web. doi:10.2172/5788642.
3. Liauw SL, Amdur RJ, Mendenhall WM, Palta J, Kim S. The effect of intravenous contrast on intensity-modulated radiation therapy dose calculations for head and neck cancer. Am J Clin Oncol. 2005;28(5):456-459. doi:10.1097/01.coc.0000170796.89560.02
4. Lee FK, Chan CC, Law CK. Influence of CT contrast agent on dose calculation of intensity modulated radiation therapy plan for nasopharyngeal carcinoma. J Med Imaging Radiat Oncol. 2009;53(1):114-118. doi:10.1111/j.1754-9485.2009.02046.x
5. Liu AJ, Vora N, Suh S, Liu A, Schultheiss TE, Wong JY. Effect of CT contrast on volumetric arc therapy planning (RapidArc and helical tomotherapy) for head and neck cancer. Med Dosim. 2015;40(1):32-36. doi:10.1016/j.meddos.2014.07.003
6. Rankine, A. W., Lanzon, P. J., & Spry, N. A. (2008). Effect of Contrast Media on Megavoltage Photon Beam Dosimetry. Medical Dosimetry, 33(3), 169–174. doi:10.1016/j.meddos.2007.04.007
7. Eusemann, C., Holmes III, D. R., Schmidt, B., Flohr, T. G., Robb, R., McCollough, C., … Fletcher, J. G. (2008). Dual energy CT: How to best blend both energies in one fused image? Medical Imaging 2008: Visualization, Image-Guided Procedures, and Modeling. doi:10.1117/12.773095
8. Möhler C, Wohlfahrt P, Richter C, Greilich S. Methodological accuracy of image-based electron density assessment using dual-energy computed tomography. Med Phys. 2017;44(6):2429-2437. doi:10.1002/mp.12265
9. Hofmann C, Sawall S, Knaup M, Kachelrieß M. Alpha image reconstruction (AIR): a new iterative CT image reconstruction approach using voxel-wise alpha blending. Med Phys. 2014;41(6):061914. doi:10.1118/1.4875975

10. Yu L, Primak AN, Liu X, McCollough CH. Image quality optimization and evaluation of linearly mixed images in dual-source, dual-energy CT. Med Phys. 2009;36(3):1019-1024. doi:10.1118/1.3077921
11. Alvarez RE, Macovski A. Energy-selective reconstructions in X-ray computerized tomography. Phys Med Biol. 1976;21(5):733-744. doi:10.1088/0031-9155/21/5/002
12. Mendonca PR, Lamb P, Sahani DV. A Flexible Method for Multi-Material Decomposition of Dual-Energy CT Images. IEEE Trans Med Imaging. 2014;33(1):99-116. doi:10.1109/TMI.2013.2281719
13. Paulo R. S. Mendonça, Rahul Bhotika, Mahnaz Maddah, Brian Thomsen, Sandeep Dutta, Paul E. Licato, Mukta C. Joshi, "Multi-material decomposition of spectral CT images," Proc. SPIE 7622, Medical Imaging 2010: Physics of Medical Imaging, 76221W (22 March 2010); https://doi.org/10.1117/12.844531
14. Wang X, Meier D, Taguchi K, Wagenaar DJ, Patt BE, Frey EC. Material separation in X-ray CT with energy resolved photon-counting detectors. Med Phys. 2011;38(3):1534-1546. doi:10.1118/1.3553401
15. Rutherford, R.A., Pullan, B.R. & Isherwood, I. Measurement of effective atomic number and electron density using an EMI scanner. Neuroradiology 11, 15–21 (1976). https://doi.org/10.1007/BF00327253
16. McCollough, C.H., Boedeker, K., Cody, D., Duan, X., Flohr, T., Halliburton, S.S., Hsieh, J., Layman, R.R. and Pelc, N.J. (2020), Principles and applications of multienergy CT: Report of AAPM Task Group 291. Med. Phys., 47: e881-e912. https://doi.org/10.1002/mp.14157
17. Meinel FG, Bischoff B, Zhang Q, Bamberg F, Reiser MF, Johnson TR. Metal artifact reduction by dual-energy computed tomography using energetic extrapolation: a systematically optimized protocol. Invest Radiol. 2012;47(7):406-414. doi:10.1097/RLI.0b013e31824c86a3
18. De Cecco CN, Darnell A, Rengo M, et al. Dual-energy CT: oncologic applications. AJR Am J Roentgenol. 2012;199(5 Suppl):S98-S105. doi:10.2214/AJR.12.9207
19. Yoo HJ, Hong SH, Chung BM, et al. Metal Artifact Reduction in Virtual Monoenergetic Spectral Dual-Energy CT of Patients With Metallic Orthopedic Implants in the Distal Radius. AJR Am J Roentgenol. 2018;211(5):1083-1091. doi:10.2214/AJR.18.19514

20. Zopfs, D., Lennartz, S., Pennig, L. et al. Virtual monoenergetic images and post-processing algorithms effectively reduce CT artifacts from intracranial aneurysm treatment. Sci Rep 10, 6629 (2020). https://doi.org/10.1038/s41598-020-63574-8
21. Lenga L, Albrecht MH, Othman AE, et al. Monoenergetic Dual-energy Computed Tomographic Imaging: Cardiothoracic Applications. J Thorac Imaging. 2017;32(3):151-158. doi:10.1097/RTI.0000000000000259
22. Delesalle MA, Pontana F, Duhamel A, et al. Spectral optimization of chest CT angiography with reduced iodine load: experience in 80 patients evaluated with dual-source, dual-energy CT. Radiology. 2013;267(1):256-266. doi:10.1148/radiol.12120195
23. Neuhaus V, Große Hokamp N, Abdullayev N, et al. Comparison of virtual monoenergetic and polyenergetic images reconstructed from dual-layer detector CT angiography of the head and neck. Eur Radiol. 2018;28(3):1102-1110. doi:10.1007/s00330-017-5081-8
24. De Cecco CN, Caruso D, Schoepf UJ, et al. A noise-optimized virtual monoenergetic reconstruction algorithm improves the diagnostic accuracy of late hepatic arterial phase dual-energy CT for the detection of hypervascular liver lesions. Eur Radiol. 2018;28(8):3393-3404. doi:10.1007/s00330-018-5313-6
25. Shuman WP, Green DE, Busey JM, et al. Dual-energy liver CT: effect of monochromatic imaging on lesion detection, conspicuity, and contrast-to-noise ratio of hypervascular lesions on late arterial phase. AJR Am J Roentgenol. 2014;203(3):601-606. doi:10.2214/AJR.13.11337
26. Sudarski S, Apfaltrer P, Nance JW Jr, et al. Objective and subjective image quality of liver parenchyma and hepatic metastases with virtual monoenergetic dual-source dual-energy CT reconstructions: an analysis in patients with gastrointestinal stromal tumor. Acad Radiol. 2014;21(4):514-522. doi:10.1016/j.acra.2014.01.001
27. Caruso D, De Cecco CN, Schoepf UJ, et al. Can dual-energy computed tomography improve visualization of hypoenhancing liver lesions in portal venous phase? Assessment of advanced image-based virtual monoenergetic images. Clin Imaging. 2017;41:118-124. doi:10.1016/j.clinimag.2016.10.015
28. Husarik DB, Gordic S, Desbiolles L, et al. Advanced virtual monoenergetic computed tomography of hyperattenuating and hypoattenuating liver lesions: ex-vivo and

patient experience in various body sizes. Invest Radiol. 2015;50(10):695-702. doi:10.1097/RLI.0000000000000171

29. McNamara MM, Little MD, Alexander LF, Carroll LV, Beasley TM, Morgan DE. Multireader evaluation of lesion conspicuity in small pancreatic adenocarcinomas: complimentary value of iodine material density and low keV simulated monoenergetic images using multiphasic rapid kVp-switching dual energy CT. Abdom Imaging. 2015;40(5):1230-1240. doi:10.1007/s00261-014-0274-y
30. Hardie AD, Picard MM, Camp ER, et al. Application of an Advanced Image-Based Virtual Monoenergetic Reconstruction of Dual Source Dual-Energy CT Data at Low keV Increases Image Quality for Routine Pancreas Imaging. J Comput Assist Tomogr. 2015;39(5):716-720. doi:10.1097/RCT.0000000000000276
31. Mileto A, Nelson RC, Samei E, et al. Impact of dual-energy multi-detector row CT with virtual monochromatic imaging on renal cyst pseudoenhancement: in vitro and in vivo study. Radiology. 2014;272(3):767-776. doi:10.1148/radiol.14132856
32. Jung DC, Oh YT, Kim MD, Park M. Usefulness of the virtual monochromatic image in dual-energy spectral CT for decreasing renal cyst pseudoenhancement: a phantom study. AJR Am J Roentgenol. 2012;199(6):1316-1319. doi:10.2214/AJR.12.8660
33. Lee SM, Kim SH, Ahn SJ, Kang HJ, Kang JH, Han JK. Virtual monoenergetic dual-layer, dual-energy CT enterography: optimization of keV settings and its added value for Crohn's disease. Eur Radiol. 2018;28(6):2525-2534. doi:10.1007/s00330-017-5215-z
34. Martin SS, Pfeifer S, Wichmann JL, et al. Noise-optimized virtual monoenergetic dual-energy computed tomography: optimization of kiloelectron volt settings in patients with gastrointestinal stromal tumors. Abdom Radiol (NY). 2017;42(3):718-726. doi:10.1007/s00261-016-1011-5
35. Albrecht MH, Bickford MW, Nance JW Jr, et al. State-of-the-Art Pulmonary CT Angiography for Acute Pulmonary Embolism. AJR Am J Roentgenol. 2017;208(3):495-504. doi:10.2214/AJR.16.17202
36. Lu GM, Zhao Y, Zhang LJ, Schoepf UJ. Dual-energy CT of the lung. AJR Am J Roentgenol. 2012;199(5 Suppl):S40-S53. doi:10.2214/AJR.12.9112

37. Kong X, Sheng HX, Lu GM, et al. Xenon-enhanced dual-energy CT lung ventilation imaging: techniques and clinical applications. AJR Am J Roentgenol. 2014;202(2):309-317. doi:10.2214/AJR.13.11191
38. Hwang, H. J., Hoffman, E. A., Lee, C. H., Goo, J. M., Levin, D. L., Kauczor, H.-U., & Seo, J. B. (2017). The role of dual-energy computed tomography in the assessment of pulmonary function. European Journal of Radiology, 86, 320–334. doi:10.1016/j.ejrad.2016.11.010
39. Wichmann JL, Katzberg RW, Litwin SE, et al. Contrast-Induced Nephropathy. Circulation. 2015;132(20):1931-1936. doi:10.1161/CIRCULATIONAHA.115.014672
40. Mangold S, De Cecco CN, Schoepf UJ, et al. A noise-optimized virtual monochromatic reconstruction algorithm improves stent visualization and diagnostic accuracy for detection of in-stent re-stenosis in lower extremity run-off CT angiography. Eur Radiol. 2016;26(12):4380-4389. doi:10.1007/s00330-016-4304-8
41. Beland B, Levental M, Srinivasan A, Forghani R. Practice variations in salivary gland imaging and utility of virtual unenhanced dual energy CT images for the detection of major salivary gland stones. Acta Radiol. 2019;60(9):1144-1152. doi:10.1177/0284185118817906
42. Wang CK, Tsai JM, Chuang MT, et al. Bone marrow edema in vertebral compression fractures: detection with dual-energy CT. Radiology. 2013;269(2):525–533
43. Forghani R, Kelly H, Yu E, et al. Low-energy virtual monochromatic dual-energy computed tomography images for the evaluation of head and neck squamous cell carcinoma: a study of tumor visibility compared with single-energy computed tomography and user acceptance. J Comput Assist Tomogr. 2017;41(4):565–571
44. Stolzmann P, Winklhofer S, Schwendener N, Alkadhi H, Thali MJ, Ruder TD. Monoenergetic computed tomography reconstructions reduce beam hardening artifacts from dental restorations. Forensic Sci Med Pathol. 2013;9(3):327-332. doi:10.1007/s12024-013-9420-z
45. Tanaka R, Hayashi T, Ike M, Noto Y, Goto TK. Reduction of dark-band-like metal artifacts caused by dental implant bodies using hypothetical monoenergetic imaging after dual-energy computed tomography. Oral Surg Oral Med Oral Pathol Oral Radiol. 2013;115(6):833-838. doi:10.1016/j.oooo.2013.03.014

46. Bongers MN, Schabel C, Thomas C, et al. Comparison and Combination of Dual-Energy- and Iterative-Based Metal Artifact Reduction on Hip Prosthesis and Dental Implants. PLoS One. 2015;10(11):e0143584. Published 2015 Nov 24. doi:10.1371/journal.pone.0143584
47. Kraft M, Ibrahim M, Spector M, et al. Comparison of virtual monochromatic series, iodine overlay maps, and single energy CT equivalent images in head and neck cancer conspicuity. Clin Imaging. 2018;48:26–31
48. May MS, Bruegel J, Brand M, et al. Computed tomography of the head and neck region for tumor staging-comparison of dual-source, dual-energy and low-kilovolt, single-energy acquisitions. Invest Radiol. 2017;52(9):522–528.
49. Forghani R, Levental M, Gupta R, et al. Different spectral Hounsfield unit curve and high-energy virtual monochromatic image characteristics of squamous cell carcinoma compared with nonossified thyroid cartilage. AJNR Am J Neuroradiol. 2015;36(6):1194–1200
50. Kuno H, Sakamaki K, Fujii S, et al. Comparison of MR imaging and dual-energy CT for the evaluation of cartilage invasion by laryngeal and hypopharyngeal squamous cell carcinoma. AJNR Am J Neuroradiol. 2018;39(3):524–531
51. Lam S, Gupta R, Levental M, et al. Optimal virtual monochromatic images for evaluation of normal tissues and head and neck càncer using dual-energy CT. AJNR Am J Neuroradiol. 2015;36 (8):1518–1524
52. Mallinson, P. I., Coupal, T. M., McLaughlin, P. D., Nicolaou, S., Munk, P. L., & Ouellette, H. A. (2016). Dual-Energy CT for the Musculoskeletal System. Radiology, 281(3), 690–707. doi:10.1148/radiol.2016151109
53. Gruber M, Bodner G, Rath E, Supp G, Weber M, Schueller-Weidekamm C. Dual-energy computed tomography compared with ultrasound in the diagnosis of gout. Rheumatology (Oxford). 2014;53(1):173-179. doi:10.1093/rheumatology/ket341
54. Zhang B, Yang M, Wang H. Diagnostic value of ultrasound versus dual-energy computed tomography in patients with different stages of acute gouty arthritis. Clin Rheumatol. 2020;39(5):1649-1653. doi:10.1007/s10067-020-05014-6
55. Dalbeth N, Choi HK. Dual-energy computed tomography for gout diagnosis and management. Curr Rheumatol Rep. 2013;15(1):301. doi:10.1007/s11926-012-0301-3

56. Manger B, Lell M, Wacker J, Schett G, Rech J. Detection of periarticular urate deposits with dual energy CT in patients with acute gouty arthritis. Ann Rheum Dis. 2012;71(3):470-472. doi:10.1136/ard.2011.154054
57. Pache G, Krauss B, Strohm P, et al. Dual-energy CT virtual noncalcium technique: detecting posttraumatic bone marrow lesions--feasibility study. Radiology. 2010;256(2):617-624. doi:10.1148/radiol.10091230
58. Guggenberger R, Gnannt R, Hodler J, et al. Diagnostic performance of dual-energy CT for the detection of traumatic bone marrow lesions in the ankle: comparison with MR imaging. Radiology. 2012;264(1):164-173. doi:10.1148/radiol.12112217
59. Damilakis J, Adams JE, Guglielmi G, Link TM. Radiation exposure in X-ray-based imaging techniques used in osteoporosis. Eur Radiol. 2010;20(11):2707-2714. doi:10.1007/s00330-010-1845-0
60. Taasti, V. T., Michalak, G. J., Hansen, D. C., Deisher, A. J., Kruse, J. J., Krauss, B., … McCollough, C. H. (2017). Validation of proton stopping power ratio estimation based on dual energy CT using fresh tissue samples. Physics in Medicine & Biology, 63(1), 015012. doi:10.1088/1361-6560/aa952f
61. Van Elmpt, W., Landry, G., Das, M., & Verhaegen, F. (2016). Dual energy CT in radiotherapy: Current applications and future outlook. Radiotherapy and Oncology, 119(1), 137–144. doi:10.1016/j.radonc.2016.02.026
62. Yang M, Virshup G, Clayton J, Zhu XR, Mohan R, Dong L. Theoretical variance analysis of single- and dual-energy computed tomography methods for calculating proton stopping power ratios of biological tissues. Phys Med Biol. 2010;55(5):1343-1362. doi:10.1088/0031-9155/55/5/006
63. Hünemohr N, Krauss B, Tremmel C, Ackermann B, Jäkel O, Greilich S. Experimental verification of ion stopping power prediction from dual energy CT data in tissue surrogates. Phys Med Biol. 2014;59(1):83-96. doi:10.1088/0031-9155/59/1/83
64. Hudobivnik N, Schwarz F, Johnson T, et al. Comparison of proton therapy treatment planning for head tumors with a pencil beam algorithm on dual and single energy CT images. Med Phys. 2016;43(1):495. doi:10.1118/1.4939106
65. Mileto A, Allen BC, Pietryga JA, et al. Characterization of Incidental Renal Mass With Dual-Energy CT: Diagnostic Accuracy of Effective Atomic Number Maps for

Discriminating Nonenhancing Cysts From Enhancing Masses. AJR Am J Roentgenol. 2017;209(4):W221-W230. doi:10.2214/AJR.16.17325

66. Njeh CF. Tumor delineation: The weakest link in the search for accuracy in radiotherapy. J Med Phys. 2008;33(4):136-140. doi:10.4103/0971-6203.44472
67. International Commission on Radiation Units and Measurements. ICRU Report 50. Prescribing, recording, and reporting photon beam therapy. Bethesda, MD: ICRU, 1993.
68. International Commission on Radiation Units and Measurements. ICRU Report 62. Prescribing, recording, and reporting photon beam therapy (Supplement to ICRU Report 50). Bethesda, MD: ICRU, 1999
69. Weiss, E., & Hess, C. F. (2003). The Impact of Gross Tumor Volume (GTV) and Clinical Target Volume (CTV) Definition on the Total Accuracy in Radiotherapy. Strahlentherapie Und Onkologie, 179(1), 21–30. doi:10.1007/s00066-003-0976-5
70. Albrecht MH, Vogl TJ, Martin SS, et al. Review of Clinical Applications for Virtual Monoenergetic Dual-Energy CT. Radiology. 2019;293(2):260-271. doi:10.1148/radiol.2019182297
71. Wichmann JL, Nöske EM, Kraft J, et al. Virtual monoenergetic dual-energy computed tomography: optimization of kiloelectron volt settings in head and neck cancer. Invest Radiol. 2014;49(11):735-741. doi:10.1097/RLI.0000000000000077
72. Roele, E.D., Timmer, V.C.M.L., Vaassen, L.A.A. et al. Dual-Energy CT in Head and Neck Imaging. Curr Radiol Rep 5, 19 (2017). https://doi.org/10.1007/s40134-017-0213-0
73. Noid, G., Schott, D., Paulson, E., Zhu, J., Shah, J., & Li, X. A. (2021). Technical Note: Using virtual noncontrast images from dual-energy CT to eliminate the need of precontrast CT for x-ray radiation treatment planning of abdominal tumors †. Medical Physics, 48(3), 1365–1371. doi:10.1002/mp.14702
74. Yamada, S., Ueguchi, T., Ogata, T., Mizuno, H., Ogihara, R., Koizumi, M., … Ogawa, K. (2014). Radiotherapy treatment planning with contrast-enhanced computed tomography: feasibility of dual-energy virtual unenhanced imaging for improved dose calculations. Radiation Oncology, 9(1), 168. doi:10.1186/1748-717x-9-168

75. Elawadi AA, AlMohsen S, AlGendy R, Allazkani H, Mohamed RA, AlAssaf H, Nisbet A, Alshanqity M. The Effect of Contrast Agents on Dose Calculations of Volumetric Modulated Arc Radiotherapy Plans for Critical Structures. Applied Sciences. 2021; 11(18):8355. https://doi.org/10.3390/app11188355
76. Yu L, Christner JA, Leng S, Wang J, Fletcher JG, McCollough CH. Virtual monochromatic imaging in dual-source dual-energy CT: radiation dose and image quality. Med Phys. 2011;38(12):6371-6379. doi:10.1118/1.3658568
77. Kalisz K, Rassouli N, Dhanantwari A, Jordan D, Rajiah P. Noise characteristics of virtual monoenergetic images from a novel detector-based spectral CT scanner. Eur J Radiol. 2018;98:118-125. doi:10.1016/j.ejrad.2017.11.005
78. D'Angelo T, Cicero G, Mazziotti S, et al. Dual energy computed tomography virtual monoenergetic imaging: technique and clinical applications. Br J Radiol. 2019;92(1098):20180546. doi:10.1259/bjr.20180546
79. International Commission on Radiation Units and Measurements, ICRU Report No. 87: Radiation dose and image-quality assessment in computed tomography, 2012.
80. International Atomic Energy Agency, Quality Assurance Programme for Computed Tomography: Diagnostic and Therapy Applications. Human Health Series No 19. Vienna:IAEA; 2012.
81. American Association of Physicists in Medicine (AAPM) Report 233: Performance evaluation of Computed Tomography Systems, 2019.
82. McNitt-Gray, M. (2006), MO-A-ValB-01: Tradeoffs in Image Quality and Radiation Dose for CT. Med. Phys., 33: 2154-2155. https://doi.org/10.1118/1.2241390.
83. Droege RT, Morin RL. A practical method to measure the MTF of CT scanners. Med Phys. 1982;9(5):758-760. doi:10.1118/1.595124.
84. Judy PF. The line spread function and modulation transfer function of a computed tomographic scanner. Med Phys. 1976;3(4):233-236. doi:10.1118/1.594283
85. Samei E, Flynn MJ, Reimann DA. A method for measuring the presampled MTF of digital radiographic systems using an edge test device. Med Phys. 1998;25(1):102-113. doi:10.1118/1.598165
86. Rossmann K. Point spread-function, line spread-function, and modulation transfer function. Tools for the study of imaging systems. Radiology. 1969;93(2):257-272. doi:10.1148/93.2.257

87. Chen B, Christianson O, Wilson JM, Samei E. Assessment of volumetric noise and resolution performance for linear and nonlinear CT reconstruction methods. Med Phys. 2014;41(7):071909. doi:10.1118/1.4881519
88. Chao, E.H., Toth, T.L., Bromberg, N.B.,Williams, E.C., Fox, S.H., Carleton, D.A.: A statistical method of defining low contrast detectability. Radiology 217, 162 (2000)
89. Seibert JA. Tradeoffs between image quality and dose. Pediatr Radiol. 2004;34 Suppl 3:S183-S241. doi:10.1007/s00247-004-1268-7
90. Alvarez, Robert & Seppi, Edward. (1979). A Comparison of Noise and Dose in Conventional and Energy Selective Computed Tomography. Nuclear Science, IEEE Transactions on. 26. 2853 - 2856. 10.1109/TNS.1979.4330549.
91. Dolly S, Chen HC, Anastasio M, Mutic S, Li H. Practical considerations for noise power spectra estimation for clinical CT scanners. J Appl Clin Med Phys. 2016;17(3):392-407. Published 2016 May 8. doi:10.1120/jacmp.v17i3.5841
92. Code of Federal Regulations, Title 21, vol.8, subchapter J. Food and Drug Administration (FDA), April 2020.
93. Yang K, Kwan AL, Huang SY, Packard NJ, Boone JM. Noise power properties of a cone-beam CT system for breast cancer detection. Med Phys. 2008;35(12):5317-5327. doi:10.1118/1.3002411
94. IEC 61223-2-6. International standard IEC 61223-2-6. Evaluation and routine testing in medical imaging departments - part 2-6: acceptance tests - imaging performance of computed tomography X-ray equipment; 2006.
95. Gulliksrud K, Stokke C, Martinsen AC. How to measure CT image quality: variations in CT-numbers, uniformity and low contrast resolution for a CT quality assurance phantom. Phys Med. 2014;30(4):521-526. doi:10.1016/j.ejmp.2014.01.006
96. Matsumoto K, Jinzaki M, Tanami Y, Ueno A, Yamada M, Kuribayashi S. Virtual monochromatic spectral imaging with fast kilovoltage switching: improved image quality as compared with that obtained with conventional 120- kVp CT. Radiology. 2011;259(1):257-262. doi:10.1148/radiol.11100978.
97. Albrecht MH, Scholtz JE, Kraft J, et al. Assessment of an Advanced Monoenergetic Reconstruction Technique in Dual-Energy Computed Tomography of Head and Neck Cancer. Eur Radiol. 2015;25(8):2493-2501. doi:10.1007/s00330-015-3627-1

98. Leithner D, Mahmoudi S, Wichmann JL, et al. Evaluation of virtual monoenergetic imaging algorithms for dual-energy carotid and intracerebral CT angiography: Effects on image quality, artifacts and diagnostic performance for the detection of stenosis. Eur J Radiol. 2018;99:111-117. doi:10.1016/j.ejrad.2017.12.024
99. Gudi S, Ghosh-Laskar S, Agarwal JP, et al. Interobserver Variability in the Delineation of Gross Tumour Volume and Specified Organs-at-risk During IMRT for Head and Neck Cancers and the Impact of FDG-PET/CT on Such Variability at the Primary Site. J Med Imaging Radiat Sci. 2017;48(2):184-192. doi:10.1016/j.jmir.2016.11.003
100. Anderson CM, Sun W, Buatti JM, et al. Interobserver and intermodality variability in GTV delineation on simulation CT, FDG-PET, and MR Images of Head and Neck Cancer. Jacobs J Radiat Oncol. 2014;1(1):006.
101. Jager, E., Kasperts, N., Caldas-Magalhaes, J., Philippens, M., Pameijer, F. A., Terhaard, C., & Raaijmakers, C. (2015). GTV delineation in supraglottic laryngeal carcinoma: interobserver agreement of CT versus CT-MR delineation. Radiation Oncology, 10(1), 26. doi:10.1186/s13014-014-0321-4
102. Forghani, R. (2019). An update on advanced dual-energy CT for head and neck cancer imaging. Expert Review of Anticancer Therapy. doi:10.1080/14737140.2019.1626234
103. Tawfik, A. M., Kerl, J. M., Bauer, R. W., Nour-Eldin, N.-E., Naguib, N. N. N., Vogl, T. J., & Mack, M. G. (2012). Dual-Energy CT of Head and Neck Cancer. Investigative Radiology, 47(5), 306–311. doi:10.1097/rli.0b013e31821e3062
104. Noid, G., Zhu, J., Tai, A., Mistry, N., Schott, D., Prah, D., … Li, X. A. (2020). Improving Structure Delineation for Radiation Therapy Planning Using Dual-Energy CT. Frontiers in Oncology, 10. doi:10.3389/fonc.2020.01694
105. Vinod SK, Jameson MG, Min M, Holloway LC. Uncertainties in volume delineation in radiation oncology: A systematic review and recommendations for future studies. Radiother Oncol. 2016;121(2):169-179. doi:10.1016/j.radonc.2016.09.009
106. Jameson MG, Holloway LC, Vial PJ, Vinod SK, Metcalfe PE. A review of methods of analysis in contouring studies for radiation oncology. J Med Imaging Radiat Oncol. 2010;54(5):401-410. doi:10.1111/j.1754-9485.2010.02192.x

107. Remeijer, P., Rasch, C., Lebesque, J. V., & van Herk, M. (1999). A general methodology for three-dimensional analysis of variation in target volume delineation. Medical Physics, 26(6), 931–940. doi:10.1118/1.598485
108. Rao M, Stough J, Chi YY, et al. Comparison of human and automatic segmentations of kidneys from CT images. Int J Radiat Oncol Biol Phys. 2005;61(3):954-960. doi:10.1016/j.ijrobp.2004.11.014
109. Pevsner A, Davis B, Joshi S, et al. Evaluation of an automated deformable image matching method for quantifying lung motion in respiration-correlated CT images. Med Phys. 2006;33(2):369-376. doi:10.1118/1.2161408
110. Toepker M, Czerny C, Ringl H, et al. Can dual-energy CT improve the assessment of tumor margins in oral cancer?. Oral Oncol. 2014;50(3):221-227. doi:10.1016/j.oraloncology.2013.12.001
111. Vaassen F, Hazelaar C, Vaniqui A, Gooding M, van der Heyden B, Canters R, van Elmpt W. Evaluation of measures for assessing time-saving of automatic organ-at-risk segmentation in radiotherapy. Phys Imaging Radiat Oncol. 2019 Dec 17;13:1-6. doi: 10.1016/j.phro.2019.12.001.
112. Dolz J, Kirişli HA, Fechter T, et al. Interactive contour delineation of organs at risk in radiotherapy: Clinical evaluation on NSCLC patients. Med Phys. 2016;43(5):2569. doi:10.1118/1.4947484
113. Zhu J, Liu Y, Zhang J, Wang Y, Chen L. Preliminary Clinical Study of the Differences Between Interobserver Evaluation and Deep Convolutional Neural Network-Based Segmentation of Multiple Organs at Risk in CT Images of Lung Cancer. Front Oncol. 2019;9:627. Published 2019 Jul 5. doi:10.3389/fonc.2019.00627
114. Fotina I, Lütgendorf-Caucig C, Stock M, Pötter R, Georg D. Critical discussion of evaluation parameters for inter-observer variability in target definition for radiation therapy. Strahlenther Onkol. 2012;188(2):160-167. doi:10.1007/s00066-011-0027-6
115. (112)Rasch, C. R., Steenbakkers, R. J., Fitton, I., Duppen, J. C., Nowak, P. J., Pameijer, F. A., … van Herk, M. (2010). Decreased 3D observer variation with matched CT-MRI, for target delineation in Nasopharynx cancer. Radiation Oncology, 5(1), 21. doi:10.1186/1748-717x-5-21

116. Brouwer CL, Steenbakkers RJ, van den Heuvel E, et al. 3D Variation in delineation of head and neck organs at risk. Radiat Oncol. 2012;7:32. Published 2012 Mar 13. doi:10.1186/1748-717X-7-32
117. Moeckli R, Sozzi WJ, Mirimanoff RO, et al. Physical considerations on discrepancies in target volume delineation. Z Med Phys. 2009;19(4):224-235. doi:10.1016/j.zemedi.2009.06.006
118. Shibamoto, Y., Naruse, A., Fukuma, H., Ayakawa, S., Sugie, C., & Tomita, N. (2007). Influence of contrast materials on dose calculation in radiotherapy planning using computed tomography for tumors at various anatomical regions: A prospective study. Radiotherapy and Oncology, 84(1), 52–55. doi:10.1016/j.radonc.2007.05.015
119. Choi Y, Kim JK, Lee HS, et al. Influence of intravenous contrast agent on dose calculations of intensity modulated radiation therapy plans for head and neck cancer. Radiother Oncol. 2006; 81(2): 158–162, doi: 10.1016/j.radonc.2006.09.010, indexed in Pubmed: 17050020
120. Holz JA, Alkadhi H, Laukamp KR, et al. Quantitative accuracy of virtual non-contrast images derived from spectral detector computed tomography: an abdominal phantom study. Sci Rep. 2020;10(1):21575. Published 2020 Dec 9. doi:10.1038/s41598-020-78518-5
121. Sahbaee, P., Segars, W. P., Marin, D., Nelson, R. C., & Samei, E. (2017). The Effect of Contrast Material on Radiation Dose at CT: Part I. Incorporation of Contrast Material Dynamics in Anthropomorphic Phantoms. Radiology, 283(3), 739–748. doi:10.1148/radiol.2016152851
122. Van Cauteren, T., Van Gompel, G., Nieboer, K.H. et al. Improved enhancement in CT angiography with reduced contrast media iodine concentrations at constant iodine dose. Sci Rep 8, 17493 (2018). https://doi.org/10.1038/s41598-018-35918-y
123. Bae KT. Intravenous contrast medium administration and scan timing at CT: considerations and approaches. Radiology. 2010;256(1):32-61. doi:10.1148/radiol.10090908
124. Komiyama R, Ohira S, Kanayama N, et al. Volumetric modulated arc therapy treatment planning based on virtual monochromatic images for head and neck cancer: effect of the contrast-enhanced agent on dose distribution. J Appl Clin Med Phys. 2019;20(11):144-152. doi:10.1002/acm2.12752

125. Liauw SL, Amdur RJ, Mendenhall WM, Palta J, Kim S. The effect of intravenous contrast on intensity-modulated radiation therapy dose calculations for head and neck cancer. Am J Clin Oncol. 2005;28(5):456-459. doi:10.1097/01.coc.0000170796.89560.02
126. Ohira S, Komiyama R, Karino T, et al. Volumetric modulated arc therapy planning based on virtual monochromatic images: Effect of inaccurate CT numbers on dose distributions. Phys Med. 2019;60:83-90. doi:10.1016/j.ejmp.2019.03.022
127. Lundin M, Lidén M, Magnuson A, et al. Virtual non-contrast dual-energy CT compared to single-energy CT of the urinary tract: a prospective study. Acta Radiol. 2012;53(6):689-694. doi:10.1258/ar.2012.110661
128. Sauter AP, Muenzel D, Dangelmaier J, et al. Dual-layer spectral computed tomography: Virtual non-contrast in comparison to true non-contrast images. Eur J Radiol. 2018;104:108-114. doi:10.1016/j.ejrad.2018.05.007
129. Zhang X, Zhang G, Xu L, et al. Utilisation of virtual non-contrast images and virtual mono-energetic images acquired from dual-layer spectral CT for renal cell carcinoma: image quality and radiation dose. Insights Imaging. 2022;13(1):12. Published 2022 Jan 24. doi:10.1186/s13244-021-01146-8
130. Li B, Pomerleau M, Gupta A, Soto JA, Anderson SW. Accuracy of Dual-Energy CT Virtual Unenhanced and Material-Specific Images: A Phantom Study. AJR Am J Roentgenol. 2020;215(5):1146-1154. doi:10.2214/AJR.19.22372
131. Jacobsen MC, Cressman ENK, Tamm EP, et al. Dual-Energy CT: Lower Limits of Iodine Detection and Quantification. Radiology. 2019;292(2):414-419. doi:10.1148/radiol.2019182870
132. Kruis MF. Improving radiation physics, tumor visualisation, and treatment quantification in radiotherapy with spectral or dual-energy CT. J Appl Clin Med Phys. 2022;23(1):e13468. doi:10.1002/acm2.13468
133. Miller J, DiMaso L, Huang-Vredevoogd J, Shah J, Lawless M. Characterization of size-specific effects during dual-energy CT material decomposition of non-iodine materials. J Appl Clin Med Phys. 2021;22(12):168-176. doi:10.1002/acm2.13471
134. Toepker M, Moritz T, Krauss B, et al. Virtual non-contrast in second-generation, dual-energy computed tomography: reliability of attenuation values. Eur J Radiol. 2012;81(3):e398-e405. doi:10.1016/j.ejrad.2011.12.011

135. Liugang G, Kai X, Chunying L, et al. Generation of Virtual Non-Contrast CT From Intravenous Enhanced CT in Radiotherapy Using Convolutional Neural Networks. Front Oncol. 2020;10:1715. Published 2020 Sep 8. doi:10.3389/fonc.2020.01715
136. Tomita H, Shibata K. Verification of the Dose Reduction Effect via Diluted Injection in Dual-Energy Computed Tomography Using a Human Blood Flow Phantom [published correction appears in Radiol Res Pract. 2019 Jun 19;2019:5109419]. Radiol Res Pract. 2019;2019:3512126. Published 2019 Apr 1. doi:10.1155/2019/3512126
137. Carrascosa, P., Capunay, C., Rodriguez-Granillo, G.A. et al. Substantial iodine volume load reduction in CT angiography with dual-energy imaging: insights from a pilot randomized study. Int J Cardiovasc Imaging 30, 1613–1620 (2014). https://doi.org/10.1007/s10554-014-0501-1
138. Shen Y, Hu X, Zou X, Zhu D, Li Z, Hu D. Did low tube voltage CT combined with low contrast media burden protocols accomplish the goal of "double low" for patients? An overview of applications in vessels and abdominal parenchymal organs over the past 5 years. Int J Clin Pract. 2016;70 Suppl 9B:B5-B15. doi:10.1111/ijcp.12861